Developments in the Field of Engineering

Editor: Assist Prof. Mehmet TEMİZ

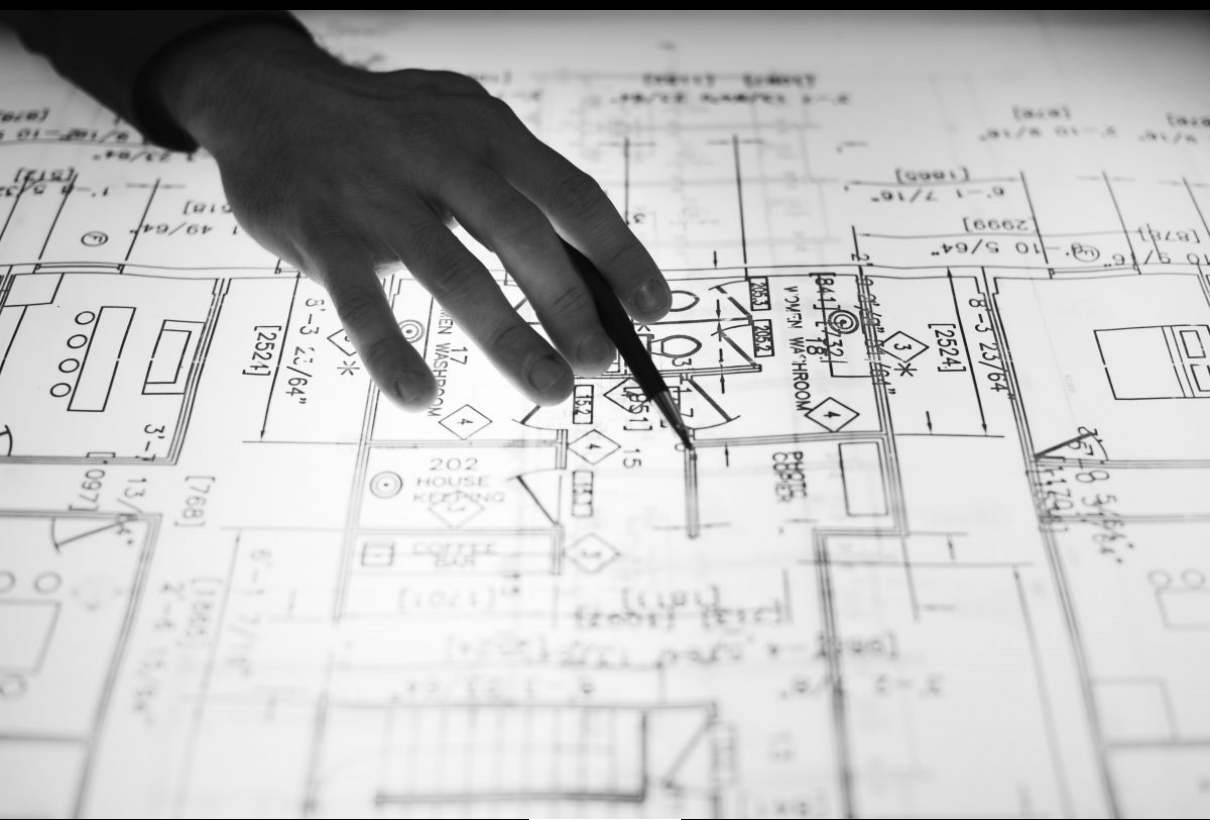

yaz yayınları

Developments in the Field of Engineering

Editor

Assist. Prof. Mehmet TEMİZ

yaz yayınları

2023

Developments in the Field of Engineering

Editor: Assist. Prof. Mehmet TEMİZ

E_ISBN 978-625-6524-95-8

Aralık 2023 – Afyonkarahisar

Dizgi/Mizanpaj: YAZ Yayınları

Kapak Tasarım: YAZ Yayınları

YAZ Yayınları. Yayıncı Sertifika No: 73086

M.İhtisas OSB Mah. 4A Cad. No:3/3
İscehisar/AFYONKARAHİSAR

www.yazyayinlari.com

yazyayinlari@gmail.com

info@yazyayinlari.com

İÇİNDEKİLER

A NEW LOOK AT ENERGY STORAGE SYSTEMS

Tarkan KOCA[1]

1. INTRODUCTION

In this study, a system which provides mechanical storage of electrical energy has been designed and installed. The back-bone of this study is the design of a system where up to 30 kWh of unused surplus of electricity from a small scale solar field can be stored without the use of batteries, capacitors, etc. The service life of the system is calculated as 30 years and will require scheduled maintenance for every 5 years. The logic behind this system, which is an alternative to traditional electrical storage systems, is that the amount of electricity obtained from the solar energy harvested by the solar panels, except for the instant use, is stored as potential energy within the system and re-applied to the grid when needed. In this storage system, the efficiency, which is 90%, remains constant around this value.

Electrical energy storage is the process of converting electrical energy from the power grid into a form that can be stored so that it can be converted into electrical energy when needed [1]. Such processes generate electricity during periods of low demand and low generation costs, or from intermittent energy sources, for use during periods of high demand and high generation costs, or when other generation options are not

[1] Assoc. Prof. Dr. Tarkan KOCA, İnönü Üniversity, Engineering Faculty, Mechanical Engineering Department, tarkan.koca@inonu.edu.tr, ORCID: 0000-0002-6881-4153.

available. [2].The amount of electricity obtained from solar energy outside the instant use should be stored somehow. Because if the amount out of use is not stored in an energy production method that is capable of producing only in daylight with an efficiency that is already considered low, the gain would be below the target. The most common methods used today for the storage of electrical energy are the storage of electricity in batteries or capacitors. However, such very successful and stable systems have some disadvantages. Considering an energy storage system that works with solar panels; these disadvantages eliminate a large portion of the gain generated by the solar panels. As an example, the lifetime of the batteries produced today is much shorter than that of solar panels. Today, solar panels provide service without maintenance for 25 years while batteries are out of service within 2 years. In addition, electrical storage capacities are decreasing day by day depending on their usage time. Today, when a capacity of 30 kWh battery group is measured after 6 months of use, it has been observed that it can drop to 25 kWh. This decrease in capacity increases exponentially over time. This disadvantage forces electricity producers to purchase new batteries every two years. The longer-lasting batteries have relatively higher costs, and even if this cost is met, ultimately these expensive storage systems also share the same end with cheap batteries. In other words, electric manufacturers use a large part of their gain from solar energy, in some cases all, to renew their malfunctioned batteries. This means that the user or the manufacturer cannot profit, may lose money from this work.

In this study, an alternative storage system design, strength analysis and efficiency calculations are included. This system brings a significant innovation to the energy storage category and is completely different from the traditional method of storage with batteries and capacitors. In this system,

electricity is converted to potential energy in a manner similar to the storage of water in the dams and, if necessary, is re-introduced to the network. This system will ensure that 30 kWh of electricity produced by the panels in a small scale solar field is converted to potential energy and stored. While doing this, it does not use a conventional method such as battery and capacitor. The service life is expected to be at least 30 years and the maintenance period to be 5 years. The lifespan of this system will be longer than the lifespan of the solar panels. System efficiency will not change with time. Maintenance will be quite easy. The system can be transported easily to the desired location (Mobility). Most importantly, in case of capacity increase, it is possible to increase capacity by modifying the system or adding another one from the same system (Modularity). The logic behind this system, which is an alternative to traditional electrical storage systems, energy is stored as potential energy within the system and re-applied to the grid when needed.

2. ELECTRICAL ENERGY STORAGE METHODS

Storage methods with battery; Lithium-Ion Batteries, Lead-Acid Batteries, Nickel Cadmium Batteries, Ultra-Capacitors, Deep Loop Gel Batteries. Mechanical Storage Methods; Pump Storage Hydroelectric Systems and Compressed Air Storage Electrical Systems. The electrical energy can be stored in different energy forms: mechanical, thermal, chemical, electro-chemical, electrical, etc. [3]. The classification of energy storage technologies according to the stored energy form is illustrated, Figure 1. Electrical Energy Storage system necessary to be taken into consideration for different applications. The

details of the Electrical Energy Storage system have been described in literatures [4].

Figure 1. Electrical Energy Storage Method [5]

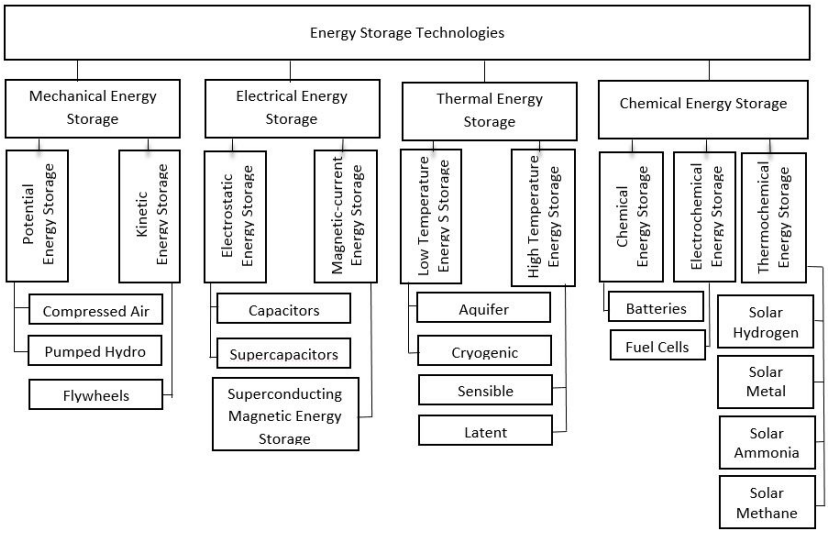

Storage technologies are defined as flywheels [6], compressed air storage [7], pumped hydro storage [8], gravity modules, hydraulic storage (HHS), breakthrough energy storage, and advanced rail energy storage (ARES).

Gravity and its basic properties are energy rating, power rating, energy density, power density, lifespan, and circulation efficiency.

Pumped Hydro Storage (PHS) The pumped hydro storage is the largest and most used energy storage technology existent. The electrical storage capacity is 120 GB in worldwide. It represents nearly 99% [10, 12]. The pumped hydro storage occurs of two water reservoirs. The water body at the high elevation speak for the stored energy. When not needed energy, it pumps water from the lower reservoir to the upper reservoir. Then water from the upper reservoir is released. Flows through

hydro turbines and producing electrical energy. This method is long-lasting, high-yielding and low-loss [11].

Compressed Air Energy Storage; The Compressed Air Energy Storage is a technology known and used since the 19th century. Electrical compressors are used to compress air and store. When needed energy, the air is released. It is mixed with natural gas and burned in a gas turbine. Numerous studies are underway to improve the compressed air energy storage. There are two in the world from the compressed air energy storage. They are located in Germany and in USA [13]. This storage can increasing the amount of energy stored by up to three times [14]. Compressed air energy storage stores large amounts of energy [15].

Flywheel Energy Storage; Flywheel energy storage has been around since the 1970s. In flywheel energy storage, rotational energy is stored in an accelerated rotor, or rotating cylinder. The main components of the system are the rotating cylinder, bearings, and shaft. During the charging process, the rotor is accelerated to speeds in excess of 30,000 rpm. Energy is stored in the flywheel [16]. If necessary, the flywheel releases energy and acts as a generator to drive the machine. Advantages: low discharge cycles, low maintenance, high efficiency [17]. The disadvantages of this system are high energy losses and high cost [18].

Battery Energy Storage System; Battery energy storage systems store electricity in the form of chemical energy. [19]. A battery consists of a set of low battery cells connected in parallel and series. The cells are made up of a liquid. A battery is charged and when needed energy discharging. High power and energy density facilitate the construction of battery energy storage systems due to short lead times, possible comfortable

seating, and technological modularity. However, most batteries contain toxic metal substances.

Superconducting Magnetic Energy Storage; T A superconducting magnetic energy storage device consists of a coil, a power processing system, a refrigerator, and a vacuum. Energy is stored in a magnetic field created by a direct current flowing through a superconducting coil. The power requested is available immediately. The superconducting magnetic energy storage is hopeful for load leveling [20]

Potential Energy Storage System (Gravitricity storage systems); This system brings a significant innovation to the energy storage category. This method is used to store the potential energy by using the force of gravity. Potential energy storage is completely different from the traditional method of storage with batteries and capacitors. In this system, electricity is converted to potential energy in a manner similar to the storage of water in the dams. The Potential Energy Storage System termed ravitricity is based on vertically raising and lowering down a mass. Gravitricity is similar to deep sea energy storage [21]. Modeling of gravitricity storage systems is very important [22]. Gravitricity started building in 2018 to build a system of 250 kWh in South Africa [23].

3. THE SYSTEM STORING ELECTRICAL ENERGY AS POTENTIAL ENERGY: MODELING THE SYSTEM

This section presents suggestions for gravity storage systems and their sizing. This system stores energy in the form of gravitational potential energy, and storage is done by locking weights. The system charges by increasing the load and discharges during periods of high load when the load can be decreased. The structure of a gravitational energy storage system

basically consists of a load, gears, rails, DC motor, and inverter. The system is charged by lifting the load and discharged during periods of high demand when the load is released for discharge. The sequence of operation of the experimental set is very important.

The electrical energy obtained is used in an electric motor. The electric motor converts electrical energy into mechanical energy and works through a pulley system when lifting the load. As mass increases, potential energy increases. When the load reaches its peak, energy is stored as mechanical potential energy. Discharge mode occurs when energy is needed. Therefore, the engine works in reverse and acts as a generator. [24].

In the test set, 2 kg load is lifted by a motor to a height of 100 cm. Thus, electrical energy is stored mechanically. The load then generates electrical energy by moving the motor while making free fall movement on the rails, Figure 2. This system stores energy in the form of gravitational potential energy, and storage is done by locking weights

Figure 2. Image of the Potential Energy Storage System

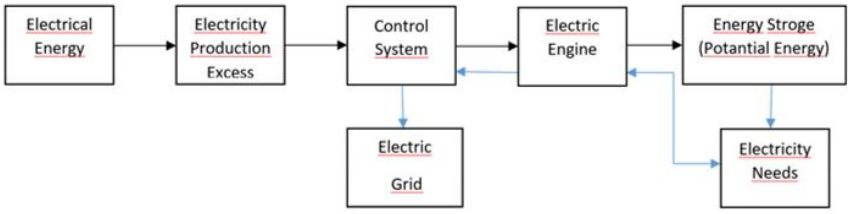

The current and voltage values on the system were measured and potential energy was calculated. Accordingly, the efficiency was calculated.

An overall flow diagram of system processes is important. Current creates electricity along with voltage. Inverters convert direct current to alternating current for use in

the power grid. The electrical energy obtained is used in the electric motor, and as the mass increases, the potential energy also increases. When the load reaches its peak, energy is stored as potential energy. This process is called system energy storage mode. Input and output voltage and current are measured and energy is calculated according to time. The current and voltage values on the system were measured and potential energy was calculated. Total energy and efficiency was calculated, Table 1.

Table 1. Total Energy and Efficiency

Total energy in	260.86 Joule
Total energy out	160.59 Joule
Efficiency	61.6 %

In addition, the sample calculations related to the realistic mechanical storage of electrical energy in solar power plants are given below. Consider an energy storage facility where a concrete block of $5mx4mx2m$ is used as a weight. (Density 2400 $kg\ m^{-3}$) Let us assume that this block moves within a 7-storey building. When this system is installed on an area of 1000 square meters, it fits 50 cells and a storage system with a capacity of 400 KWh is obtained. If soil containing iron ore is used as the filling material for the same system instead of concrete, 800 kWh storage facility can be established; if lead plates are used, a storage facility with a capacity of 1.8 MWh can be established. Gearbox output shaft diameter is 50 mm. The torque value is 10941 kgm for 150 diameters. A 10:1 gear system will be installed on the shaft to move a load of around 110 tons. As a result of this operation, the speed is 5 rpm. As a result, when losses are taken into account, 100 metric tons of load can be lifted with this system by means of a 90 kW motor.

4. CONCLUSIONS

This system brings a significant innovation to the energy storage category and is completely different from the traditional method of storage with batteries and capacitors. It can be installed at any desired point regardless of geography. It does not need stream source or impermeable caves. The setup would be extremely fast and inexpensive. There is no need to hire sensitive or special equipment or staff that is difficult to find in the market. By varying the type of filling material, different storage quantities can be provided in the same volume. Compared to other systems, it has a long service life and low maintenance costs. According to the calculations, the maintenance period is long. Silent operation is another feature. It is also different from capacitor based systems because electricity is not stored statically in this new system. In this system, electricity is converted to potential energy in a manner similar to the storage of water in the dams and, if necessary, is re-introduced to the network. Lifespan at least 15 times longer than batteries, so the cost is lower. Maintenance can be done by the user. It is flexible to respond to the capacity increase in installed power. Extremely environmentally friendly. It does not need any chemical materials and production methods used in the manufacture of batteries, capacitors and similar products. No large plants, molding technologies, etc. are required for the production of the system. The intermediate materials used for the production of the system are already produced and sold as standard in the market. The manufacturing process is fast and does not require processes that require special skills and advanced technology. This method is used to store the potential energy by using the force of gravity known for thousands of years. As a result of the obtained data and calculations, it was found that around 90% of the energy obtained from the panels can be recirculated to the grid. But this efficiency is around 95%

in conventional batteries and 99% in Lithium Ion batteries. However, this situation eliminates the majority of the gain obtained due to the renewal after the battery is out of use. In other words, battery efficiency, which is actually at 99%, eliminates this advantage of material loss battery systems that result from replacement costs. In the potential energy storage system, the efficiency, which is 90%, remains constant around this value and there is no decrease during use.

REFERENCES

[1] Mclarnon FR, Cairns EJ (1989) Energy storage. Ann Rev Energy.14:241–71.

[2] Dti Report. (2004) Status of electrical energy storage systems. dg/dti/ 00050/00/00, urn number 04/1878, UK department of tradeand industry. 1–24.

[3] Chen H, Cong TN, Yang W, Tan C, Li Y, Ding Y (2009) Progress in electrical energy storage system: A critical review, Progress in Natural Science. 19(3):291-312.

[4] Walawalkar R, Apt J, Mancini R (2007) Economics of electric energy storage for energy arbitrage and regulation. Energy Policy. 5:2558–68.

[5] Backhaus SN, Chertkov M, Dvijotham K (2011) Operations-based planning for placement and sizing of energy storage in a grid with a high penetration of renewable. Report no. LA-UR-11-03619. Los Alamos National Laboratory.

[6] IEC (2012) Grid integration of large-capacity renewable energy sources and use of large-capacity electrical energy storage.

[7] Ruoso AC, Caetano NR, Rocha LAO (2019) Storage Gravitational Energy for Small Scale Industrial and Residential Applications, İnventions, 4 (64):1-13.

[8] Wang D, Ren C, Sivasubramaniam A, et al. Energy storage in datacenters: what,where, and how.

[9] Swierczynski M, Teodorescu R, Rasmussen CN, et al. (2010). Overview of the energy storage systems for wind power integration enhancement. In: Proceedings of IEEE international symposium on industrial electronics, Bari, Italy, July 4–7.

[10] Energy storage for grid connected wind generation applications (2004) EPRI-DOE handbook supplement.

[11] Zafirakis D, Chalvatzis KJ, Baiocchi G, et al. (2013) Modeling of financial incentives for investments in energy storage systems that promote the large-scale integration of wind energy. Appl Energy. 105:138–54.

[12] Linden S (2006) Bulk energy storage potential in the USA, current developments and future prospects. Energy. 31:3446–57.

[13] Kondoh J, Ishii I, Yamaguchi H, et al. (2000) Electrical energy storage systems for energy networks. Energ Convers Manage. 41:1863–74.

[14] Suzuki Y, Koyanagi A, Kobayashi M (2005) Novel applications of the flywheel energy storage system. Energy. 30:2128–43.

[15] http://www.beaconpower.com/products (2007).

[16] Najjar Y, Zaamout MS (1998) Performance analysis of compressed air energy storage (CAES) plant for dry regions. Energy Convers Manage. 39:1503–11.

[17] Sears JR (2004) TEX: The next generation of energy storage technology. Telecommunications Energy Conference, INTELEC 2004. In: 26th annual international. 23; 218–22.

[18] Najjar Y, Jubeh N (2006) Comparison of performance of compressed-air energy-storage plant with compressed-air storage with humidification. In: Proceeding of IMechE, Part A: Journal of Power and Energy.220:581–8.

[19] Wang S, Chen G, Fang M, et al. (2006). A new compressed air energy storage refrigeration system. Energ Convers Manage. 47:3408–16.

[20] Bueno C, Carta JA (2006) Wind powered pumped hydro storage systems, a means of increasing the penetration of renewable energy in the Canary Islands. Renew Sus Energy Rev.10:312–40.

[21] Aneke, M., Wang, M (2016) Energy storage technologies and real life applications—A state of the art review. Appl. Energy. 179:350–377.

[22] Botha, C.D. Kamper, M.J (2019) Capability study of dry gravity energy storage. J. Energy Storage. 23: 159–174.

[23] Connolly D (2007) An Investigation into the energy storage technologies available for the integration of alternative generation techniques.

[24] IEC (2011) Electrical energy storage white paper.

OPTIMIZATION OF NACA 4412 AIRFOIL USING TAGUCHI METHOD

Veysel EROL[1]

Ahmet ŞUMNU[2]

Yüksel ERASLAN[3]

1. INTRODUCTION

Early in the 20th century, the National Advisory Committee for Aeronautics (NACA) revealed 4-digit airfoil family that completely changed the perspective of aircraft designers. These airfoils proposed increased lift and decreased drag, which results in improved flight performance for aerial vehicles. During an aircraft design process, the airfoil has a significant influence on aerodynamic performance, in other words efficiency. For instance, research by (Anderson and Hunter, 1987) emphasize the importance of ideal wing forms and how they help to increase lift and decrease drag. Their 4-digit naming convention defined their shape. The maximum camber is represented by the first two digits, and its location with respect to the chord length is indicated by the last two digits (Bramantya and Ginting, 2020). Because of their uniform shapes, engineers were able to optimize lift at varying speeds and produce more effective

[1] Research Assistant, İskenderun Technical University, Faculty of Aeronautics and Astronautics, Aerospace Engineering Department, veysel.erol@iste.edu.tr, ORCID: 0009-0001-1290-079X.

[2] Assist. Prof. Dr., İskenderun Technical University, Faculty of Aeronautics and Astronautics, Aerospace Engineering Department, ahmet.sumnu@iste.edu.tr, ORCID: 0000-0003-1514-6048.

[3] Lect. Dr., İskenderun Technical University, İskenderun Vocational School, Unmanned Aerial Vehicle Technology and Operatorship Program, yuksel.eraslan@iste.edu.tr, ORCID: 0000-0002-5158-5171.

and predictable wing designs. NACA 4-digit airfoils continue to be essential for increased aerodynamic performance and have made major contributions to the improvements of current aircraft designs.

Figure 1. Airfoil's Geometry

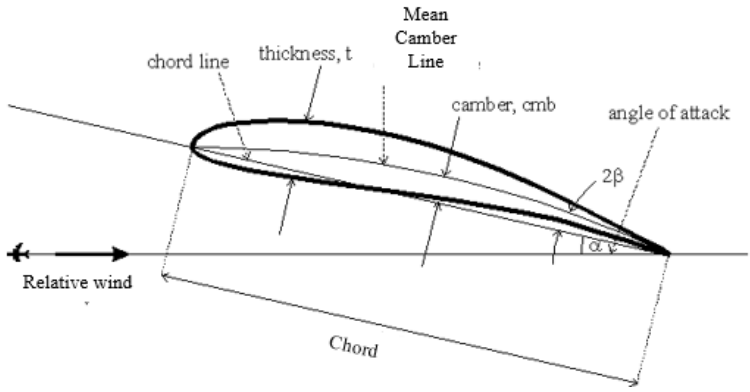

Source: (Kandwal and Singh, 2012)

Optimization studies on aircraft wings to increase aerodynamic performance have developed extensively and revealed the intersection of computational fluid mechanics and optimization techniques. The study by (Lam, 2020) investigated wing shape optimization for improved aerodynamic performance, emphasizing the use of genetic algorithms. Additionally, (Benaouali and Kachel, 2019) introduced multidisciplinary optimization by considering structural and aerodynamic aspects in wing design. (Lyu, Xu and Martins, 2014) focused on modifying wings using optimization methodologies to increase adaptability in flight conditions. (Wang, 2011) takes a different tack and offers a strong airfoil optimization platform built on a modified version of the particle swarm optimization technique. By expressing particle velocity in relation to position and its variation, the approach incorporates second-order precision. Furthermore, to improve global convergence and variety, an oscillating term was included. Over a broad design range, the

optimization platform successfully enhanced the aerodynamic properties of airfoils. These references express various approaches and advances in optimizing aircraft wings, increasing efficiency and performance.

Developments in aircraft engineering indicate the need for Computational Fluid Dynamics (CFD). Sources that address CFD applications in aerodynamic shape optimization, emphasizing its function in aerodynamics optimization, include the study by (van Stratan, Roy and San, 2023). (Sun et al., 2023) looked into how CFD affected noise reduction tactics. Additionally, (Suresh, Ramesh and Paramaguru, 2015) looked into how CFD might be used to simulate complex flow characteristics around wings. In another study, the author (Jain, Jain and Bajpai, 2016) focused on 3D wing design for a commercial aircraft using the NACA 2415 airfoil, known for its high L/D ratio at low Reynolds and Mach numbers. The wing with specific dimensions and dihedral angle was analysed using the Spalart-Allamaras turbulence model in ANSYS Fluent to investigate the lift coefficient, drag coefficient and lift/drag at various angles. (Seeni and Rajendran, 2019) focused on validating the CFD method to test the NACA 0009 airfoil at ultra-low Reynolds number of 20000. ANSYS Fluent was used to compare numerical results with experimental data based on literature. Using a coarse grid and a realizable k-epsilon turbulence model, the study shows positive predictions for a variety of angles of attack. (Mehdi, Gaurav and Sharma, 2017) look at the effect of aerodynamic performance on the two-dimensional NACA4412 airfoil. The computational approach uses the Spalart-allmaras turbulence model, which is steady state, incompressible, and finite volume method. Equations for continuity and Navier-Stoke were used to study the flow. At various angles of attack (3, 6 and 9 degrees) and Reynolds numbers ($1x10^6$, $2x10^6$, $3x10^6$, and $4x10^6$), numerical simulations were carried out. Moreover, based on a study by

(Nordanger et al., 2015) concerns efforts to perform a CFD simulation of airflow through a fixed 2D NACA0015 airfoil at high Reynolds number ($Re = 2.5 \times 10^6$) using linear, quadratic, and isogeometric finite element methodology. The current study uses the Spalart-Allmaras turbulence model combined with the Navier-Stokes solver based on the Chorin projection method, the first development of its kind in the isogeometric finite element framework. ANSYS Fluent was used to quantitatively assess the lift and drag coefficient performances of the NACA-0009 and NACA-4415 airfoils at different angles of attack. The optimal levels and effects of control factors (angles of attack and airfoil types) are demonstrated by statistical analyses using the L16 orthogonal array based on the Taguchi method (Evran and Yıldır, 2023). The technical report by (Echavarria et al., 2022) focused on optimizing airfoil shapes for aerodynamic platforms by employing particle swarm optimization, XFOIL, and OpenFOAM. The airfoil shape equations are developed to achieve the best lift-drag ratio, considering specific lift coefficients and Reynolds numbers. The authors (Strelets et al., 2023) discuss multi-point optimization of the airfoil for the Long Endurance Mars Exploration Flying Vehicle considering assorted constraints, including in-flight Reynolds number variation. CFD, specifically ANSYS Fluent, has been used to predict aerodynamic coefficients in Martian atmospheric conditions.

In this study, it is aimed to optimize NACA 4412 airfoil in the matter of its aerodynamic performance defined as the lift-to-drag ratio. In that context, firstly, aerodynamic performance investigation of the base airfoil is performed on ANSYS Fluent using SST k-omega turbulence model and validated with the existing experimental results from (Abbot et al., 1931) at $3x10^6$ Reynolds number. Furthermore, an optimization is carried out by means of the airfoil geometrical parameters of maximum camber, maximum camber position and thickness. In conclusion, the

applied Taguchi Method is provided remarkable lift/drag improvement, which is a well-known parameter, and defined as the target to be maximized during the optimization.

2. MODEL AND METHOD

2.1. Airfoil Geometry and Mesh Structure of Computational Domain

A two-dimensional model of the airfoil was created in ANSYS Design Modeler. The outline of the geometric model of the airfoil used is shown in Figure 2. The number of mesh elements was produced nearly 50000 to 1.1 million. Growth rates are varied according to network density.

Figure 2. Mesh Distribution Around the Airfoil

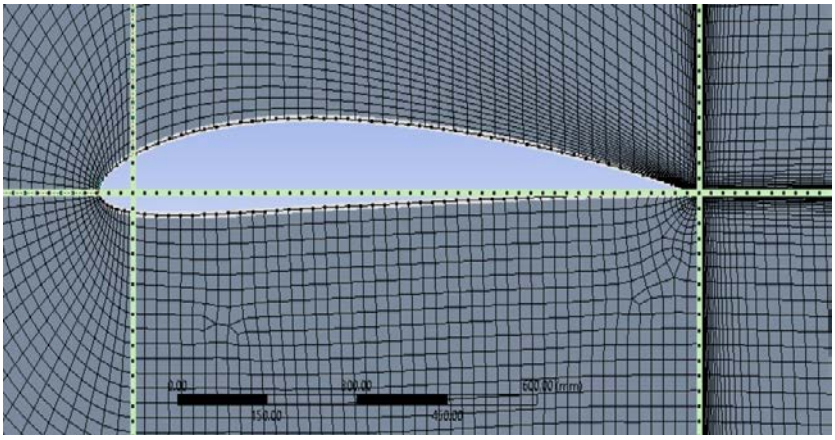

The computational domain and grid structure are created using ANSYS Design Modeler and ANSYS Mesher. The calculation area is modelled as C-shape, five times longer from the tip of the airfoil up and down, and 10 times longer from right to left and given in Figure 3. For quadrilateral elements and regular elements, a method was used in which the flow field was divided into four regions.

Figure 3. Mesh Representation on C Shape Computational Domain

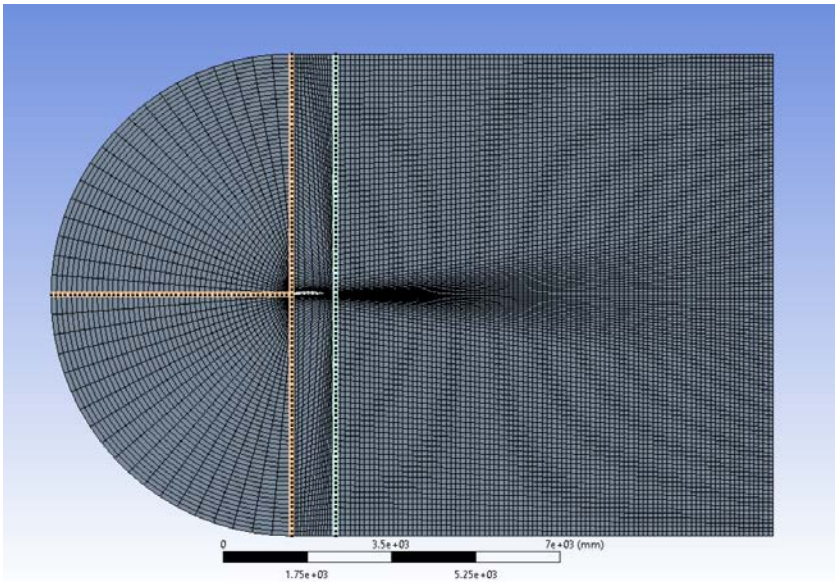

Figure 4. C_l Value Varying with Number of Mesh Elements

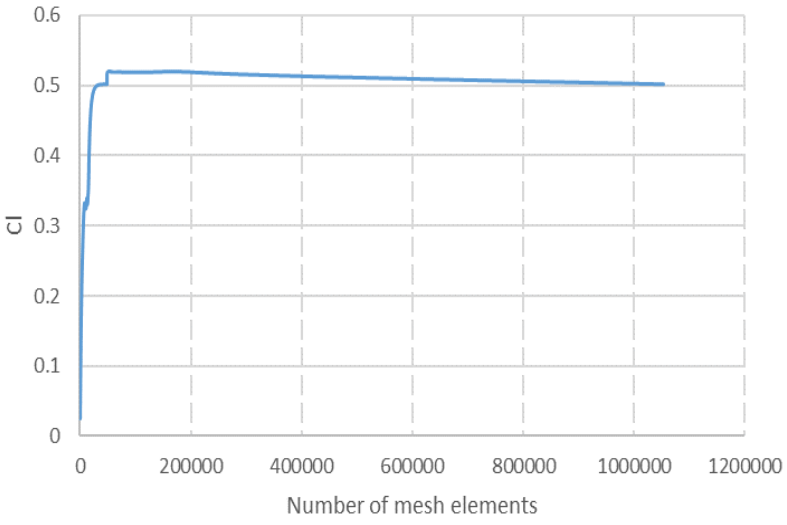

2.2. Flow Solver

In this study, the Fluent flow solver in ANYS was used to obtain the flow field around C_l/C_d and the geometry. SST *k-ω* turbulence model was used to solve airfoil aerodynamics. The SST *k-ω* method combines the *k-*ε and *k-ω* turbulence models, offering accurate predictions for boundary layer and free shear flows. Developed by (Menter 1994), the SST model addresses deficiencies in *k-*ε models. It provides robust turbulence modelling, making it widely applied in aerodynamics and fluid dynamics simulations. This turbulence model has been used in various studies (Mehdi et al., 2017; Wang et al., 2012). *k* and ω transport equations according to the SST k-ω model (Ansys Inc. 2010):

$$\frac{\partial}{\partial t}(\rho k) + \frac{\partial}{\partial x_i}(\rho k u_i) = \frac{\partial}{\partial x_j}\left(\Gamma_k \frac{\partial k}{\partial x_j}\right) + \bar{G}_k - Y_k + S_k \quad (1)$$

$$\frac{\partial}{\partial t}(\rho \omega) + \frac{\partial}{\partial x_i}(\rho \omega u_i) = \frac{\partial}{\partial x_j}\left(\Gamma_\omega \frac{\partial \omega}{\partial x_j}\right) + G_\omega - Y_\omega + D_\omega + S_\omega \quad (2)$$

In which $\bar{G}_k$ denotes the generation of turbulence kinetic energy due to mean velocity gradients. G_ω is generation of ω. Γ_k and Γ_ω show the effective diffusivity of k and ω. Y_k and Y_ω indicate dissipation of k and ω due to turbulence. Also D_ω is used as cross-diffusion term. The effective diffusivities for the SST k - ω model are given by

$$\Gamma_k = \mu + \frac{\mu_t}{\sigma_k} \quad (3)$$

$$\Gamma_w = \mu + \frac{\mu_t}{\sigma_\omega} \quad (4)$$

μ_t is the turbulent viscosity. σ_k and σ_ω are the turbulent Prandtl numbers.

$$\tilde{G}_k = min(G_k, 10\rho\beta^* k\omega) \quad (5)$$

$$G_\omega = \frac{\alpha}{v_t}\tilde{G}_k \quad (6)$$

$\tilde{G}_k$ represents the production of turbulence kinetic energy. G_ω represents the production of ω.

$$Y_k = \rho\beta^* k\omega \quad (7)$$

$$Y_\omega = \rho\beta\omega^2 \quad (8)$$

Y_k shows dissipation of turbulence kinetic energy and Y_ω represents the dissipation of ω.

$$D_\omega = 2(1 - F_1)\rho\sigma_{\omega,2}\frac{1}{\omega}\frac{\partial k}{\partial x_j}\frac{\partial \omega}{\partial x_j} \quad (9)$$

D_ω is cross-diffusion term.

Convergence occurred within 210 iterations. The calculation run is completed when the flow residuals reach 10^{-6}.

The convergence of the solution is shown in Figure 5, which shows the solution residuals. Table 1 indicates setup parameters.

Table 1. Setup Parameters

Number	Parameters	Values
1	Fluid	Air
2	Density	1.225 kg/m^3.
3	Viscosity	1.802* 10^{-5}kg/m-s
4	Inlet Velocity	43.9m/s
5	Turbulence Model	SST-*k*-omega
6	Momentum	Second Order Upwind
7	Pressure	Second Order
8	Turbulent kinetic Energy	Second Order Upwind
9	Gradient	Least Squares Cell Based
10	Chord	1m

Figure 5. Residuals Versus Iterations and

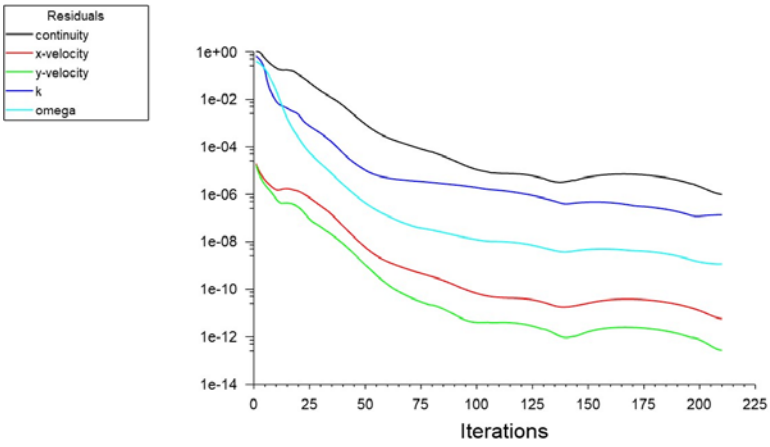

2.3. Computational Fluid Dynamics Solution

In this section, the model is presented with experimental studies to demonstrate the validation of the CFD solution for the NACA4412 airfoil. These values were compared with the experimental results of the NACA4412 airfoil studied by (Abbot et al., 1931). CFD solution results were obtained using the SST *k*-

omega turbulence model. Table 2 represents the experimental results performed and Fluent results.

Table 2. Differences Between the Experimental (Abbot Et Al., 1931) and Numerical Results.

Number of Elements	C_d (Fluent)	C_d (Exp)	Disc. %	C_l (Fluent)	C_l (Exp)	Disc. %
11500	0.00821	0.007	15.91	0.426771	0.43	0.754
187763	0.00827	0.007	16.64	0.440229	0.43	2.35
606079	0.00842	0.007	18.41	0.432643	0.43	0.613
1536807	0.00838	0.007	17.94	0.432646	0.43	0.613

Discrepancies between CFD solutions and experimental results may be due to experimental errors or uncertainties. Model asymmetries or dynamic model motion may be the possible cause of the measurements.

3. OPTIMIZATION

Improving the aerodynamic performance of aircraft is a very important task. The external structure of the aircraft is very important in respect of aerodynamic performance. There are many statistical and optimization methods created using disparate parameters. One of those methods is the Taguchi method (Hamzacebi et al., 2003). The purpose of this method is to find the maximum, minimum, and optimal values using a small number of variables. In this way, it can save time and computational costs (Semioshkina and Voigt, 2006). In this study, the Taguchi method was used to reach the maximum. CFD calculations were performed using the outputs of the L9 orthogonal array in the Taguchi method. There are three control factors in this experimental design adaptation (Sarin, 2014).

The maximum camber ratio was determined as the first control factor of the selected NACA4412 airfoil. The maximum camber was changed from 3.6 percent to 4.4 percent. As the second factor, the position of the maximum camber ratio in tenths

of the cord was determined. The maximum camber position was changed from 36 percent to 44 percent. Maximum thickness was chosen as the third factor. The maximum thickness in cords was changed between 10.8 and 13.2 percent. 9 different CFD analyses were applied based on the outputs of the Taguchi method. The control factors and control factor levels used in the calculations are shown in Table 3.

Table 3. Parameters

Factors	Icons	Levels		
Maximum Camber	A	3.6	4	4.4
Maximum Camber Position	B	36	40	44
Maximum Thickness	C	10.8	12	13.2

The C_l/C_d of the NACA4412 airfoil were selected as the output of the Taguchi method. As a result of the calculations, the "Larger is Better" methodology based on the Taguchi method was chosen to calculate the C_l/C_d. “Larger is Better” is stated in Equation 11 (Kong and Group n.d.), respectively.

$$S / N_L = -10\, log(\frac{1}{n}\sum\frac{1}{y_i^2}) \quad (11)$$

4. RESULTS AND DISCUSSION

The goal of the CFD study is to calculate lift and drag coefficients for different parameter values.

Table 4. CFD Results for L9 Orthogonal Array

Runs	Maximum Camber	Maximum Camber Position	Thickness	Results		
				Drag Coefficient (C_d)	Lift Coefficient (C_l)	C_l/C_d
1	3.6	36	10.8	0.01179	0.38607	32.74555
2	3.6	40	12	0.012506	0.36218	28.9605
3	3.6	44	13.2	0.013207	0.43368	32.83713

4	4.4	36	13.2	0.013844	0.46772	33.78503
5	4.4	40	10.8	0.013574	0.50115	36.91985
6	4.4	44	12	0.011739	0.48284	41.13127
7	4	36	12	0.012892	0.42683	33.10813
8	4	40	13.2	0.01183	0.42947	36.30347
9	4	44	10.8	0.0114	0.46412	40.71228

Lift and drag coefficients are determined in Table 4. Analysis of Variance (ANOVA) was run to show the dominant levels of the parameters and their effects on the C_l/C_d. Besides, the effect ratios of the parameters on the results were calculated using ANOVA. The analysis was performed according to the 95% confidence level. R-Sq =91.31% and R-Sq(adj) = 65.24 % the ANOVA results of the lift/drag based on are shown in Table 5.

Table 5. ANOVA Results for C_l/C_d

Source	DF	Seq SS	Contribution	Adj SS	Adj MS	F-Value	P-Value
Maximum Camber	2	60.53	47.79%	60.53	30.263	5.50	0.154
Maximum Camber Position	2	43.21	34.12%	43.21	21.606	3.93	0.203
Thickness	2	11.90	9.40%	11.90	5.952	1.08	0.480
Error	2	11.01	8.69%	11.01	5.503		
Total	8	126.65	100.00%				
R-sq 91.31% R sq(adj) 65.24%							

As seen in Table 5, the effect of the maximum camber ratio for Cl/Cd was calculated as 47.79%, the effect of the maximum camber position was 34.12% and the effect of the thickness was calculated as 9.40%.C_l/C_d error rate is 8.69%. In order to understand the effects of the parameters specified as input on C_l/C_d, the average data of C_l/C_d for all factors were solved based on all levels for CFD and S/N ratio data. The results obtained are shown in Table 6.

Table 6. Response Table for C_l/C_d

Level	S/N data (dB)			Means		
	Maximum Camber	Maximum Camber Position	Thickness	Maximum Camber	Maximum Camber Position	Thickness
1	31.28	29.96	30.43	31.51	33.21	36.79
2	30.64	31.26	30.59	36.71	34.06	34.40
3	30.70	31.40	31.60	37.28	38.23	34.31
Delta	0.64	1.45	1.18	5.76	5.01	2.48
Rank	3	1	2	1	2	3

From Table 6, the maximum C_l/C_dratio was obtained using the NACA4412 airfoil with the third level of parameters. Using the data in Table 6, a graph was created to statistically determine the effect of each parameter on C_l/C_d. The plots containing the influence of C_l/C_d control factors are shown in Figure 6, respectively.

Figure 6. Effects of a Maximum Camber, Maximum Camber Position and Thickness on Response

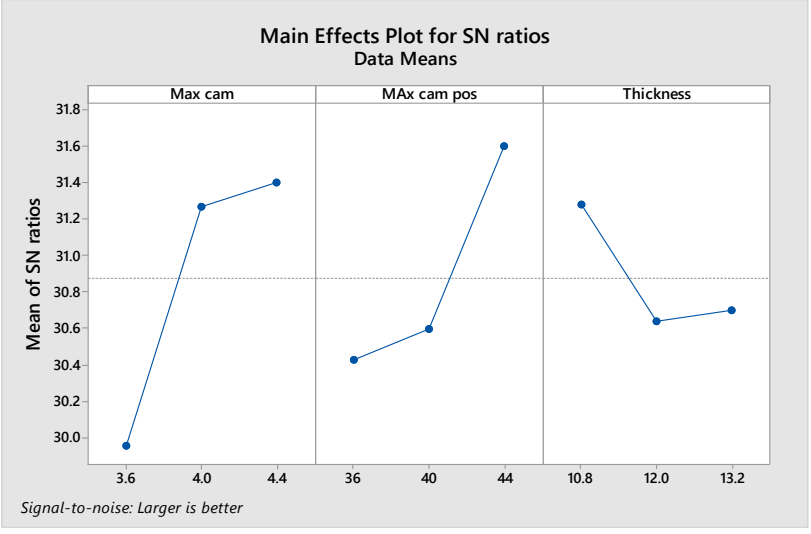

According to Figure 6, the resulting parameter combination leads to an increase in the Cl/Cd ratio. The maximum Cl/Cd ratio can be achieved using a maximum camber ratio of 4.4 percent, a maximum camber position ratio of 44 percent, and a thickness ratio of 10.8 percent.

Table 7. Original and Proposed Geometry

Geometry	Maximum Camber (%)	Maximum Camber Position (%)	Thickness (%)	Cl/Cd
NACA4412	4	40	12	32.002
Taguchi Design	4.4	44	10.8	41.895

As seen in Table 7, the difference between the original geometry and Taguchi's predicted results increases with maximum camber and thickness. Taguchi method outputs have been verified with CFD. Additionally, the pressure contour as a function of the optimal control coefficients for the Cl and Cd are shown in Figure 7.

Figure 7. Pressure Contour of Original NACA4412 (Left) and Modified NACA4412 (Right) Airfoils

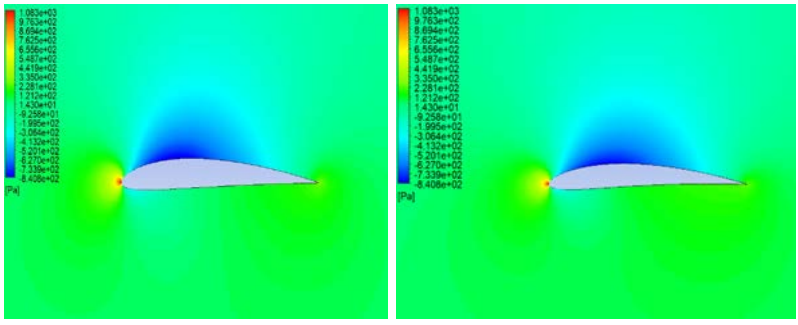

As can be seen in Figure 7, the change in shape causes pressure changes in different regions of the NACA4412 profile. It has been observed that in regions where the speed value is maximum, the pressure occurs at minimum value, while in regions where the pressure increases, the velocity occurs at minimum levels.

5. CONCLUSION

In this study, NACA 4412 airfoil was aimed to be optimized to have an improvement in its lift-to-drag ratio, that can be defined as aerodynamic performance. Aerodynamic analyses of the airfoil are performed on ANSYS Fluent using SST k-omega turbulence model and the results were validated from the experimental results in the literature. The optimization of the airfoil is carried out via Taguchi Method with variation in maximum chamber and location, and thickness of the geometry. The modified airfoil is evaluated again by using validated CFD analyses methodology and results shown that the effect of maximum camber on the Cl/Cd ratio was determined as 47.49%, the effect of maximum camber position as 34.12% and the effect of thickness as 9.4%. There was a 30.91% improvement in the Cl/Cd ratio of the modified NACA4412 airfoil compared to the base geometry.

REFERENCES

Anderson, John D., and Lloyd P. Hunter. 1987. Introduction to Flight . Vol. 40.

Benaouali, Abdelkader, and Stanisław Kachel. 2019. "Multidisciplinary Design Optimization of Aircraft Wing Using Commercial Software Integration." Aerospace Science and Technology 92:766–76. doi: 10.1016/j.ast.2019.06.040.

Bramantya, Muhammad Agung, and Ray Rhido Ribuna Ginting. 2020. "Study of the Effect of 4-Digit NACA Variation on Airfoil Performance Using Computation Fluid Dynamics." AIP Conference Proceedings 2248(July). doi: 10.1063/5.0013514.

Echavarria, Camilo, Jose D. Hoyos, Jesus H. Jimenez, Gustavo Suarez, and Andres Saldarriaga. 2022. “Optimal Airfoil Design through Particle Swarm Optimization Fed by CFD and XFOIL.” Journal of the Brazilian Society of Mechanical Sciences and Engineering 44(11):1–17. doi: 10.1007/s40430-022-03866-4.

Evran, Savaş, and Salih Zeki YILDIR. 2023. “Numerical and Statistical Aerodynamic Performance Analysis of NACA0009 and NACA4415 Airfoils.” Journal of Polytechnic 0900:0–2. doi: 10.2339/politeknik.1229081.

Jain, Rohit, Sandeep Jain, and Lokesh Bajpai. 2016. “Investigation on 3-D Wing of Commercial Aeroplane with Aerofoil NACA 2415 Using CFD Fluent.” International Research Journal of Engenieering and Technology (IRJET) 4(06, 2016):2321–0613.

Kandwal, S., and S. Singh. 2012. “Computational Fluid Dynamics Study Of Fluid Flow And Aerodynamic Forces On An Airfoil.” International Journal of Engineering Research & Technology (IJERT) 1(7):1–8.

Kong, Ting, and The Advantage Group. n.d. “Taguchi Methods in Experimental Design.” 139–48.

Lam, Xuan-Binh. 2020. “Multidiscilinary Design Optimization for Aircraft Wing Using Response Surface Method, Genetic Algorithm, and Simulated Annealing.” Journal of Science and Technology in Civil Engineering (STCE) - NUCE 14(1):28–41. doi: 10.31814/stce.nuce2020-14(1)-03.

Lyu, Z., Z. Xu, and J. R. R. A. Martins. 2014. “Benchmarking Optimization Algorithms for Wing Aerodynamic Design Optimization.” The Eighth International Conference on Computational Fluid Dynamics 18.

Mehdi, Husain, Shwetanshu Gaurav, and Mudit Sharma. 2017. "Numerical Investigation of Fluid Flow and Aerodynamic Performance on a 2D NACA-4412 Airfoil." International Journal of Research in Engineering and Innovation 1(1):1–5.

Menter, F. R. 1994. "Two-Equation Eddy-Viscosity Turbulence Models for Engineering Applications." 32(8).

No, Report. 1931. "The National Advisory Committee for Aeronautics." Science 74(1923):451. doi: 10.1126/science.74.1923.451.

Nordanger, Knut, Runar Holdahl, Trond Kvamsdal, Arne Morten Kvarving, and Adil Rasheed. 2015. "Simulation of Airflow Past a 2D NACA0015 Airfoil Using an Isogeometric Incompressible Navier-Stokes Solver with the Spalart-Allmaras Turbulence Model." Computer Methods in Applied Mechanics and Engineering 290:183–208. doi: 10.1016/j.cma.2015.02.030.

Sarin, Sanjiv, and North Carolina Agricultural. 2014. "Teaching Taguchi ' ' s Approach to Parameter Design Teaching Taguchi ' s Approach to Parameter Design Sanjiv Sarin." (September).

Semioshkina, Natalia, and Gabrielle Voigt. 2006. "An Overview on Taguchi Method." Journal Of Radiation Research 47 Suppl A(2):A95–100.

van Stratan, G. S. M., Sukanta Roy, and Yam Ke San. 2023. "Aerodynamic Shape Optimization of a NACA0018 Airfoil Using Adjoint Method and Gradient-Based Optimizer." MATEC Web of Conferences 377:01016. doi: 10.1051/matecconf/202337701016.

Strelets, Dmitry, Egor Parkhaev, Andrey Fevralskikh, Djahid Gueraiche, and Debopam Das. 2023. "Airfoil

Optimization Methodology and CFD Validation for Mars Atmospheric Conditions." Aerospace Systems 6(1):175–86. doi: 10.1007/s42401-022-00181-7.

Sun, Jianwei, Koichi Yonezawa, Yasutada Tanabe, Hideaki Sugawara, and Hao Liu. 2023. "Blade Twist Effects on Aerodynamic Performance and Noise Reduction in a Multirotor Propeller." Drones 7(4):1–18. doi: 10.3390/drones7040252.

Suresh, C., K. Ramesh, and V. Paramaguru. 2015. "Aerodynamic Performance Analysis of a Non-Planar C-Wing Using CFD." Aerospace Science and Technology 40:56–61. doi: 10.1016/j.ast.2014.10.014.

Wang, Shengyi, Derek B. Ingham, Lin Ma, Mohamed Pourkashanian, and Zhi Tao. 2012. "Turbulence Modeling of Deep Dynamic Stall at Relatively Low Reynolds Number." Journal of Fluids and Structures 33:191–209. doi: 10.1016/j.jfluidstructs.2012.04.011.

Wang, Yuan-yuan. 2011. "Robust Airfoil Optimization Based on Improved Particle Swarm Optimization Method ∗." 32(10):1245–54. doi: 10.1007/s10483-011-1497-x.

Hamzacebi, C., Kutay, F. (2003). Taguchi method: An application. 6(3-4) , 7 - 17.

Ansys Inc. 2010. "Ansys Fluent 15.0 - Theory Guide." ANSYS Inc., USA 15317(November):0–746.

EVALUATION OF DYNAMIC BEHAVIOR OF STRUCTURES

Emre ALPASLAN[1]

1. INTRODUCTION

Generally speaking, mathematical or numerical models are developed in all engineering domains to understand the behavior of real systems. These models serve a wide range of applications, but they can be broadly categorized into three categories: analysis, prediction, and design. New and powerful numerical methods have been developed to examine the behavior of such models, which are used for the design of engineering structures, under static and dynamic loads. The finite element method (FEM) is generally preferred because it is fast and economical in creating numerical modeling of structures and examining their behavior. One of the most popular techniques in civil engineering for determining how a structure would behave under dynamic loads like earthquakes, wind, traffic, and explosions is the use of finite element (FE) models. These FE models include studies carried out to determine the behavior of some or all of the structures (Betti and Galano, 2012; Ural and Celik, 2018).

Many assumptions are made in theoretical analyses when creating the FE model of the structure as a result of the creation of new, high-performance materials the intricate nature of constructed systems becoming more complex, and the existence of many unknown and uncertain system parameters like boundary

[1] Assist. Prof. Dr., Ondokuz Mayıs University, Faculty of Engineering, Department of Civil Engineering, emre.alpaslan@omu.edu.tr, ORCID: 0000-0002-3715-990X.

conditions, loads, and geometric and material features for developing numerical models. Additionally, the assumptions made when building structures must be simplified due to a lack of knowledge or other constraints. In addition, in existing structural systems, building materials lose their strength, deformations that may occur over time, excessive and irregular loading due to misuse, ground settlements, environmental effects (such as earthquake, flood, wind, and explosion effects), and accidents that are likely to occur. Uncertainty of damages can also reduce the accuracy and validity of numerical models. Due to such factors, the SE model created to represent the current structure fully is an approach far from reality. The main reasons for errors that may occur in terms of the created SE model being able to represent the real structure are as follows (Raineri and Fabbrocino, 2014);

i) Structural model errors: These types of errors, which may occur when there is uncertainty regarding the creation of physical equations, are typically caused by factors such as junction points of elements, welded elements, damping, etc., which are difficult to model in a particular engineering system.
ii) Errors in model parameters: They arise due to inaccurate assumptions made to facilitate the model to be created, difficulties that may be encountered in determining material properties, and the application of inappropriate boundary conditions.
iii) Complex structural system errors: Errors occur due to insufficient models created for non-linear systems.

Due to such uncertainties, the finite element model created must be compared with experimentally obtained data to reflect the behavior of the structure more realistically. The modal analysis method is one of the most effective methods in obtaining the dynamic behavior of structures experimentally. In the modal

analysis method, natural frequencies, natural mode shapes, and natural damping ratios, which are called the modal dynamic parameters of the structure, are obtained. The three steps followed in the modal analysis method are as follows;

- Planning and execution of tests (correct placement of sensors, choosing the parameters for data gathering and using vibration)
- Data processing and determination of modal parameters (filtering, breaking, windowing, extraction of modal parameters)
- Validity of the modal model

Once the modal model is obtained, it can be used for the following purposes:

1. Obtaining vibration characteristics and solving problems to understand the causes of problems that may be encountered in real life, such as excessive vibration and noise
2. In health monitoring and damage detection of buildings to determine the existence, location, and importance of any damage that may occur in the structure by comparing the model parameters obtained from the current state of the buildings with the modal parameters taken previously as a reference
3. To update the model; In the development of the SE model using experimentally obtained modal parameters, to more accurately obtain the real behavior of structures with complex structural systems and uncertain material properties
4. In sensitivity analyses carried out to understand the effects of any repair and strengthening that may be made in the structure on the dynamic behavior of the structure
5. In performance evaluations and damage detection studies carried out on the SE model created to determine the

dynamic performance of building systems using modal parameters and mode shapes

2. EVALUATING EXPERIMENTAL MODAL PARAMETERS

The studies with items 1 and 2 mentioned above include experimental modal analysis applications. Experimental modal analysis methods include forced vibration tests (FVT), free vibration tests, and operational modal analysis (OMA) tests (Zhang, 2013). FVT is carried out by applying vibrations of known amplitude and change over time to the structure to be studied and measuring the vibration signals formed in the structure under these vibrations. The dynamic properties and direction of these externally generated vibrations are controlled. These vibrations and the vibrations they create in the structure are measured simultaneously. In the free vibration test, some initial states are applied to the structure (usually initial displacement). Under these initial states, the dynamic behavior occurring in the structure is examined by leaving it in free vibration. The modal parameters of the structure in the OMA test are obtained as a result of examining the vibrations occurring in the structure under natural (random) source vibrations whose amplitude and change over time are unknown. Natural vibrations are generally caused by traffic load, human load, wind effect, wave effect, and ground movements. The OMA method has taken an important place in civil engineering in recent years in examining the structural systems of buildings exposed to random or natural vibrations under their current conditions. It is widely used in many other engineering fields, including mechanical engineering, as it has important advantages such as being fast and economical in its application and providing the opportunity to examine the current situation of the entire structural behavior. There are many

successful studies in the literature using the OMA method. In the field of civil engineering, bridges (Chen et al. 2017; Rainieri et al. 2020; Hasani and Freddi 2023) buildings (Amaddeo and Dom 2023; Shim and Park 2023) historical structures (Ramos et al. 2010), marine structures (Maetz et al. 2023), wind turbines (Ibsen and Liingaard 2005), dams (Baptista et al. 2005) and stadiums (Reynolds et al. 2005), the OMA method has been successfully applied.

2.1. Operational Model Analysis Method

In the operational modal analysis (OMA) method, the vibrations affecting the structure are unknown. These vibrations consist of environmental effects; The dynamic characteristics of structures can be determined experimentally by processing the responses to vibrations in the time and frequency environment. Since the vibrations are of environmental origin, the amplitude of the vibrations affecting the structure and the resulting change over time cannot be known. Natural sources of vibration are sometimes traffic or pedestrian load, sometimes they can be caused by ground tremors, and sometimes they can be caused by wind. Noise can have negative effects on buildings. In this case, it is important to choose the correct method of processing the reactions caused by vibrations and to eliminate this negativity with the chosen method. The flow chart showing the determination of the dynamic properties of structures in this method is shown in Figure 1 (Türker, 2011).

Devices that transfer the reactions such as displacement, speed, and acceleration occurring in the building system in the form of a proportional electrical signal to a data-receiving unit ready for signal processing are called transducers. Accelerometers are the most preferred type of transducers due to their features such as having wide frequency and dynamic range and being relatively small and light. As an example of accelerometers that can be used

in measurements, high-sensitivity field-type single and three-axis accelerometers are shown in Figure 2. General information about these accelerometers is presented in Table 1.

Figure 1. Operational Modal Analysis Method Measurement Setup

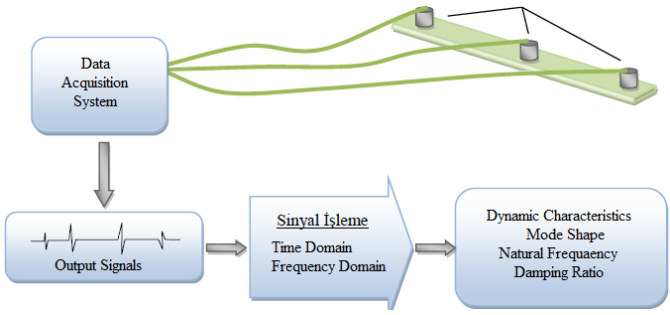

Figure 2. Types of Accelerometers That can be Used in Experimental Studies

Table 1. Accelerometer information

Type	Force/electro-dynamic feedback
The largest acceleration measurement range	± 3g
Frequency range	0.1-120 Hz
Sensitivity	2400 mV/g
Shock resistance	2000 g
Operating temperature	-40oC to +65oC

2.1.1. Data Acquisition System and Signal Processing

Data acquisition devices are defined as a device that converts analog data into digital data at certain time intervals. A computer, specialized software, and a data collection unit make up the data collection system. The vibration signals that are supplied from the accelerometers to the computer program are

transferred via the data acquisition unit. In collecting and processing vibration signals stored in the computer environment, special software is used as the element that provides the necessary interface.

Data acquisition devices used in experimental measurements can generally process signals at high speeds and with high resolution from many voltage output sensors such as acceleration sensors, load cells, strain washers, and displacement meters. The technical specifications of the data collection device, which has 4 channels and can sample all channels simultaneously, are shown in Table 2. Additionally, an example of the data acquisition system is shown in Figure 3.

In experimental studies to be carried out; It is necessary to use software that is compatible with the dynamic data acquisition system to be used in the experimental study, in introducing the accelerometers to the data acquisition unit, collecting the vibration signals in the data acquisition unit, performing signal conditioning operations and transferring them to the computer-based signal processing program.

2.1.2. Enhanced Frequency Domain Decomposition (EFDD) Method

The Frequency Domain Decomposition (FDD) Method is improved upon by the EFDD Method, which is based on the frequency domain. Here, there are a few benefits to using the EFDD approach rather than the FDD method. For instance, the EFDD approach allows for the determination of modal damping ratios in addition to natural frequencies and mode shapes. Additionally, since it is a process that requires the selection of peaks, it has some disadvantages. Because the selection of peaks is not objective but subjective and therefore the reliability of the results decreases.

Table 2. Data Acquisition Unit Technical Specifications

Measurement Resolution 2	4 Bit
Communication Interface	Ethernet
Number of Channels	4 (synchronization with GPS option)
Channel Measurement	Differential
Synchronization	True simultaneous
Data Acquisition Rate	4 kHz (4000 samples/sec) / Channel - Independent of the number of channels
Filtering	Anti-Aliasing / Low Pass
Dynamic Input Range	140dB
Measurement Range	±5.5 V (standard), ±12 V (PGA option),
Channel Gains	1/8, ¼, ½, 1, 2, 4, 8, 16, 32, 64, 128 times - each channel can be adjusted independently (PGA option)
Sensor Excitation Voltage	+5V, +12V, -12V
Power Requirement	12V DC, maximum 40W
Operating Temperature	10ºC-35ºC - Recommended 25ºC
Storage Temperature	0ºC-50 ºC
Digital Infrastructure	ARM Cortex microcontroller, embedded Linux operating system (optional)

Figure 3. Dynamic Data Collection Device and Acceleration Recording System

Since the damping is calculated based on the maximum amplitude, the accuracy of the maximum amplitude also affects the damping to be determined and the reliability of the damping estimates decreases. Although it has advantages and

disadvantages, the EFDD method is widely used in the signal processing stage of modal analysis. The theoretical relationship of this method under environmental vibration under the unknown impact force and measurable reaction force, that is, the behavior function is expressed as (Brincker et al. 2000);

$$G_{yy}(j\omega) = H(j\omega)^{*} G_{xx}(j\omega) H(j\omega)^{T} \quad (1)$$

Here, G_{xx} (jω) represents the Power Spectral Density (PSD) function of the effect signal, G_{yy} (jω) indicates the PSD function of the response signal, and H(jω) represents the frequency response function. In Equation (1), * and T indicate the complex conjugation and transpose of expressions, respectively. After mathematical arrangements, the PSD function of the response signal is in the form of a unipolar residual value function is defined by;

$$H(j\omega) = \sum_{k=1}^{n} \frac{R_k}{j\omega - \lambda_k} + \frac{R_k^*}{j\omega - \lambda_k^*} \quad (2)$$

In this formula, n denotes the mode number, λ_k denotes the polar function, and R_k denotes the residual value function. After the necessary arrangements are made, it can be obtained by follow;

$$G_{yy}(j\omega) = \sum_{k=1}^{n} \sum_{x=1}^{n} \left[\frac{R_k}{j\omega - \lambda_k} + \frac{R_k^*}{j\omega - \lambda_k^*} \right] G_{xx}(j\omega) \left[\frac{R_s}{j\omega - \lambda_s} + \frac{R_s^*}{j\omega - \lambda_s^*} \right]^{\tilde{H}} \quad (3)$$

Here, s denotes singular values, H denotes complex conjugate, and T denotes transpose. When the mathematical expressions are simplified, the PSD function of the response signal is in the form of a unipolar residual value function is obtained as;

$$G_{yy}(j\omega) = \sum_{k=1}^{n} \frac{A_k}{j\omega - \lambda_k} + \frac{A_k^*}{j\omega - \lambda_k^*} + \frac{B_k}{-j\omega - \lambda_k} + \frac{B_k^*}{-j\omega - \lambda_k^*} \quad (4)$$

Here A_k denotes the k residual value matrix of the PSD function of the response signal. The first step in the GFTAA method is to determine the PSD matrix. The estimate of the PSD

of the response signal at discrete frequencies is known as $\omega = \omega_i$ and then it is separated by taking the singular value separation matrix. According to this it can be expressed as;

$$G_{yy}(j\omega_i) = U_i S_i U_i^{\bar{H}} \quad (5)$$

Here u_{ij} is the singular vectors, $U_i = [u_{i1}, u_{i2} \ldots u_{im}]$ is the whole matrix containing the singular vectors, s_{ij} is the scalar singular values and $S_i = [s_{i1}, s_{i2} \ldots s_{im}]$ is the diagonal matrix containing the scalar singular values. In the PSD function, the points giving peak values correspond to natural frequencies. The singular vectors (u_{ij}) that form the peaks correspond to natural mode shapes.

2.1.3. Stochastic Subspace Identification (SSI) Method

SAB method is a method that works directly in the time domain and gives data, and in this case, there is no need for spectral transformation or correlation. In this method, negative effects caused by noise can be intervened and it is a suitable and useful method for determining dynamic characteristics. The formulations and relations taken into account in this method are given below, depending on the equations of motion; The dynamic behavior of the building system is seen as a linear, constant-coefficient second-order differential equation (Overschee and De Moor, 2012);

$$[M]\{\ddot{U}(t)\} + [C]\{\dot{U}(t)\} + [K]\{U(t)\} = \{R(t)\} = [B]\{u(t)\} \quad (6)$$

Here; [M], [C], [K] denote the mass, damping, and stiffness matrices of the system, respectively, R(t) denotes the vibration force, and $\{U(t)\}, \{\dot{U}(t)\}, \{\ddot{U}(t)\}$ denotes the time-dependent displacement, velocity, and acceleration vectors, respectively.

The {R(t)} force vector can be stated using the [B] matrix and {u(t)} vector, which symbolize the data in the environment.

Although the dynamic balance equation represents the behavior of the vibrating structure in Eq. (6), it is not suitable for the SSI method with this structure. Therefore, Eq. (6) is transformed into a more appropriate form, the discrete-time stochastic state-space model. The State-Space model, which is used in civil engineering to determine the dynamic properties of structures with viscous damping, is developed from control theory. Equation (6) can be expressed as following definitions,

$$x(t) = \begin{pmatrix} U(t) \\ \dot{U}(t) \end{pmatrix}, A_* = \begin{pmatrix} 0 & I_{n_2} \\ -M^{-1}K & -M^{-1}C \end{pmatrix}, B_* = \begin{pmatrix} 0 \\ M^{-1}B \end{pmatrix} \quad (7)$$

$$x(t) = A_* x(t) + B_* u(t) \quad (8)$$

Here, A_* is the state matrix, B_* is the data matrix and x(t) is the state vector.

It is impossible to measure every structural degree of freedoms in ambient vibration tests. Consequently, the number of independent variables characterizing the system's state equals the number of components in the state-space vector, and the observation equation is determined by;

$$y(t) = C_* x(t) + D_* u(t) \quad (9)$$

Here, C_* is the system behavior matrix and D_* directly refers to the transmission matrix. Eqs. (8) and (9) form the continuous-time specific state-space model. Here, it is stated that expressions with “Continuous Time” can be evaluated at any time t∈N. However, measurements are made at discrete times such as kΔt (k∈N). Sampling time and ambient noise always affect signal data. After sampling, the state-space model can be as follows;

$$\left.\begin{aligned} x_{k+1} &= A_* x_k + B_* u_k \\ y_k &= C_* x_k + D_* u_k \end{aligned}\right\} \quad (10)$$

Here, $x_k = x(k\Delta t)$ denotes the discrete-time state vector, u_k the distinct effect signal vector. Measurements made under

real operational conditions include signals related to the structure and external noise. Therefore, when stochastic noise components are added in Eq. (10), the specific-stochastic state-space model can be expresses as;

$$\left.\begin{aligned} x_{k+1} &= A_* x_k + B_* u_k + w_k \\ y_k &= C_* x_k + D_* u_k + v_k \end{aligned}\right\} \quad (11)$$

Here, w_k refers to the noise signals processed due to uncertainties and defects in the model, and v_k refers to the noise signal processed due to accelerometer defects. Both vectors consist of signals whose values cannot be measured. White noise and covariance matrices without effect can be identified as;

$$E_*\left[\begin{pmatrix} w_p \\ v_p \end{pmatrix}\begin{pmatrix} {w_q}^T & {v_q}^T \end{pmatrix}\right] = \begin{pmatrix} Q & S \\ S^T & R \end{pmatrix}\delta_{pq} \quad (12)$$

Here; E_* denotes the expected value operator and δ_{pq} Kronecker denotes the delta. Kronecker delta is a function of two variables and is expressed as follows;

$$\delta_{pq} = \begin{cases} 1, şayet & p = q \\ 0, şayet & p \neq q \end{cases} \quad (13)$$

In the SSI method, the behavior of the structural system is determined under normal operating conditions. In this case, it is not possible to distinguish the distinct signal data u_k shown in Eq. (11) from the noise terms w_k and v_k. For this purpose, the term u_k is written in terms of noise terms w_k and v_k, the discrete-time stochastic state-space model of the structure is given by;

$$\left.\begin{aligned} x_{k+1} &= A_* x_k + w_k \\ y_k &= C_* x_k + v_k \end{aligned}\right\} \quad (14)$$

Eq. (14) forms the basis of the time domain in determining dynamic characteristics from ambient vibrations.

3. MODEL UPDATING TECHNIQUES

3.1.Creating Initial Analytical Models

By using many software programs, FE models of structures can be created and the modal parameters of the structure, namely natural frequency and modal shapes, can be obtained. Different element types are offered in creating the FE model in different software. The type of structure desired to be created in the type of element to be selected is important. The material properties to be used for the initial FE model of the buildings can be determined by using non-destructive test methods (Schmidt hammer, ultrasonic testing device) in the field, depending on the suitability of the structures. In cases where this is not possible, it can be determined based on studies conducted in the literature. In the initial FE model, the assumption of linear elastic material behavior is generally valid. The boundary conditions of the structures can be modeled as simple, fixed support etc. depending on the ground conditions.

3.2.FE Model Updating

The studies containing the 3rd, 4th, and 5th items mentioned in the previous section include applications made by creating an analytical model. Due to the uncertainties in the initial analytical model, model updating techniques have been developed to investigate the accuracy and validity of the created analytical models. Modifying or reassessing unknown structural system features that are utilized as parameters in numerical modeling is the basic goal of the model updating technique. Comprehensive information regarding the general and local behavior of the structure can be found in the vibration experiment data (frequency response functions, acceleration-time values, natural frequencies and natural mode shapes, curvature degrees, modal stresses, and modal flexibility). Therefore, these vibration data play an important role in estimating uncertain system

parameters in the FE model updating process. In addition, the presence and location of damage in the structure can be determined by using the parameters obtained from modal analysis techniques that can be applied to structures. This method is predicated on the idea that damage to the structure alters its dynamic properties by affecting its overall behavior, including its mass, stiffness, and damping (Ramos et al., 2010; Dawari and Vesmawala, 2013; Bassoli et al, 2018).

In recent years, studies on creating FE models have begun to increase rapidly in various structures, taking into account the uncertainties mentioned above (Astroza et al., 2020; Xin et al., 2020; Altunişik et al., 2020). Recent studies have shown that the results obtained from the FE model created when uncertainties are taken into account are more reliable (Oberkampf, 2010), which shows the necessity and importance of examining uncertainties at the modeling stage (Simoen et al., 2015). When examining uncertain parameters in FE model update studies, the parameters that are considered to be updated are no longer deterministic but are defined as random variables. The main probabilistic and non-probabilistic methods applied to determine random variables are presented in Table 3.

Although statistical methods such as the Monte Carlo method (Fishman, 2014) seem to be a simple method for evaluating the behavior of a model with uncertain parameters, they may be disadvantageous because the convergence process takes time. Sampling methods and variant reduction techniques can help overcome this problem.

Table 3. Main Parametric Methods Used to Determine Uncertain Parameters

Probabilistic Methods	Non-Probabilistic Methods
Statistical Methods Monte Carlo Method Variable Reduction and Sampling Method Reliability Method Response Surface Method	Generalized Information Method Frequency Theorem
Stochastic FE Methods Confusion, Neumann Decomposition Spectral Stochastic Method	Fuzzy Set Theory Frequency Theorem
Model Reduction Techniques Proper Orthogonal Decomposition Proper Orthogonal Decomposition	Information Gap Decision Theory

Source: (Daouk Et Al, 2015)

The Stochastic FE method is based on the combination of finite elements with probabilities. Major random variables are addressed using the perturbation method (Kleiber and Hien, 1994) and Spectral Stochastic Methods (Ghanem and Spanos, 2013). Model reduction techniques aim to approximate the behavior of a complex model, a representative model built through a prediction on a reduced basis, such as Proper Orthogonal Decomposition (Willcox and Peraire, 2002) and Proper Generalized Decomposition (Chinesta et al, 2011). However, some situations may be epistemic due to uncertainties and incomplete information. For this reason, non-probabilistic approaches have been developed, such as the frequency theorem, which is applied by taking into account the limit ranges of variable output parameters, and the Fuzzy Set Method, which does not use invariant calculations (Massa et al., 2008; Quaranta, 2011).

Recently, the Response Surface Method (RSM) has gained an important place among the techniques developed to characterize and measure the difference between numerical models and real structures, taking into account different sources

and types of uncertain parameters. The most important advantage of RSM can be defined as providing rapid optimization due to its simple and flat rate of change thus reducing the convergence problem. Used in both FE model updating and damage assessment studies, RSM represents the link between the inputs and outputs of a physical system with a certain purpose by combining statistical and mathematical methods. To create a mathematical model that can represent such relationships, several subsets must be selected in the entire design area. To obtain a reliable model, experimental design techniques can be used to provide specific designs consisting of a limited number of points with a reasonable distribution from the entire design space. The model updating approach based on RSM has been applied to civil engineering structures (Deshan et al., 2015; Beheshti et al. 2019; Xiong et al. 2022).

REFERENCES

Altunişik, A. C., Kalkan, E., Okur, F. Y., Karahasan, O. Ş., Ozgan, K. 2020. "Finite-Element Model Updating and Dynamic Responses of Reconstructed Historical Timber Bridges using Ambient Vibration Test Results", Journal of Performance of Constructed Facilities, 34, 04019085.

Amaddeo, C., & Dorn, M. (2023). Ambient Vibration Tests and Modal Analysis of a Six-story Lightweight Timber Frame Building. In World Conference on Timber Engineering (WCTE 2023), Oslo (pp. 2898-2906).

Astroza, R., Alessandri, A., Conte, J. P. 2020. "Finite Element Model Updating Accounting for Modeling Uncertainty", Model Validation and Uncertainty Quantification, 3, 211-221. Cambridge University Press.

Baptista, M. A., Mendes, P., Oliveira, S. 2005. "Use of ambient vibration tests for structural identification: 3 case studies", Proceedings of the 1st International Operational Modal Analysis Conference, 26-27 April, Curran Associates, 85-93, Copenhagen, Denmark.

Bassoli, E., Vincenzi, L., D'Altri, A. M., Miranda, M., Forghieri, M., Castellazzi, G. 2018. "Ambient vibration-based finite element model updating of an earthquake-damaged masonry tower", Structural Control Health Monitoring, 25, 1-15.

Beheshti Nezhad, H., Miri, M., and Ghasemi, M. R. (2019). New neural network-based response surface method for reliability analysis of structures. Neural Computing and Applications, 31, 777-791.

Betti, M., Galano, L. 2012. "Seismic Analysis of Historic Masonry Buildings: The Vicarious Palace in Pescia (Italy)", Buildings, 2, 63-82.

Brincker, R., Zhang, L., Andersen, P. 2000. "Modal identification from ambient responses using frequency domain decomposition", Proceedings of the 18th Society of Experimental Mechanics International Modal Analysis Conference, 7-10 February, Society for Experimental Mechanics, Inc. San Antonio, USA.

Chen, G. W., Omenzetter, P., and Beskhyroun, S. (2017). Operational modal analysis of an eleven-span concrete bridge subjected to weak ambient excitations. Engineering Structures, 151, 839-860.

Chinesta, F., Ladevèze, P., Cueto, E., 2011. "A short review on model order reduction based on proper generalized decomposition", Archives of Computational Methods in Engineering, 18, 395-404.

Daouk, S., Louf, F., Dorival, O., Champaney, L., Audebert, S. 2015. "Uncertainties in structural dynamics: overview and comparative analysis of methods", Mechanics and Industry, 16, 404:1-10

Dawari, V., Vesmawala, G. 2013. "Identification of crack damage in reinforced concrete beams using mode shape-based methods", Civil and Environmental Research, 3, 24-29.

Deshan, S., Qiao, L., Inamullah, K., Xiaohang, Z. 2015. "A novel finite element model updating method based on substructure and response surface model", Engineering Structures, 103, 147-156.

Fishman, G. S. 2014. Monte Carlo: Concepts, Algorithms and Applications (4. Basım). Springer-Verlag.

Ghanem, R. G., Spanos, P. D. 2013. Stochastic Finite Elements: A Spectral Approach (6. Basım). Courier Corporation.

Hasani, H., and Freddi, F. (2023). Operational Modal Analysis on Bridges: A Comprehensive Review. Infrastructures, 8(12), 172.

Ibsen, L. B., Liingaard, M. 2005. "Output-only modal analysis used on new foundation concept for offshore wind turbine", Proceedings of the 1st International Operational Modal Analysis Conference, 26-27 April, Curran Associates, 385-393, Copenhagen, Denmark.

Kleiber, M., T. D. Hien, T. D. 1994. The stochastic finite element method: basic perturbation technique and computer implementation (1. Basım). John Wiley & Sons, England.

Maetz, T., Kappel, J., Wiemann, M., Bergmannshoff, D., Hägelen, M., Jetten, R., ... and Krozer, V. (2023). Microwave Structural Health Monitoring of the Grouted Connection of a Monopile-Based Offshore Wind Turbine:

Fatigue Testing Using a Scaled Laboratory Demonstrator. Structural Control and Health Monitoring, 2023.

Massa, F., Ruffin, K., Tison, T., Lallemand, B. 2008. "A complete method for efficient fuzzy modal analysis", Journal of Sound and Vibration, 309, 63-85.

Oberkampf W. L., Roy C. J. 2010. Verification and validation in scientific computing (3. Basım). Cambridge: Cambridge University Press.

Quaranta, G. 2011. "Finite element analysis with uncertain probabilities", Computer Methods in Applied Mechanics and Engineering, 200, 114-129.

Raineri, C., Fabbrocino, G. 2014. Operational Modal Analysis of Civil Engineering Structures, Springer, New York.

Rainieri, C., Notarangelo, M. A., and Fabbrocino, G. (2020). Experiences of dynamic identification and monitoring of bridges in serviceability conditions and after hazardous events. Infrastructures, 5(10), 86.

Ramos, L. F., Roeck, G. D., Lourenço, P. B., Campos-Costa A. 2010. "Damage identification on arched masonry structures using ambient and random impact vibrations", Engineering Structures, 32, 146-162.

Ramos, L. F., Roeck, G. D., Lourenço, P. B., Campos-Costa A. 2010. "Damage identification on arched masonry structures using ambient and random impact vibrations", Engineering Structures, 32, 146-162.

Reynolds, P., Mohanty, P., Pavic, A. 2005. "Use of Operational Modal Analysis on empty and occupied stadia structures", Proceedings of the 1st International Operational Modal Analysis Conference, 26-27 April, Curran Associates, 75-85, Copenhagen, Denmark.

Shim, H. B., & Park, H. S. (2023). SSI-LSTM network for adaptive operational modal analysis of building structures. Mechanical Systems and Signal Processing, 195, 110306.

Simoen E., De Roeck G., Lombaert G. 2015. "Dealing with uncertainty in model updating for damage assessment: a review", Mechanical System and Signal Processing. 56, 123-149.

Türker T. 2011. Çevresel Titreşim Verileri Kullanılarak Yapıların Hasar Durumlarının Tespiti ve Değerlendirilmesi, Doktora Tezi, Karadeniz Teknik Üniversitesi, Fen Bilimleri Enstitüsü, İnşaat Mühendisliği Anabilim Dalı.

Ural, A., Celik, T. 2018. "Dynamic Analyses and Seismic Behavior of Masonry Minarets with single Balcony", Aksaray University Journal of Science and Engineering, 2, 13-27.

Van Overschee, P., and De Moor, B. (2012). Subspace identification for linear systems: Theory-Implementation—Applications. Springer Science & Business Media.

Willcox, K., Peraire, J. 2002. "Balanced model reduction via the proper orthogonal decomposition", AIAA Journal, 4, 2323-2330.

Xin, L., Li, X., Zhu, Y., Liu, M. 2020. "Uncertainty and sensitivity analysis for train-ballasted track–bridge system", Vehicle System Dynamics, 58, 453-471.

Xiong, C. Q., Zhu, Z. W., and Jiang, J. (2022). Response Surface-Based Finite Element Model Updating of Steel Box-Girder Bridges with Concrete Composite Decks. Advances in Civil Engineering, 2022.

MIXTURE DISTRIBUTIONS AND USE OF IN ENGINEERING

Selin SARAÇ GÜLERYÜZ[1]

1. INTRODUCTION

In the service sector, the accuracy of companies' forecasts within the competitive environment increases their chances of survival. Therefore, demand forecasting holds high importance for the profitability and continuity of a firm (Ergün & Şahin, 2017). There are numerous methods used in demand forecasting that assist in making strategic and operational decisions. All operations in service and production enterprises depend on the quantity of demand. Accurate short, medium, or long-term demand forecasting ensures precise planning for machinery, personnel, and capacity.

In demand forecasting, both non-numerical methods, relying on the forecaster's knowledge and experience, and numerical analyses based on time series are conducted (Çağıl, 1997). Regardless of the accuracy of the demand forecasting methods employed, the results will not be 100% accurate. Therefore, choosing an incorrect forecasting method will further increase the margin of error.

The process of demand forecasting comprises five stages. Firstly, factors influencing demand are identified. For instance, for a bank, the influencing factor may be customer arrivals, whereas for a factory, it may be the quantity of ordered products, or for a restaurant, the number of prepared meals. These identified

[1] Asst. Prof., Toros University, Faculty of Engineering, Department of Industrial Engineering, selin.sarac@toros.edu.tr, ORCID: 0000-0002-4729-0637.

factors are collected in the second stage and prepared for analysis. In the third stage, the period length for the collected data is determined. The fourth stage involves selecting the forecasting method, and finally, in the fifth stage, the validity of the obtained results is tested.

Forecasting methods can be categorized into three groups: qualitative, quantitative, and artificial intelligence-based. Qualitative methods, relying on individual opinions and experience, do not adhere to a scientific approach. In quantitative methods, historical data is mathematically utilized to predict future data (Viglione, 2007). Artificial intelligence-based methods rely on inferences drawn from previously acquired information for decision-making and forecasting (Borgelt & Kruse, 2002).

Mathematical modeling of systems, queue theory, and simulation modeling are widely used for planning. The key is to define the correct parameters for the system to provide the most accurate results. If simulation modeling is to be used for a hospital system, parameters such as the inter-arrival time of patients or the number of patients arriving within a specific period and service times are required.

Count data can vary from the number of products customers purchase in a store to the number of patients arriving at a hospital or the calls received at a center. In systems where such uncertainty exists, it is essential to predict relevant parameters for planning, such as capacity, personnel, and product quantities, using methods like demand forecasting, qualitative, quantitative, and artificial intelligence-based approaches. Particularly in systems where uncertainty is high, the effective application of one of these methods is crucial for the proper management of the system. These methods involve checking whether data taken over a specific time period conforms to a

known theoretical distribution. To use input parameters in such models, these parameters need to be predicted in a form close to reality. In simulation models, these predictions are often made using methods such as time series analysis, machine learning, and theoretical distribution fitting.

The method of fitting to a theoretical distribution, one of the most commonly used approaches for determining simulation parameters, may not work well in some cases. For instance, certain data may vary according to specific factors, increasing the variance of the data. As the system becomes more complex, fitting data to a known pure distribution becomes more challenging. In such cases, attempts are made to represent the system with an empirical distribution. Applying an empirical distribution, especially in cases where there is a large amount of data or where the data is concentrated within a specific range, becomes a laborious process. Demand forecasting and statistical distribution fitting methods work effectively in situations where uncertainty and variance are low, but fitting data to any pure distribution becomes challenging when uncertainty is high. In cases where data does not conform to any known pure distribution, it becomes necessary to represent it by creating an empirical distribution. Creating an empirical distribution is a time-consuming and labor-intensive process, especially when dealing with a large amount of data. At this point, the concept of representing data as a mixture distribution by dividing it into multiple sub-populations has emerged. Mixture distribution models are used to understand the heterogeneity in a specific dataset and identify subgroups arising from this heterogeneity. These models can be described as powerful tools in statistical analyses and data mining applications, particularly for extracting information from large and complex datasets.

2. MIXTURE DISTRIBUTIONS

A mixture distribution can be thought of as a combination of convex distribution functions that can be applied to model two or more states (Lindsay, Titterington, Smith, & Makov, 1987). In a simpler definition, distributions consisting of two or more components are defined as mixture distributions (Dedeoğlu, 2020).

Mixture distribution models provide a mathematical approach to statistically model measurement values of random features in natural phenomena and use in the many areas such as biology, chemistry, engineering, genetics, medicine, physics, criminology, psychology, education, economics, marketing and health (Koyuncu, 2019).

Mixture distribution models are also known as classification methods and include statistical techniques such as cluster analysis, discriminant analysis and image processing (Ng, Xiang, & Yau, 2019). Mixture distributions are used to model more complex data using a weighted combination of different component distributions. These distributions are often used to better describe complex real-life events and data. For this reason, mixture distribution models have an important place in theoretical and practical applications and their use is increasing. Mixture distributions can be identified as a good tool for representing time series models and can be used directly for short- to medium-term forecasting (Eirola & Lendasse, 2013).

Mixture distribution modeling essentially involves describing the group structure of the population under study and provides a flexible and powerful probability approach in major statistical fields, such as cluster analysis In the context of cluster analysis applications, the grouping of entities into several clusters is achieved through mixture distribution. Thus, the objective is to obtain data groups with the least similarity between clusters and

the highest similarity within the cluster. Mixture distribution-based clustering approaches measure observed trait data based on variables associated with each entity, without prior knowledge of the group structure of the underlying population. This situation is referred to as unsupervised classification. Mixture models not only provide a robust mathematical framework for clustering but also offer statistical inferences for determining the number of components and assessing classification uncertainty (McLachlan & Peel, 2000).

Applied statistics often assumes that observed data are collected in a single population. However, this assumption of homogeneity is frequently unrealistic or insufficient to accurately represent the data under study. At this point, mixture distribution models play a crucial role in representing the data, offering an approach that takes into account the existence of heterogeneous subpopulations with different parameters. Cost-effectiveness analyses, which tend to work with smaller datasets, may find the scope of parametric modeling more limited (Mills & Patterson, 2009). Recently, nonlinear methods, such as posterior mixture distributions and semiparametric approaches, have started to be used instead of linear regression (Jones, 2010).

The probability density function of mixture distributions is expressed as the weighted sum of the probability density functions of distributions. The probability density function attempts to model the distribution of the data set by taking into account the interaction and weights of different components.

A finite mixture distribution can be thought of as a combination of convex distribution functions that can be applied to model two or more states (Titterington et al., 1985). In a simpler definition, distributions consisting of two or more components are defined as mixture distributions.

Mixture distribution models were proposed by Pearson and have been used for many years in various fields such as genetics, biology, agriculture, and engineering. Mixture distributions consist of two or more components, defined by three elements: the mixing ratio $(\pi_1, \pi_2, \dots, \pi_k)$, the number of components (k), and the distribution parameters $f_1(x;\ \theta_1), f_2(x;\ \theta_2), \dots, f_k(x;\ \theta_k)$.

$$f(x) = \pi_1 f_1(x;\theta_1) + \pi_2 f_2(x;\theta_2) + \cdots + \pi_k f_k(x;\theta_k) \quad (1)$$

$$0 \le \pi_i \le 1\ i = 1,2, \dots, k \quad (2)$$

$$\sum_{i=1}^{k} \pi_i = 1 \quad (3)$$

In the general representation of mixture distributions, the symbol ψ can be used for parameters.

$$f(x,\psi) = \sum_{i=1}^{k} \pi_i f(x;\theta_i) \quad (4)$$

The most important problem encountered when deal with a mixture distribution model is determining whether the data set consists of a mixture of more than one distribution and determining these distributions (Atienza, García-Heras, Muñoz, & Villa, 2007). The problem of identifying components leads to the problem of estimating distribution parameters. Estimating the number of components of a mixture distribution is a challenging process that has not yet been completely solved (McLachlan and Peel, 2000). The uncertainty in this regard can be resolved by applying some parametric assumptions and stacking analysis.

For a data set to be modeled as a mixture distribution, the first step is to estimate the number of components. Once the number of components is determined, the mixture distribution can be divided into homogeneous distributions. In the second stage, mixing ratios are estimated, and finally, distribution parameters are determined. The primary objective in determining the number of components is to cluster the data in a way that minimizes the distance between points within formed clusters and maximizes

the distance between points in different clusters (Arabie, Hubert, & De Soete, 1996). There are multiple methods suggested in the literature to determine the number of components, commonly utilized tools include histograms, Q-Q plots, likelihood test rate (LTR), Akaike Information Criteria (AIC), and Bayesian Information Criteria (BIC) (Schlattmann, 2003).

2.1. Estimating the Number of Components of Mixture Distribution

Technically, determining the number of components (k) of mixture distributions is a technique used for a clustering algorithm. The main challenge of deal with a mixture distributions lies in discovering hidden patterns and structures in the dataset.

2.1.1. Graphical Methods

Graphical methods can be initially employed for estimating the number of components.

Probability density functions (PDF) can be used as a first step to determine the number of component of mixture distribution. A single-peaked distribution in the data set is a representation of a homogeneous structure that does not show any clustering, while an PDF with multiple peak can describe a heterogeneous data set.

Figure 1. Probability density function of $\mathbf{0.5f_1(10,2) + 0.5f_2(20,3)}$

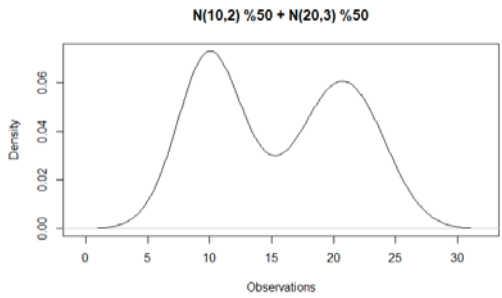

In Figure 1, probability density function of mixture of two normal distributions is given. The probability density function has two peaks. The presence of two peak indicates the existence of a mixture distribution. The initial number of components can be considered as two.

Figure 2. Probability density function of $0.5f_1(10,2) + 0.5f_2(12,3)$

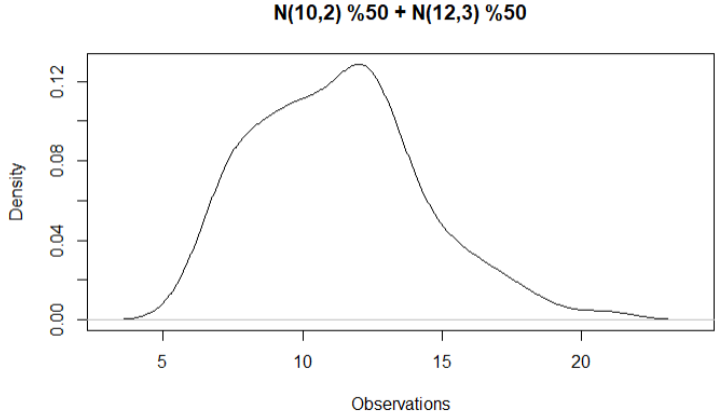

In Figure 2, on the other hand, there is no probability density function that conforms to any known pure distribution. It may be considered as a mixture distribution, but determining the number of components is challenging.

Figure 3. Probability density function of $0.2f_1(6,2) + 0.3f_2(10,2) + + 0.5f_3(20,2)$

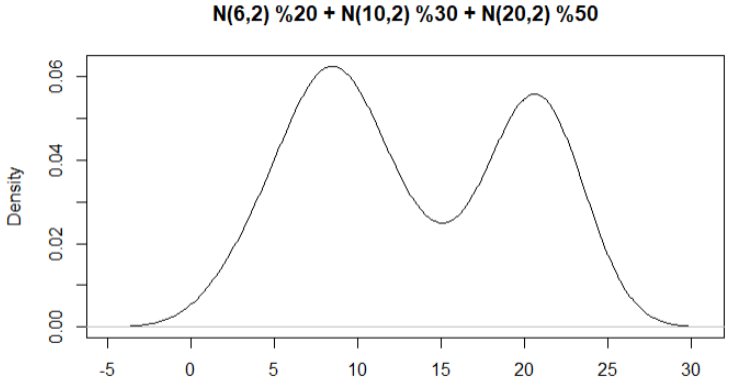

In Figure 3, a two-component interpretation can be made for the mixture distribution. However, the mixture distribution is generated from three components, and due to the overlapping of the N(6, 2) and N(10, 2) distribution values, it behaves as a pure distribution. This result indicates that the effectiveness of this probability density function approach to estimated number of components of mixture distribution is limited.

Q-Q plot can be helpful in determining whether a dataset follows a mixture distribution. A Q-Q plot is a graphical representation of the quantiles of the dataset, comparing the distribution quantiles of the dataset against those expected for a chosen distribution by dividing the cases into equally sized groups. If the variable under consideration conforms to the test distribution, the points on the Q-Q plot cluster around the line formed by the expected variables (Pallant, 2005).

By examining the probability density function and Q-Q plot, it can be determined whether the data set follows a mixture distribution, and so, an initial number of components can be identified.

Oscillations in the Q-Q graph can be shown as evidence that the data set contains more than one component. Since this method is a graphical method, it is not always sufficient to determine the number of components.

As seen in Figure 4, the Q-Q plot of data consisting of a pure distribution lies on the line formed by the theoretical variables.

Figure 4. Q-Q plot of $\mathbf{N(10,2)}$

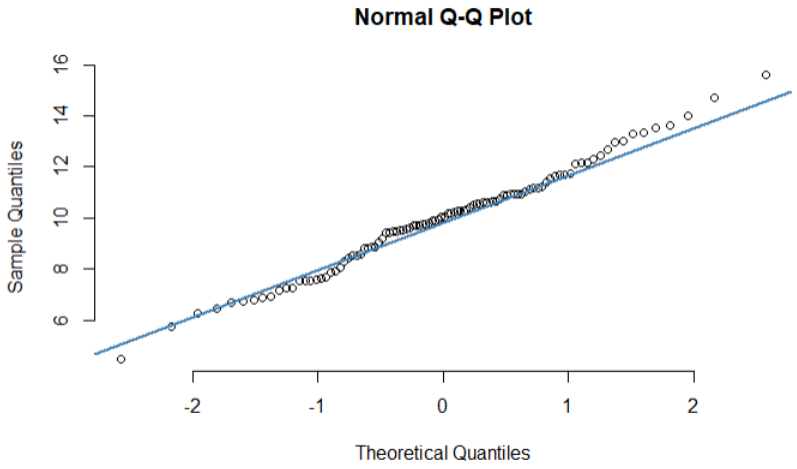

However, as can be seen in Figure 5, the oscillations observed in the Q-Q plot can be considered as evidence that the dataset includes multiple components.

Figure 5. Q-Q plot of $\mathbf{0.5f_1(10,2) + 0.5f_2(20,3)}$

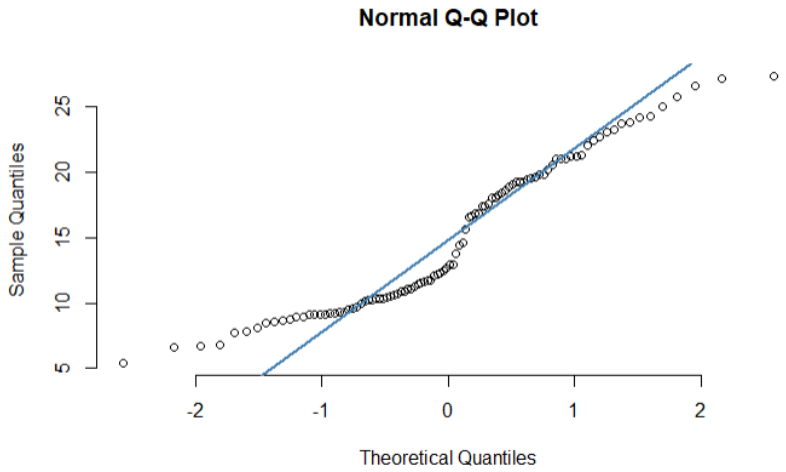

In Figure 6, due to the data consisting of a mixture distribution, oscillations are observed. These methods allow for interpretations

regarding the existence of a mixture distribution but do not provide precise information about the number of components.

Figure 6. Q-Q plot of $0.2f_1(6,2) + 0.3f_2(10,2) + + 0.5f_3(20,2)$

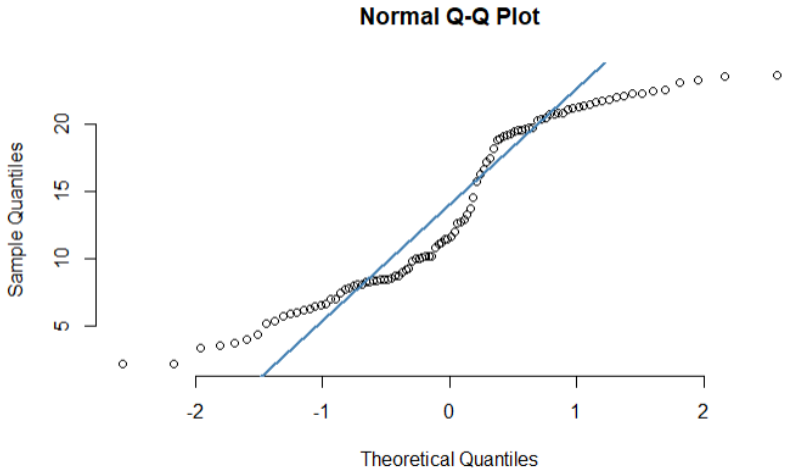

2.1.2. Model-Based Methods

Model-based methods such as likelihood test rate (LTR), Akaike Information Criteria (AIC), and Bayesian Information Criteria (BIC) should be integratively employed to determine the number of components in mixture distributions.

One of the methods used to estimate the number of components k of mixture distribution models is the likelihood test rate (LTR). The aim of LTR is to determine whether the difference between mixture distributions is statistically significant. So, it can be used as a criterion to determine which model fits the dataset better. LTR is calculated as $LTR = 2(lnL_1 - lnL_2)$, where L_1 is a simple and L_2 is a likelihood function for the complex model.

AIC and BIC are also widely used to select optimal k (Sin & White, 1996). AIC estimates the best model to represent a data set by comparing it with other models. AIC is calculated as $AIC =$

$2k - 2lnL(\psi)$ for a mixture distribution with k components, where $L(\psi)$ is the maximum value of the likelihood function (Akaike, 1974). When comparing AIC values for different k values, the model with the lowest is selected.

BIC is calculated as $BIC = -\ln(n)\, k - 2lnL(\psi)$ where n is the number of observations (Schwarz, 1978). Similar to the AIC, the model with the smallest value is chosen.

In general, AIC tends to perform better for large datasets, whereas BIC yields more accurate results for small datasets (Schwarz, 1978).

2.2.Estimating the Parameters of Mixture Distribution

After determining the mixture distribution with k components based on histograms, Q-Q plots, AIC, and BIC values, the next step involves estimating the parameters for each component according to the k number of components. The most commonly used methods for parameter estimation are Maximum Likelihood Estimation (MLE) and the Expectation-Maximization (EM) algorithm.

2.2.1. Maximum-Likelihood Estimation (MLE)

The MLE is a statistical method used to estimate the parameters of a model and was introduced by Fisher (Fisher, 1922). It is based on the principle of finding parameter values that maximize the likelihood function of the observed data, which is a function of the model parameters.

The maximum likelihood estimation method operates as an algorithm that seeks to find the parameter values of a dataset that maximize the probability of observed sample values.

The maximum likelihood estimate for θ is the set of values $\theta(x_1, \dots, x_n)$ that maximizes the likelihood function $L(\psi)$ for a k-component mixture distribution model formed by n observations.

To simplify the mathematical operations, the logarithmic likelihood function is often employed. Subsequently, optimization problems are solved by taking derivatives with respect to each parameter.

2.2.2. Expectation-Maximization (EM) Algorithm

The EM algorithm was introduced by Dempster in 1977 (Dempster, Laird, & Rubin, 1977). This algorithm has been extensively used in estimating parameters for mixture distribution models (Lakshmi & Vaidyanathan, 2016).

The EM algorithm works iteratively to compute maximum likelihood estimates for parameters and mixture proportions based on a specified initial value for parameters. Each observation is assigned to a cluster with a certain probability distribution weight, and there are no strict boundaries between these created clusters. New means are calculated based on these weighted measurements. When the algorithm is completed, it determines to which cluster each observation in the dataset belongs.

3. RESULTS

Skewed data modeling is a common situation in statistical analysis. When a data set is not suitable for pure distribution and has an asymmetric structure, the modeling process becomes difficult. Mixture distributions are an effective tool in modeling non-symmetric distributions. Also applied statistics is mostly based on the assumption that observed data are collected in a single pure population. This assumption of homogeneity is often not realistic or sufficient to accurately represent the data under study. At this point, mixture distribution plays an important role in statistical data modeling.

In simulation of engineering proceses, input parameters such as customer inter-arrival times and service times are often

represented through statistical fitting methods. If the data does not fit a pure distribution, an empirical distribution is generally used. However, empirical distributions do not perform well for data with very few or very many observations or for data clustered within a specific range. Moreover, since empirical distributions always produce the same value, this method has its disadvantages. Especially in complex and challenging datasets, data can be effectively represented by dividing it into two or more homogeneous structures using the mixture distribution method instead of relying on an empirical distribution.

For future decision-making, demand predictions need to be modeled to best reflect the reality of the data taken from the past. Therefore, compared to the empirical distribution, the mixture distribution may work more reliably due to its ability to represent a wide range of data, including replication, iteration, and narrow and broad intervals.

KAYNAKÇA

Akaike, H. (1974). A new look at the statistical model identification. *IEEE Transactions on Automatic Control*, *19*(6),716–723. https://doi.org/10.1109/tac.1974.1100705

Arabie, P., Hubert, L., & De Soete, G. (1996). Clustering and classification. In *WORLD SCIENTIFIC eBooks*. https://doi.org/10.1142/1930

Atienza, N., García-Heras, J., Muñoz, J. M., & Villa, R. (2007). An application of mixture distributions in modelization of length of hospital stay. *Statistics in Medicine*, *27*(9), 1403–1420. https://doi.org/10.1002/sim.3029

Borgelt, C., & Kruse, R. (2002). *Graphical Models: methods for data analysis and mining*. Retrieved from http://ci.nii.ac.jp/ncid/BA55975025

Çağıl, G. (2017). Mevsimlik olmayan Box-Jenkins modellerinde iki aşamalı yapay sinir ağlarının kullanılması. *Academic platform-Journal of Engineering and Science*, 119–126. https://doi.org/10.21541/apjes.335424.

Dedeoğlu, M. (2020). Estimation of critical nitrogen contents in peach orchards using visible-near infrared spectral mixture analysis. *Journal of Near Infrared Spectroscopy, 28*(5–6), 315–327. https://doi.org/10.1177/0967033520939319

Dempster, A. P., Laird, N. M., & Rubin, D. B. (1977). Maximum Likelihood from Incomplete Data via the EM Algorithm. *Journal of the Royal Statistical Society. Series B (Methodological)*, *39*(1), 1–38. http://www.jstor.org/stable/2984875

Eirola, E., & Lendasse, A. (2013). Gaussian mixture models for time series modelling, forecasting, and interpolation. In *Lecture Notes in Computer Science* (pp. 162–173). https://doi.org/10.1007/978-3-642-41398-8_15

Ergün, S., & Şahin, S. (2017). Literature survey about demand forecasting in industry. *Ulakbilge Sosyal Bilimler Dergisi, 5*(10), 469–487. https://doi.org/10.7816/ulakbilge-05-10-11

Fisher, R. A. (1992). On the Mathematical Foundations of Theoretical Statistics. In *Springer series in statistics* (pp. 11–44). https://doi.org/10.1007/978-1-4612-0919-5_2

Koyuncu, M. (2019). Sağlık sistemlerinde karma dağılım modellerinin uygulanması. *Çukurova Üniversitesi Mühendislik Mimarlık Fakültesi Dergisi*, *34*(3), 73–84. https://doi.org/10.21605/cukurovaummfd.637621

Jones, A.M. (2010). Models For Health Care, Health, Econometrics and Data Group (HEDG) Working Papers

10/01, HEDG, c/o Department of Economics, University of York.

Lakshmi, R., & Vaidyanathan, V. S. (2016). Parameter Estimation in Gamma Mixture Model using Normal based Approximation. *Journal of Statistical Theory and Applications*, *15*(1), 25. https://doi.org/10.2991/jsta.2016.15.1.3

Lindsay, B. G., Titterington, D. M., Smith, A. F. M., & Makov, U. (1987). Statistical analysis of finite mixture distributions. *Journal of the American Statistical Association*, *82*(398), 694. https://doi.org/10.2307/2289504

Ng, S. K., Xiang, L., & Yau, K. K. W. (2019). Mixture modelling for medical and health sciences. *Chapman and Hall/CRC eBooks*. https://doi.org/10.1201/9780429195181

McLachlan, G. J., & Peel, D. (2000). Finite mixture models. *Wiley series in probability and statistics*. https://doi.org/10.1002/0471721182

Mills, T. C., & Patterson, K. (2009). Palgrave Handbook of Econometrics. *Palgrave Macmillan UK eBooks*. https://doi.org/10.1057/9780230244405

Pallant, J. (2020). *SPSS Survival Manual: A Step by Step Guide to Data Analysis using IBM SPSS*. McGraw-Hill Education (UK).

Schlattmann, P. (2003). Estimating the number of components in a finite mixture model: the special case of homogeneity. *Computational Statistics & Data Analysis*, 41(3–4), 441–451. https://doi.org/10.1016/s0167-9473(02)00173-1

Schwarz, G. (1978). Estimating the Dimension of a Model. *The Annals of Statistics*, *6*(2), 461–464. http://www.jstor.org/stable/2958889

Sin, C., & White, H. (1996). Information criteria for selecting possibly misspecified parametric models. *Journal of Econometrics*, *71*(1–2), 207–225. https://doi.org/10.1016/0304-4076(94)01701-8

Viglione, A., Laio, F., & Claps, P. (2007). A comparison of homogeneity tests for regional frequency analysis. *Water Resources Research*, *43*(3). https://doi.org/10.1029/2006wr005095

INVESTIGATION OF THE PERFORMANCE OF DIFFERENT MAXIMUM POWER POINT TRACKING ARCHITECTURES IN BUILDING INTEGRATED PHOTOVOLTAICS FOR SHADING CONDITIONS

Tuğba DURMUŞ[1]

Mustafa Engin BAŞOĞLU[2]

1. INTRODUCTION

With the increase in the world population, the demand for energy has also increased. The amount of energy consumption and the diversity in energy resources provide information about the economic and social development level of countries. The majority of electrical energy demand is provided by the use of limited fossil resources. Interest in renewable energy sources has increased due to the unplanned use of fossil resources, their limitations and environmental pollution [1]. It is possible to easily access solar energy, which is a renewable energy source, for electricity generation.

Solar energy-based electricity generation with the use of photovoltaic (PV) cells in the building envelope was examined in terms of design, and examples of integrating PV modules into buildings abroad were included. As a result of the study, it was seen that the use of PV panels in the roof area of the building is

[1] Electrical and Electronics Engineer, (Gümüşhane University, Institute of Science and Technology), tdurmus4263@gmail.com, ORCID: 0000-0002-8723-0137.

[2] Assoc. Prof., (Gümüşhane University, Faculty of Engineering and Natural Sciences, Electrical and Electronics Engineering,) menginbasoglu@gumushane.edu.tr, ORCID: 0000-0002-6228-4112.

widespread [2]. A monitoring system that measures PV system performance, PV module temperatures and solar radiation amounts statically placed on an urban building is described. It has been determined that the amount of energy production is highest at the beginning of spring and autumn seasons, less in winter than in these two seasons, and lowest in summer [3]. In another study, the electricity production performance of the building-integrated PV (BIPV) system on various surfaces of a building in Elazığ was examined. Single crystal and polycrystalline PV cells were used in the Vsyst 6.2.6 program for analysis. Under conditions where there is no shading, higher electrical energy was produced in panels of single-crystal PV cell technology compared to polycrystalline cell technology [4].

In order to obtain maximum power from PV modules, a boost converter with Perturbe-Observe (P&O) algorithm was used. Maximum power point tracking (MPPT) performance under different irradiances was examined using the proposed boost converter [5]. In a different study, P&O and incremental conductance (IC) algorithms in different radiation and load situations were examined using a boost converter. Under these conditions, it has been determined that the times to reach the maximum power point (MPP) are close to each other, but the oscillations in the P&O algorithm are more than the other algorithm. While the performances of both algorithms are close to each other at high irradiance values, it has been stated that the P&O algorithm has difficulty in monitoring MPP at low irradiance. In addition, the P&O algorithm was more successful under changing load conditions [6]. In order for the PV modules to reach the MPP and operate by constantly monitoring the MPP, MPPT algorithms such as P&O, IC, hybrid IC, fuzzy logic, artificial neural networks and adaptive network-based fuzzy inference system have been analyzed in cuk and boost converter.

It was concluded that load resistance of the boost converter should be greater than the internal resistance of the PV module [7].

Within the scope of the study, the energy production performance of different MPPT architectures under different radiation conditions in the BIPV system was examined. Models of PV modules and boost converter were designed in MATLAB/SIMULINK and MPPT was realized with the P&O algorithm. MPPT architectures can be listed as central, module-based and sub-module-based MPPT. The different radiation conditions to which PV modules are exposed are defined as three different scenarios: standard conditions, light and severe shading. Irradiance values for light and heavy shading were determined randomly. Three different radiation scenarios were run for each MPPT architecture and the results were analyzed.

2. MODELING AND SIMULATION STUDIES

The roof area of the building was preferred for the use of the BIPV design. The color template visualizing the appearance of the PV panels integrated on the roof and the amount of radiation they are exposed to is shared in Figure 1.

Figure 1. Example of a roof-integrated PV system and the color template used for different irradiances in PV modules

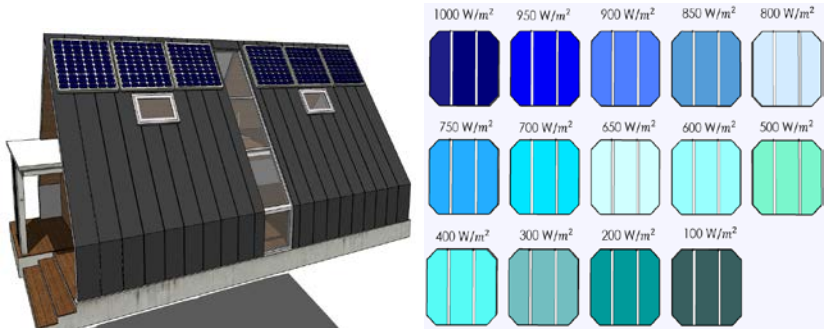

MATLAB/SIMULINK was used to simulate scenarios in which PV panels integrated on the building roof are exposed to various radiations. In the simulations, central MPPT, module-based MPPT and sub-module-based MPPT architectures were examined and the results were compared. Three radiation profiles are defined in each MPPT architecture: Scenario-1, Scenario-2 and Scenario-3. In Scenario-1, all modules are exposed to equal radiation of 1000W/m^2, in Scenario-2, mild partial shading is considered, and in Scenario-3, severe partial shading is considered.

2.1. Central MPPT Architecture

In MATLAB/SIMULINK, after connecting the PV modules to each other in series for the central MPPT architecture, a boost converter was connected to their outputs and MPPT was realized with the P&O algorithm. In the central MPPT, six PV modules are used and these modules are connected in series. The technical specifications of components such as PV module, boost converter and P&O algorithm in this architecture are listed in Table 1. The power of the serially connected PV modules in MPP is 1500W, its voltage is 181.86V and its current is 8.25A.

In case of mild partial shading, the number of MPPs in the P-V curve varies between two and in case of severe partial shading, it varies between four and six. In the tables where the radiation amounts for these scenarios are shared, the areas colored green indicate that the global MPP has been reached, and the areas colored red indicate that the local MPP is stuck. In some of the tables, green or red colors are not used in the areas where the power value in MPP is located. In this case, both the global MPP and the local MPP could not be reached.

2.1.1. Scenario-1: Regular Radiation Condition

In Scenario-1 simulation, irradiance values in module 1, module 2, module 3, module 4, module 5 and module 6 are

1000W/m^2. During the simulation period, 1000W/m^2 radiation was applied to the PV modules and the power value at the peak was 1500.43W. When the data obtained as a result of the simulation was examined, it was determined that the PV system reached the targeted power and voltage values.

Simulation results are presented in Figure 2, and Figure 2.(b) shows that the PV system produces 1500W power. Since the radiation coming to the PV modules is constant, there is no partial shadowing and there is only one MPP in the P-V curve. In the central MPPT architecture, the MPPT efficiency for Scenario-1 is calculated as 96.45%.

Table 1. Features of components in the central MPPT

Characteristic features in central architecture					
Bosch solar energy c-Si M60 NA42117 250W - 6 connected in series		Values of the P&O algorithm		Values of the boost DC-DC converter	
Power at MPP (W)	1500,34	D_{MAX}	0.95	C_{INPUT} (F)	1500 µ
Voltage at MPP (V)	181,86	$D_{MİN}$	0.1	C_{OUTPUT} (F)	500 µ
Current at MPP (A)	8,25	D_{inut}	0.5	Inductors (H)	2.5 m
Open circuit voltage value (V)	227,4	ΔD	0.005	Resistance (Ω)	150
Short circuit current (A)	8,82	Frequency (kHz)	40		

Figure 2. Simulation results for central MPPT, Scenario-1: (a) PV system current (b) PV system power, (c) PV system voltage and (d) Duty ratio

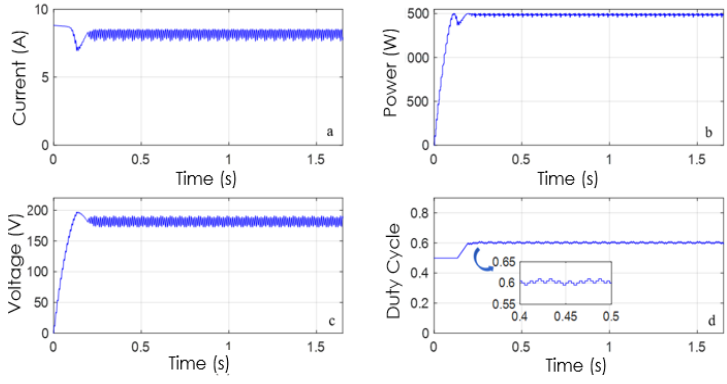

2.1.2. Scenario-2: Light Shadowing Condition

In the simulation, the radiation values coming to the PV modules changed in periods of 0.275s. Table 2 presents the global MPP and local MPP values obtained from the irradiance values and the P-V curve of the PV system. When the P-V curve is created in the specified time interval, two peaks are formed: global MPP and local MPP, and the same situation is detected in other time intervals. It can be understood from the color pattern given in Figure 3 that the PV modules are exposed to partial shading.

Table 2. Radiation amounts applied in central MPPT architecture Scenario-2 and power values in MPP

SCENARIO-2	TIME (s)					
	0-0.275	0.275-0.55	0.55-0.825	0.825-1.1	1.1-1.375	1.375-1.65
RADIATION 1 (W/m^2)	1000	800	600	500	400	200
RADIATION 2 (W/m^2)	1000	800	600	500	400	200
RADIATION 3 (W/m^2)	1000	800	600	500	400	200
RADIATION 4 (W/m^2)	200	400	500	600	800	1000
RADIATION 5 (W/m^2)	200	400	500	600	800	1000
RADIATION 6 (W/m^2)	200	400	500	600	800	1000
PEAK 1: POWER VALUE AT MPP (W)	730,31	661,06	797,1	797,1	661,06	730,31
PEAK 2: POWER VALUE AT LOCAL MPP (W)	336,97	589,6	444,75	444,75	589,6	336,97

Figure 3. Appearance of partial shadowing in Scenario-2

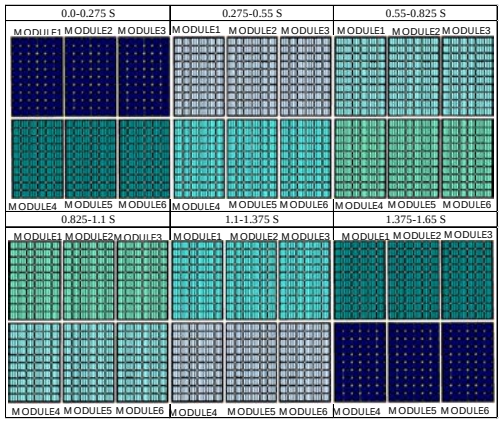

In Table 2, the power value in MPP in the time interval of 0.275-0.55s is 661W. As a result of the simulation study, 599W power was produced at the output of the PV modules during the mentioned time period. In this case, it was determined that the system could not reach the global MPP in the relevant time period and remained stuck in the local MPP. In Figure 4.(b), the moments when the PV system is stuck in the local MPP and the MPP cannot be reached in the time intervals of 0.55-0.825s, 0.825-1.1s and 1.1-1.375s are shown with a red frame. As a result of the simulation, MPPT efficiency was calculated as 75.85%.

Figure 4. Simulation results for central MPPT, Scenario-2: (a) PV system current, (b) PV system power, (c) PV system voltage and (d) Duty ratio

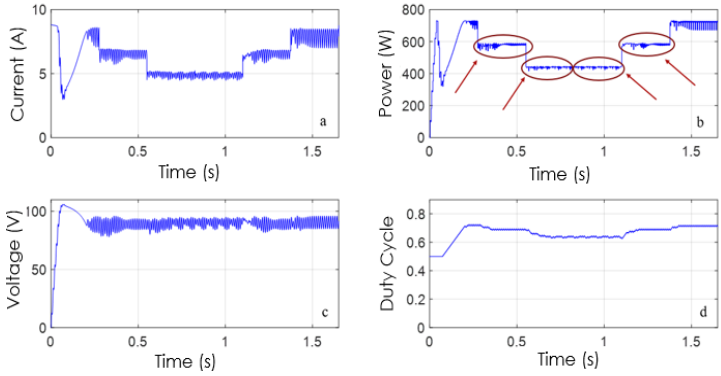

2.1.3. Scenario-3: Severe Partial Shadowing Condition

For Scenario-3, the global MPP and local MPP power values obtained by the radiation information applied to the PV modules and the P-V curve are given in Table 3. As given in Table 3, four different irradiance values were applied to the PV modules in the 0.275-0.55s time interval and 4 different MPP were formed in the P-V curve. In the range of 1.1-1.375s, six different irradiance values were applied to the PV modules and six peaks occurred in the P-V curve.

In Table 3, the MPP value in the 0-0.275s range is 334.75W, and when Figure 5.b is examined, it can be seen that 329.05W of power is produced. When the MPP power value given in Table 3 was compared with the power value produced as a result of the simulation, it was seen that the local MPP was reached. A similar situation occurred in the range of 1.1-1.375s. As a result of the simulation carried out for Scenario-3 in the central MPPT, the MPPT efficiency was calculated as 89.26%.

Table 3. Radiation in Scenario-3 and power values in MPP

SCENARIO-3	TIME (s)					
	0-0.275	0.275-0.55	0.55-0.825	0.825-1.1	1.1-1.375	1.375-1.65
RADIATION 1 (W/m^2)	1000	900	700	500	400	100
RADIATION 2 (W/m^2)	300	600	600	800	900	1000
RADIATION 3 (W/m^2)	650	750	800	900	950	1000
RADIATION 4 (W/m^2)	200	400	500	700	800	900
RADIATION 5 (W/m^2)	100	400	500	600	600	700
RADIATION 6 (W/m^2)	300	400	400	600	700	800
PEAK 1: POWER VALUE AT MPP (W)	334,75	657,99	685,92	850,63	838,71	968,99
PEAK 2: POWER VALUE AT LOCAL MPP (W)	329,05	482,78	679,1	809,93	758,54	857,52
PEAK 3: POWER VALUE AT LOCAL MPP (W)	289,12	376,17	476,73	552,16	703,49	691,75
PEAK 4: POWER VALUE AT LOCAL MPP (W)	217,02	196,47	349,1	396,41	623,45	473,74
PEAK 5: POWER VALUE AT LOCAL MPP (W)	177,5		175,47	196,46	437,39	184,12
PEAK 6: POWER VALUE AT LOCAL MPP (W)					202,79	

Figure 5. Simulation results for central MPPT Scenario-2: (a) PV system current, (b) PV system power, (c) PV system voltage and (d) Duty ratio

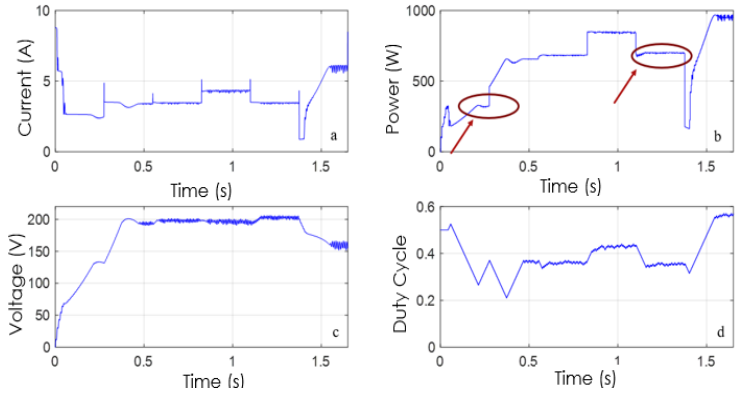

2.2. Module Based MPPT Architecture

In module-based MPPT, MPPT process is carried out separately for each PV module. The PV module specified in Table 4 was used in the simulation studies, and the outputs of the PV modules were connected separately to the independent boost converter. The features of the components used in the module-based MPPT architecture are given in Table 4. Since PV modules are connected in series in the central MPPT architecture, the amount of power produced is negatively affected in case of partial shading caused by different radiations. However, in the module-based MPPT architecture, since the MPPT process occurs independently in the PV modules, the power produced by the PV modules exposed to different radiation does not change.

Table 4. Features of the components of the module-based MPPT

PV Module Features		Values of the boost DC-DC converter	
Power at MPP (W)	250,05	C_{INPUT} (F)	250µ
Voltage at MPP (V)	30,31	C_{OUTPUT} (F)	83.33µ
Current at MPP (A)	8,25	Inductors (H)	0.42m
Open circuit voltage value (V)	37,9	Resistance (Ω)	25
Short circuit current (A)	8,82		

2.2.1. Scenario-1: Regular Radiation Condition

In the module-based MPPT architecture, the radiation reaching each PV module is 1000W/m^2. As a result of the simulation in the module-based MPPT architecture, a power value of 250W was reached under 1000W/m^2 radiation and MPPT was achieved. As a result of the simulation, the MPPT efficiency was calculated as 99.34%.

2.2.2. Scenario-2: Light Shadowing Condition

The radiation values applied to the PV modules for the simulation study and the power values of the MPP obtained from the P-V curve are given in Table 5.

Simulation results are shown in Figure 6 for PV module-1, PV module-2 and PV module-3, and in Figure 7 for PV module-4, PV module-5 and PV module-6. It has been determined that the power values of MPP shared in the relevant time intervals in Table 5 have been reached in Figure 6.b and Figure 7.b. As a result of the simulation study, the MPPT efficiency value was calculated as 98.09% for the PV modules in the first group and 97.1% for the modules in the second group.

Table 5. Radiation amounts applied in Scenario-2 and power values in MPP

SCENARIO-2		TIME (s)					
		0-0.275	0.275-0.55	0.55-0.825	0.825-1.1	1.1-1.375	1.375-1.65
PV MODULE 1, 2 ve 3	RADIATION (W/m^2)	1000	800	600	500	400	200
	PEAK 1: POWER VALUE AT MPP (W)	250,07	201,83	152,22	126,96	101,45	49,98
PV MODULE 4, 5 ve 6	RADIATION (W/m^2)	200	400	500	600	800	1000
	PEAK 1: POWER VALUE AT MPP (W)	49,98	101,45	126,96	152,22	201,83	250,07

Figure 6. Simulation results of the first group of modules in module-based MPPT Scenario-2: (a) PV module current, (b) PV module power, (c) PV module voltage and (d) Duty ratio

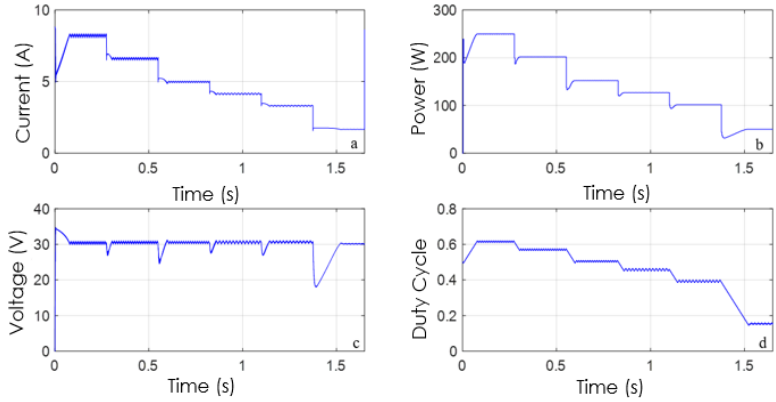

Figure 7. Simulation results of the second group of modules in module-based MPPT Scenario-2: (a) PV system current, (b) PV system power, (c) PV system voltage and (d) Duty ratio

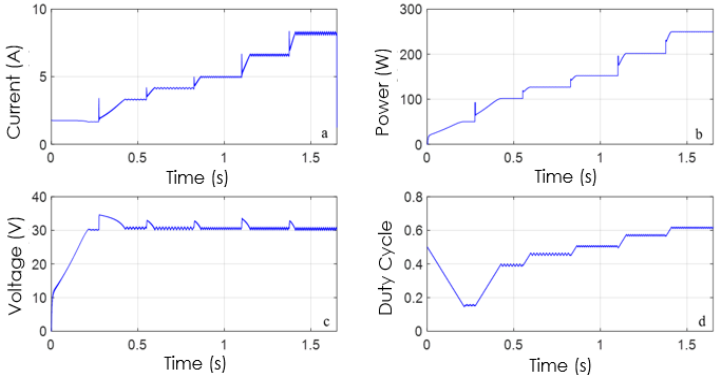

In Table 5, the radiation values applied to the first group of PV modules decreased throughout the simulation period, and in this context, the power values produced at the module output also decreased. According to the power change in Figure 6.b, the power values produced by the PV module decreased over time in accordance with Table 5. The opposite of this situation occurred

in the second group of PV modules. During the simulation period, the radiation values increased and the amount of power produced increased accordingly.

2.2.3. Scenario-3: Severe Partial Shadowing Condition

In the module-based MPPT, the radiation applied to the PV modules in Scenario-3 and the MPP power values for these radiation situations are given in Table 6. As a result of the module-based MPPT architecture Scenario-3 simulation, it was observed that PV module-2, PV module-3, PV module-4, and PV module-6 reached the MPP during the simulation period and the MPPT was achieved. It was determined that MPP could not be reached when exposed to 100W/m^2 radiation between 1.375-1.65s in PV module-1 and 0-0.275s in PV module-5. In Table 6, the MPP power value in the P-V curve for 100W/m^2 radiation is 24.36W, and the power value produced as a result of the simulation is 16W. In this case, it was determined that less power was produced than the power value obtained in the P-V curve.

Table 6. Module-based MPPT: Radiation amounts applied in Scenario-3 and power values in MPP

SCENARIO-3		TIME (s)					
		0-0.275	0.275-0.55	0.55-0.825	0.825-1.1	1.1-1.375	1.375-1.65
PV MODULE-1	RADIATION (W/m^2)	1000	900	700	500	400	100
	PEAK 1: POWER VALUE AT MPP (W)	250,07	226,13	177,18	126,96	101,45	24,36
PV MODULE-2	RADIATION (W/m^2)	300	600	600	800	900	1000
	PEAK 1: POWER VALUE AT MPP (W)	75,75	152,22	152,22	201,83	226,13	250,07
PV MODULE-3	RADIATION (W/m^2)	650	750	800	900	950	1000
	PEAK 1: POWER VALUE AT MPP (W)	164,74	189,55	201,83	226,13	238,15	250,07
PV MODULE-4	RADIATION (W/m^2)	200	400	500	700	800	900
	PEAK 1: POWER VALUE AT MPP (W)	49,98	101,45	126,96	177,18	201,83	226,13
PV MODULE-5	RADIATION (W/m^2)	100	400	500	600	600	700
	PEAK 1: POWER VALUE AT MPP (W)	24,36	101,45	126,96	152,22	152,22	177,18
PV MODULE-6	RADIATION (W/m^2)	300	400	400	600	700	800
	PEAK 1: POWER VALUE AT MPP (W)	75,75	101,45	101,45	152,22	177,18	201,83

When the simulation results are examined, MPPT was performed at high irradiance values. However, when a low irradiance value of 100W/m^2 was applied to the PV modules, MPP could not be reached. The reason for this situation is that when a boost converter is used in MPPT, the MPPT performance of the system is negatively affected by the decrease in the solar radiation intensity affecting the PV modules and the system cannot operate in MPPT. In boost converters, the instantaneous power produced by the PV module is equal to the product of the PV module current and voltage. The ratio of PV module voltage to PV module current will give the instantaneous PV module internal impedance. If this impedance value is less than the load resistance, MPPT cannot be achieved. This is a frequently experienced situation, especially at low irradiance, due to the increase in the instantaneous internal impedance of the PV module [8]. Results show that the calculated efficiency values of PV module-1, PV module-2, PV module-3, PV module-4, PV module-5 and PV module-6 are 97.4%, 97.87%, 99.77%, 97.16%, 96.03% and 98.4%, respectively.

2.3. Sub-Module Based MPPT Architecture

The PV module used in the simulations consists of three sub-modules. Therefore, there are a total of 18 sub-modules in six PV modules. Figure 8 shows the PV module and sub-module representation. In the sub-module based MPPT architecture, simulation studies carried out in MATLAB/SIMULINK, 18 sub-modules and a boost converter were used for each sub-module. The appearance of PV sub-modules in partial shading is given in Figure 8.c, and the numbering of PV sub-modules is done from left to right. The features of the system components used in the sub-module-based MPPT architecture are presented in Table 7.

Table 7. Features of the components of sub-module based MPPT

PV Sub-Module Features		Values of the boost DC-DC converter	
Power at MPP (W)	83,35	C_{INPUT} (F)	83.33µ
Voltage at MPP (V)	10,1	C_{OUTPUT} (F)	27.78µ
Current at MPP (A)	8,25	Inductors (H)	0.14m
Open circuit voltage value (V)	12,63	Resistance (Ω)	8,33
Short circuit current (A)	8,82		

2.3.1. Scenario-1: Regular Radiation Condition

In the sub-module based MPPT architecture, 1000W/m^2 radiation reaches all 18 sub-modules. Under this operating condition, the MPP power value in the P-V curve of each sub-module is 83.32W and the voltage value is 10.1V.

In Scenario-1, PV sub-modules produced 83.32W power and MPPT was realized. As a result of the simulation, the MPPT efficiency for PV sub-modules was calculated as 99.3%.

Figure 8. (a) PV module, (b) sub-module and (c) sub-modules

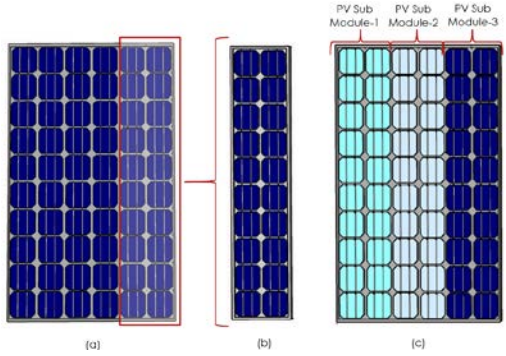

2.3.2. Scenario-2: Light Shadowing Condition

In the simulation study carried out for Scenario-2 in the module-based MPPT architecture, PV module-1, PV module-2 and PV module-3 were exposed to equal radiation. Likewise, PV module-4, PV module-5 and PV module-6 have equal radiation values. In the sub-module based MPPT architecture, the radiation

values in the module-based MPPT architecture are left exactly the same in one sub-module of the relevant module. The other two sub-modules were exposed to different radiation. For example; If the PV module was exposed to 1000W/m^2 in the module-based MPPT architecture, it was exposed to 1000W/m^2, 900W/m^2 and 800W/m^2 in the sub-module-based MPPT architecture. This stated situation is valid for the sub-modules in PV module-2 and PV module-3. Irradiance values created in the sub-modules of PV module-1, PV module-2 and PV module-3 were also applied to the sub-modules of PV module-4, PV module-5 and PV module-6. In Table 8, the irradiance values of the sub-module MPPT architecture Scenario-2 and the power values of the MPP in the P-V curve are given.

In the simulation studies carried out according to the results given in Table 8, MPPT was provided for PV sub-modules using the P&O algorithm, since there is no multiple peak structure in the sub-module P-V curves.

Table 8. Sub-module based MPPT: Radiation amounts applied in Scenario-2 and power values in MPP

SCENARIO-2			TIME (s)					
			0-0.275	0.275-0.55	0.55-0.825	0.825-1.1	1.1-1.375	1.375-1.65
PV MODULE 1-3	SUB MODULE 1,4,7	RADIATION (W/m2)	1000	800	600	500	400	200
		POWER VALUE AT MPP (W)	83,32	67,25	50,72	42,3	33,8	16,65
	SUB MODULE 2,5,8	RADIATION (W/m2)	900	700	800	600	500	600
		POWER VALUE AT MPP (W)	75,35	59,04	67,25	50,72	42,3	50,72
	SUB MODULE 3,6,9	RADIATION (W/m2)	800	500	1000	700	600	800
		POWER VALUE AT MPP (W)	67,25	42,3	83,32	59,04	50,72	67,25
PV MODULE 4-6	SUB MODULE 10,13,16	RADIATION (W/m2)	200	400	500	600	800	1000
		POWER VALUE AT MPP (W)	16,65	33,8	42,3	50,72	67,25	83,32
	SUB MODULE 11,14,17	RADIATION (W/m2)	400	700	700	800	600	1000
		POWER VALUE AT MPP (W)	33,8	59,04	59,04	67,25	50,72	83,32
	SUB MODULE 12,15,18	RADIATION (W/m2)	600	900	900	1000	500	1000
		POWER VALUE AT MPP (W)	50,72	75,35	75,35	83,32	42,3	83,32

2.3.3. Scenario-3: Severe Partial Shadowing Situation

Irradiance values applied to sub-modules for sub-module based MPPT architecture Scenario-3 are presented in Table 9. Although Scenario-3 represents a severe partial shadowing situation, MPPT performance is high since MPPT is performed separately in the sub-modules.

When Table 9 is examined, it is seen that, except for the irradiance value of 100W/m^2, MPP is reached and MPP is monitored according to the power values produced at the output of the PV sub-modules in other applied radiations. At low irradiances, the reason for this situation is that the boost converter negatively affects the operating performance of MPP at low radiations [8].

Table 9. Sub-module based MPPT: Radiation amounts applied in Scenario-3 and power values in MPP

SCENARIO-3			TIME (s)						
			(0-0.275)	(0.275-0.55)	(0.55-0.825)	(0.825-1.1)	(1.1-1.375)	(1.375-1.65)	
PV MODULE 1	SUB MODULE 1	RADIATION (W/m2)	1000	900	700	500	400	100	
		POWER VALUE AT MPP (W)	83,32	75,35	59,04	42,3	33,8	8,12	
	SUB MODULE 2	RADIATION (W/m2)	400	800	800	400	500	300	
		POWER VALUE AT MPP (W)	33,8	67,25	67,25	33,8	42,3	25,24	
	SUB MODULE 3	RADIATION (W/m2)	600	700	700	600	600	500	
		POWER VALUE AT MPP (W)	50,72	59,04	59,04	50,72	50,72	42,3	
PV MODULE 2	SUB MODULE 4	RADIATION (W/m2)	300	600	600	800	900	1000	
		POWER VALUE AT MPP (W)	25,24	50,72	50,72	67,25	75,35	83,32	
	SUB MODULE 5	RADIATION (W/m2)	900	400	400	900	800	800	
		POWER VALUE AT MPP (W)	75,35	33,8	33,8	75,35	67,25	67,25	
	SUB MODULE 6	RADIATION (W/m2)	500	200	200	500	700	600	
		POWER VALUE AT MPP (W)	42,3	16,65	16,65	42,3	59,04	50,72	
PV MODULE 3	SUB MODULE 7	RADIATION (W/m2)	650	750	800	900	950	1000	
		POWER VALUE AT MPP (W)	54,89	63,16	67,25	75,35	79,35	83,32	
	SUB MODULE 8	RADIATION (W/m2)	500	600	600	500	850	500	
		POWER VALUE AT MPP (W)	42,3	50,72	50,72	42,3	71,31	42,3	
	SUB MODULE 9	RADIATION (W/m2)	400	400	400	400	750	400	
		POWER VALUE AT MPP (W)	33,8	33,8	33,8	33,8	63,16	33,8	
PV MODULE 4	SUB MODULE 10	RADIATION (W/m2)	200	400	500	700	800	900	
		POWER VALUE AT MPP (W)	16,65	33,8	42,3	59,04	67,25	75,35	
	SUB MODULE 11	RADIATION (W/m2)	800	300	300	800	500	800	
		POWER VALUE AT MPP (W)	67,25	25,24	25,24	67,25	42,3	67,25	
	SUB MODULE 12	RADIATION (W/m2)	100	100	100	100	300	700	
		POWER VALUE AT MPP (W)	8,12	8,12	8,12	8,12	25,24	59,04	
PV MODULE 5	SUB MODULE 13	RADIATION (W/m2)	100	400	500	600	600	700	
		POWER VALUE AT MPP (W)	8,12	33,8	42,3	50,72	50,72	59,04	
	SUB MODULE 14	RADIATION (W/m2)	300	600	600	300	400	500	
		POWER VALUE AT MPP (W)	25,24	50,72	50,72	25,24	33,8	42,3	
	SUB MODULE 15	RADIATION (W/m2)	500	800	800	500	100	400	
		POWER VALUE AT MPP (W)	42,3	67,25	67,25	42,3	8,12	33,8	
PV MODULE 6	SUB MODULE 16	RADIATION (W/m2)	300	400	400	600	700	800	
		POWER VALUE AT MPP (W)	25,24	33,8	33,8	50,72	59,04	67,25	
	SUB MODULE 17	RADIATION (W/m2)	600	600	600	600	600	600	
		POWER VALUE AT MPP (W)	50,72	50,72	50,72	50,72	50,72	50,72	
	SUB MODULE 18	RADIATION (W/m2)	900	800	800	900	500	400	
		POWER VALUE AT MPP (W)	75,35	67,25	67,25	75,35	42,3	33,8	

Figure 9 shows the difference in the amount of radiation applied to the system and the appearance of partial shading on the PV modules in the sub-module-based MPPT architecture. When the radiation distributions in Figure 9 are compared to the radiation values in Scenario-2, the partial shadowing situation in

the simulation study of Scenario-3 carried out at the sub-module level is higher than in Scenario-2.

When the simulation results are examined, when 100W/m^2 radiation intensity is applied in sub-module-1, sub-module-12 and sub-module-15, the amount of power produced did not reach the MPP value specified in Table 9. Under this radiation condition, the amount of power produced by the sub-module was determined as 7W. The amount of power produced at radiation values other than the time intervals where 100W/m^2 radiation intensity was applied reached the power values in MPP presented in Table 9 and MPP was tracked.

Figure 9. Appearance of partial shadowing in Scenario 3 in the sub-module MPPT architecture

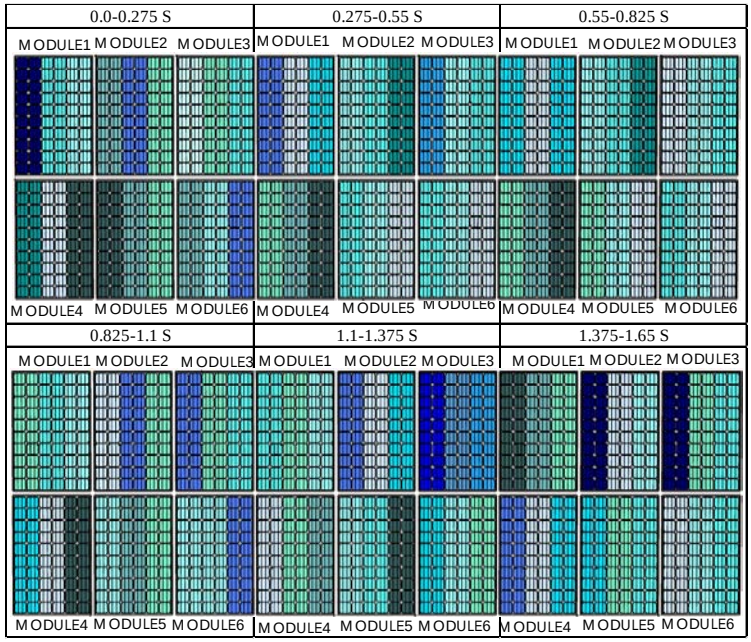

As a result of the simulation, the efficiencies from sub-module-1 to sub-module-18 are 97.46%, 96.88%, 99.81%, 98.26%, 96.48%, 95.46%, 99.85%, 98.38%, 97.51%, 97.42%,

93.75%, 84.66%, 95.11%, 96.5%, 93.97%, 98.69%, 99.95%, 98.84%, respectively.

3. CONCLUSIONS

PV modules are used to generate electricity from solar energy. PV modules are affected by temperature, radiation, weather conditions and shading. Within the scope of the study, investigations were made for central MPPT, module-based MPPT, sub-module-based MPPT architectures under normal conditions, light and severe partial shadowing situations by using the boost converter with P&O algorithm, and it was aimed to increase the system efficiency.

The MPPT architectures specified in the simulation studies are created and the power amounts produced in the system and the efficiency values of MPPT monitoring are analyzed. The efficiency values calculated in the simulation studies carried out for Scenario-2 are 75.85% in the central MPPT architecture, between 97.1% and 98.09% in the module-based MPPT architecture, and between 97.54% and 99.08% in the sub-module-based MPPT architecture. In the simulation study conducted for Scenario-3, the MPPT efficiency was calculated as 89.26% in the central MPPT architecture, 96.03% to 99.77% in the module-based MPPT architecture, and 84.66% to 99.95% in the sub-module-based MPPT architecture. As a result of the studies, the highest amount of power produced in the PV system according to the architectures was determined as sub-module-based MPPT, module-based MPPT and central MPPT, respectively. Thanks to this study, simulation studies were carried out on the MPPTs that should be selected when PV modules are wanted to be integrated into the roof façade of the building. According to the simulation results, the architectural choice of sub-module MPPT was

deemed appropriate in the PV system that will be integrated into the building roof.

REFERENCES

[1] Dirks, E., Gole, A.M. ve Molinski, T.S. (2006). Performance Evaluation of a Building Integrated Photovoltaic Array using an Internet Based Monitoring System. 2006 IEEE Power Engineering Society General Meeting, Montreal, QC, Canada, 5.

[2] Özdoğan, H.P. (2005). Ekololojik Binalarda Bina Kabuğunda Kullanılan Fotovoltaik Panellerin Tasarım Bağlamında İncelenmesi. Yayımlanmamış yüksek lisans tezi. Yıldız Teknik Üniversitesi, İstanbul.

[3] Dirks, E., Gole, A.M. and Molinski, T.S. (2006). Performance Evaluation of a Building Integrated Photovoltaic Array using an Internet Based Monitoring System. 2006 IEEE Power Engineering Society General Meeting, Montreal, QC, Canada, 5.

[4] Ekici, B.B. (2015). Farklı Yönler Bakan Cephelerdeki Bina Entegre Fotovoltaik (BIPV) Sistem Performanslarının Değerlendirilmesi. 2. Ulusal Yapı Kongresi ve Sergisi, 3- 5 Haziran, Ankara, Bildiriler Kitabı, 425-435.

[5] Başoğlu, M.E. (2013). Güneş Enerjisi Sistemlerinde Kullanılan Maksimum Güç Noktası İzleyicili Yükseltici DA-DA Dönüştürücü Analizi ve Gerçekleştirilmesi. Yayımlanmamış yüksek lisans tezi. Kocaeli Üniversitesi, Kocaeli.

[6] Keskin, Y.E. (2014). Fotovoltaik Sistemlerde Maksimum Güç Noktası İzleme Yöntemlerinin Karşılaştırılması. Yayımlanmamış yüksek lisans tezi. Kocaeli Üniversitesi, Kocaeli.

[7] Güngör, O. (2018). Fotovoltaik modüllerde maksimum güç takibi için dönüştürücü ve algoritmik yöntemlerin incelenmesi. Yayımlanmamış yüksek lisans tezi, Sakarya Üniversitesi, Sakarya.

[8] Başoğlu M.E. and Çakır, B. (2016). Comparisons of MPPT performances of isolated and nonisolated DC-DC converters by using a new approach, Renewable and Sustainable Energy Reviews, 60, 1100–1113.

FACILE SYNTHESIS AND SPECTRAL STUDIES OF NiO NANOSTRUCTURES

Emin YAKAR[1]

Fatma SARF[2]

1. INTRODUCTION

Studies on the band-gap-controlled metal oxide nanostructures have been progressing in the industrial applications such as magnetic memory devices[1], optoelectronic devices [2], electrochemical energy storage systems [3] and electrochromic devices [4]. As a transition metal oxide type semiconductor, NiO is intrinsic p-type material and has a wide band gap of ~3.4-4.0 eV with its high chemical stability and high optical transparency. Ongoing research is aimed at maximizing the potential of the NiO in different kind photonic technologies [5]. Another important condition is to be able to achieve this with low-cost production methods. The following Table 1 lists some inexpensive NiO production methods;

Table 1. Some of the types of low-cost NiO nanoparticle studies available in 2023 year

Production type	Application field	Reference
Biogenic synthesis	Biomedical	*Velsankar et.al.* [6]
Green combustion	Gas sensor	*Ananthi et.al.* [7]
Co-precipitation	Opto-electronic and data storage	*Boukhari et.al.* [8]
Chemical precipitation	Solar cell	*Hassan et.al.* [9]
sol–gel auto-combustion	Photocatalyst	*Khan et.al.* [10]

[1] Dr. Öğr. Üyesi, Çanakkale Onsekiz Mart Üniv./ Müh.Fak./Malzeme Bilimi ve Mühendisliği, eyakar@comu.edu.tr, ORCID: 0000-0001-7747-953X.

[2] Doç. Dr. Çanakkale Onsekiz Mart Üniv./Çan MYO/Yönetim ve Organizasyon, fatmaozutok@comu.edu.tr, ORCID: 0000-0002-4445-4800.

Unlike physical methods such as vapor-phase, laser ablation and e-beam lithography, chemical methods such as sono-chemical, hydrothermal, sol-gel and chemical reduction provides good production rate, large scale production and applying even at low temperatures. Among them, the co-precipitation method avoids the use of multi-materials and leads to inexpensive process and provides uncomplicated chemical reactions.

Due to the electron deficiency of pure NiO which created substantial effects on the optical properties. To improve the optical properties of NiO nanoparticles, one of the effective strategy is doping with proper (generally as metals) element/s such as Fe [11], Co [12], Mn [13] and Al [14]. Because, the deviation of NiO from perfect stoichiometry can be achieved by doping or adding new elements during the synthesis process under favorable production conditions [8]. Another frequently used approach is NiO-nanoparticle decorated C-based material nanocomposite forms for enhancing the optical characteristics [15]. For example, MWCNTs have nonlinearity and a broad spectrum response and integrated with NiO to improve the nonlinear optical efficiency [16].

This study aims to provide an explanation of the improvement of optical properties of the chemical bath deposition method by converting waste chemicals into NiO nanoparticles by co-precipitation method.

2. CONTENT OF THE STUDY

Chemical wastes, which contain quite a big hazardous for the environment and public health which turn into a valuable nanotechnology material in this work. For this purpose, the waste chemicals of the chemical bath deposition, using produce the NiO thin films, used in our previous study were converted into NiO nanoparticles by co-precipitation, which is a simple and

inexpensive method. The structural and optical properties of the synthesized NiO structures were examined and introduced to the literature. In a similar study previously, $Zn_{1-x}Cu_xO$ was produced in a similar way and its optical properties were examined [17]**.**

In our previous study, the NiO-1 and NiO-2 coded with different concentrations samples [18] were filtered by co-precipitation method with using ethanol and distilled water for several times and dried at 120 °C. Finally, the resulting powder particles were annealed at 500 °C to remove surface residues. Structural properties of the obtained NiO particles were examined by Rigaku SmartLab x-ray diffractometer through a CuK_α source in between 2Θ=20°-80° range. Transmittance spectra was obtained by using ultraviolet–visible (Perkin-Elmer UV–Vis Lambda 2S Spectrometer). All characterization measurements were realized at 25 °C.

3. RESULTS

In Figure 1, x-ray patterns of produced NiO nanoparticles were depicted. Well-defined patterns are recorded around at 32.35, 39.79 and 62.18° which corresponding to (111), (200) and (220) indexed face-centered cubic NiO geometry (JCPDS card number 01-073-1523), respectively. However, the observed peaks related to extra phases (marked as *) were determined, as shown in 2Θ~50° corresponding to (102) indexed $Ni(OH)_2$ precursor phase (JCPDS card number 14-0117) [19].

Figure 1. x-ray patterns of NiO nanoparticles

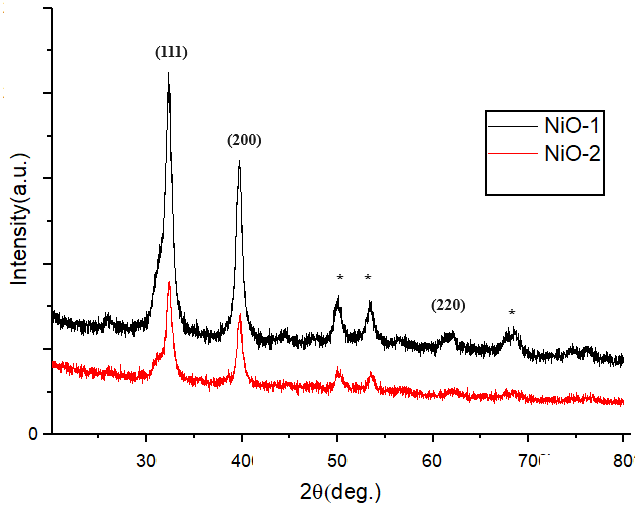

In Figure 2, structural parameters of particles were shown. The crystallite size was calculated according to the well-known Debye Scherrer Model, as formulated by Equation 1;

$D = 0.94\lambda/\beta \cos \Theta$ (Equation 1)

where, λ is the wavelength produced by X-rays (1.54 Å), β is the full-width at half maximum, and θ is the angle of diffraction. Lattice strain is another important parameter which interests presence of crystal imperfections and distortion in the material, as formulated by Equation 2;

$\beta = 4\varepsilon \tan 4\Theta$ (Equation 2)

where, ε is the micro strain in the lattice. The lattice constant is ‘’a’’ the cubic structure of NiO can be calculated by Equation 3;

$a = \sqrt{d^2}(h^2 + k^2 + l^2)$ (Equation 3)

Average grain size slightly decreased and lattice strain slightly increased with increasing nickel concentration in NiO-2 samples. This can be attributed to distortions and imperfections in host crystal structure. From these results, waste NiO nanoparticle

crystal quality depends on the growth process from $Ni(OH)_2$ to NiO with changing nickel concentration.

Figure 2. Structural parameters of NiO nanoparticles

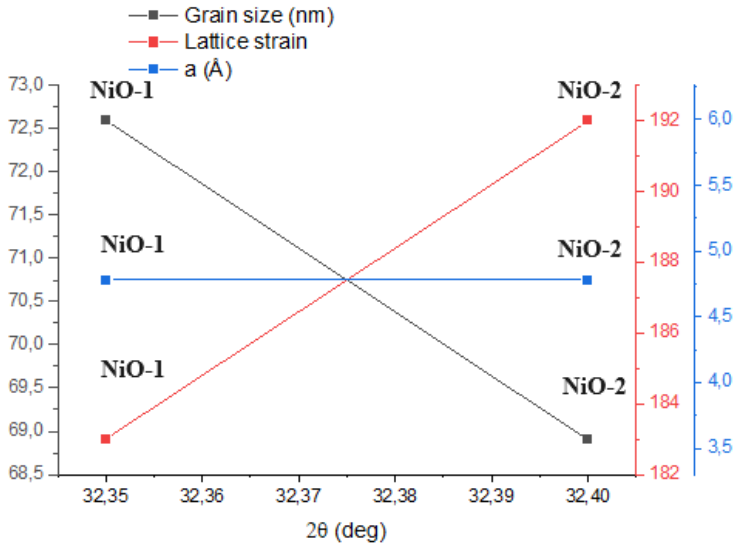

Figure 3. Optical transperancy spectra of NiO nanoparticles

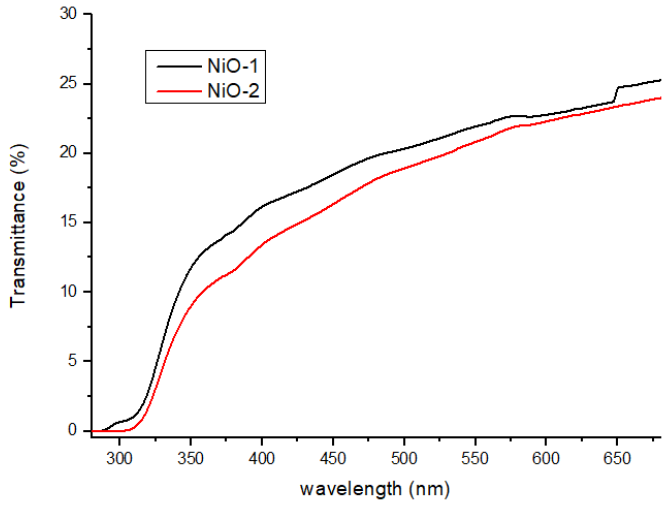

In Table 2, some optical parameters of NiO nanoparticles were depicted according to production process. From these results, the green synthesis method has been attractive in recent years through obtained wide optical band gap of NiO nanoparticles.

Table 2. Comparison of optical properties of NiO nanoparticles

Synthesis Method	Crystal-lite size (nm)	Optical abs. edge (nm)	E_g (eV)	Reference
co-precipitation	19.5	-	3.51	*Boukhari et.al.,2023* [8]
thermal decomposition	37.5	329.5	3.54	*El-Kemary et.al.*,2013 [20]
Green synthesis	30	330	-	*Sivagami et.al.* , 2022 [21]
Green synthesis	20-30	268-278	3.82-4.43	*Anand et.al.*, 2020, [22]
co-precipitation	68.9-72.6	315	-	*Present study*[*]

REFERENCES

[1] Gandhi A.C., Li T-Y, Kumar B.V., Reddy P.M., Peng J-C, Wu C-M, Wu S.Y.(2020). Room Temperature Magnetic Memory Effect in Cluster-Glassy Fe-Doped NiO Nano-particles. *Nanomaterials,* 10(7):1318.

[2] Yu X, Marks T.J., Facchetti A. (2016). Metal oxides for optoelectronic applications. *Nat Mater,* 15(4):383-96.

[3] Seok D, Jeong Y, Han K, Yoon DY, Sohn H. (2019). Recent Progress of Electrochemical Energy Devices: Metal Oxide–Carbon Nanocomposites as Materials for Next-Generation Chemical Storage for Renewable Energy. *Sustainability*, 11(13):3694

[4] Rozman M, Cetin N, Bren U, Lukšič M. (2021). Use of Different Metal Oxide Coatings in Stainless Steel Based ECDs for Smart Textiles. *Electronics*, 10(20):2529.

[5] Aivalioti C, Papadakis A, Manidakis E, Kayambaki M, Androulidaki M, Tsagaraki K, Pelekanos NT, Stoumpos C, Modreanu M, Crăciun G, et al. (2021). Transparent All-Oxide Hybrid NiO:N/TiO_2 Heterostructure for Optoelectronic Applications. *Electronics*, 10(9):988.

[6] Velsankar K. , Aravinth K. , Wang Yong, Mohandoss S. , Rok Lee Yong, Ana Cláudia Paiva-Santos, (2023). NiO nanoparticles, an algorithm of their biosynthesis, toxicity, and biomedical activities, *Journal of Molecular Structure*, 1291.

[7] S. Ananthi, M. Kavitha, A. Balamurugan, E. Ranjith Kumar, G. Magesh, A.F. Abd El-Rehim, Ch. Srinivas, P. Anilkumar, J. Suryakanth, C. Sharmila Rahale (2023), Synthesis, analysis and characterization of camellia sinensis mediated synthesis of NiO nanoparticles for ethanol gas sensor applications, *Sensors and Actuators B: Chemical*, 387.

[8] J. Al Boukhari, A.A. Azab, Z. Bitar, R. Awad (2023). Influence of (Mg, Cu) codoping on the structural, optical and magnetic properties of NiO nanoparticles synthesized by coprecipitation method, *Physica B: Condensed Matter*, 663.

[9] Sara Hassan, A. El-Shaer, A.H. Oraby, E. Salim (2023). Investigations of charge extraction and trap-assisted recombination in polymer solar cells via hole transport layer doped with NiO nanoparticles,*Optical Materials*, 145.

[10] Afroz Khan, Md. Saad, Tausif Kamal, F. Rahman (2023). Structural, morphological, optical and UV-light driven enhanced photocatalytic properties of Fe-doped NiO nanoparticles, Materials Chemistry and Physics, 305.

[11] Minisha S, Johnson J, Mohammad Wabaidur S, Gupta JK, Aftab S, Siddiqui MR, Lai W-C (2023). Synthesis and Characterizations of Fe-Doped NiO Nanoparticles and Their Potential Photocatalytic Dye Degradation Activities. *Sustainability*, 15(19):14552

[12] Marand ZR, Kermanpur A, Karimzadeh F, Barea EM, Hassanabadi E, Anaraki EH, Julián-López B, Masi S, Mora-Seró I (2020). Structural and Electrical Investigation of Cobalt-Doped NiO_x/Perovskite Interface for Efficient Inverted Solar Cells. *Nanomaterials*. 10(5):872

[13] S. Sivakumar, Nazir Ahmad Mala (2022). Synthesis and characterization of manganese doping on NiO nanoparticles and its supercapacitor applications, *Materials Today: Proceedings,* 49 (5): 1469-1474.

[14] Irum Sidra, Andleeb Saadia, Sardar Sumbal, Mustafa Zeeshan, Ghaffar Ghazanfar, Mumtaz M., Mubasher , Arslan Muhammad, Abbas Mudassar (2021). Chemical Synthesis and Antipseudomonal Activity of Al-Doped NiO Nanoparticles, *Frontiers in Materials,* 8.

[15] Samuel R. Cantrell, Eric Welch, Luisa M. Scolfaro, Wilhelm J. Geerts, Opto-electronic properties of carbon doped NiO, *Journal of Physics and Chemistry of Solids,* 174, 111110.

[16] Tahani A. Alrebdi, Hoda A. Ahmed, Fatemah H. Alkallas, Eman A. Mwafy, Amira Ben Gouider Trabelsi, Ayman M. Mostafa (2022). Structural, linear and nonlinear optical properties of NiO nanoparticles–multi-walled carbon nanotubes nanocomposite for optoelectronic applications, *Radiation Physics and Chemistry*,195, 110088.

[17] Yakar, E., (2023). Determination of Structural and Optical Properties of Zn1-xCuxO Nanoparticles by Chemical Bath Deposition Waste Recovery Technique. Journal of advanced research in natural and applied sciences (Online) , vol.9, no.3, 710-718.

[18] Sarf, F., (2022). Impurity Defect Induced Ferromagnetism Investigation of SiO2-Supported NiO Particles. Journal Of The Mexican Chemical Society , vol.66, 34-41.

[19] Wang, R., Lang, J., Liu, Y. *et al.* (2015). Ultra-small, size-controlled $Ni(OH)_2$ nanoparticles: elucidating the relationship between particle size and electrochemical performance for advanced energy storage devices. *NPG Asia Mater* **7**, e183.

[20] M. El-Kemary, N. Nagy, I. El-Mehasseb (2013). Nickel oxide nanoparticles: Synthesis and spectral studies of interactions with glucose, Materials Science in Semiconductor Processing, 16 (6): 1747-1752

[21] M. Sivagami, I.V. Asharani (2022). Phyto-mediated Ni/NiO NPs and their catalytic applications-a short review, Inorganic Chemistry Communications, 145, 110054.

[22] G. Theophil Anand, R. Nithiyavathi, R. Ramesh, S. John Sundaram, K. Kaviyarasu (2020). Structural and optical properties of nickel oxide nanoparticles: Investigation of antimicrobial applications, *Surfaces and Interfaces*, 18, 100460,

ADSORPTION AND BIODEGRADATION OF PARACETAMOL USING ACTIVATED SLUDGE IN DOMESTIC WASTEWATER TREATMENT PLANTS

Ayşe ÖZGÜVEN[1]

1. INTRODUCTION

In recent years, there has been a significant increase in the production and usage of pharmaceutical compounds for treating human and animal diseases. Studies on the existence and fate of microcontaminants in the environment resulting from pharmaceutical active ingredients have increased over the last 20 years with the development of new technologies (Quintelas et al. 2020; Özgüven 2020; Özgüven et al. 2021; Özgüven et al. 2022). Pharmaceuticals, used in medicine to promote human health, have different functions, structures, behaviors and activities. Many pharmaceutical compounds are excreted from the body through feces or urine. Pharmaceutical compounds are often eliminated from the body through feces or urine. Once excreted by the body, these compounds and their metabolites are excreted in groundwater, surface water and drinking water (Whitacre et al. 2010; Li et al. 2013; Schaider et al. et al. 2014). Some pharmaceutical compounds are highly metabolized, while others are moderately or poorly metabolized. Conversion processes can be hydrolysis, photo-oxidation or biotic oxidation. The resulting metabolites differ both pharmacologically and toxicologically compared to the parent drugs (Maculewicz et al. 2022).

[1] Department of Environmental Engineering, Faculty Engineering, Van Yüzüncü Yıl University, ayseozguven@yyu.edu.tr, ORCID: 0000-0003-1071-2813.

Paracetamol, analgesic (painkiller) and is a pharmaceutical substance widely used as an antipyretic (antipyretic) (Samal et al. 2022). Paracetamol is typically found in environmental settings at low microgram concentrations per liter (μg/L) and can be detected in around 75% of natural water sources like rivers and lakes (Ternes et al. 2005; Li et al. 2010).

Activated sludge processes are one of the classical methods used in the biological treatment of wastewater. It has been shown in some studies that more than 90% removal of paracetamol is achieved using conventional activated sludge and batch reactors with membrane bioreactors (Erkus et al. 2015; Alobaidi et al. 2021). This means that paracetamol is biodegraded by the activated sludge found in wastewater treatment plants. Biological treatment plants' ability to remove compounds depends on their physicochemical properties, wastewater technology, hydraulic retention time (HRT), solid retention time (SRT), and climatic conditions. (Kasprzyk-Hordern et al. 2009; Sahar et al. 2011). Domestic wastewater treatment plants are generally not designed to remove medical or pharmaceutical compounds. Most pharmaceutical active ingredients are not effectively removed by conventional wastewater treatment processes designed to remove nutrients such as organic matter, nitrogen and phosphorus and they are discharged into aquatic environments at concentrations that will cause adverse effects (Erkus, 2012). This study aims to investigate paracetamol removal by operating the batch-activated sludge process under different operating conditions (SRT, HRT). Furthermore, the collected data were utilized to apply kinetic models in order to investigate the removal mechanism of paracetamol in the activated sludge process.

2. MATERIALS AND METHODS

The activated sludge utilized in the study was obtained from Van Gevaş Wastewater Treatment Plant's long-aeration biological activated sludge treatment facility. For the activated sludge to not lose its activity, it was continuously aerated with diffusers in the laboratory environment. To evaluate the removal efficiency of the activated sludge process under high dissolved oxygen conditions, the dissolved oxygen concentration in the aerobic reactor was kept within the range of 5.0 ± 0.75 mg/L. In the activated sludge process operation, 10, 20 and 30 day SRT was used and the sludge concentration was kept in the range of 2000-5000 mg/L. The synthetic domestic wastewater composition used in the study was prepared according to the ISO11733 standard. Synthetic domestic wastewater is prepared daily to preserve its composition and prevent changes. In the batch system activated sludge process, paracetamol concentration (Cas No: 103-90-2, Merck) was kept constant at 5 mg/L and the effect of different initial biomass concentrations (2500, 3500 and 4500 mg/L) was investigated. The batch-activated sludge device used in the study is shown in Figure 1.

Figure 1. Batch activated sludge system

The efficiency of the activated sludge reactor was checked by analyzing chemical oxygen demand (COD), suspended solids in the mixed liquid (MLSS), volatile suspended solids in the mixed liquid (MLVSS), pH and dissolved oxygen. All

experiments were carried out in accordance with Standard Methods (APHA, 2012). Quantification of paracetamol Yüzüncü Yıl University Center It was done on the HPLC device (Agilent1100) in his laboratory. The HPLC device used a 250x4.6 mm, 4µm particle size, kromasil C18 column. During the acclimation of activated sludge to paracetamol, system efficiency was calculated based on COD removal. Wastewater's COD was determined using the closed reflux colorimetric method with a spectrophotometer (WTW spectroflex 6100) (APHA, 2012).

2.1.Biological Degradation Studies

Paracetamol (0.5 mg/L) was added to synthetic wastewater containing 550 mg/L COD and fed to activated sludge for 12 days to help the biomass adapt to the environment. After a 12-day acclimation period, 5 mg/L paracetamol was fed to the system with wastewater at a constant concentration for 1 day, and the system was operated at room temperature for 24 hours. During biodegradation studies, the biomass concentration was kept constant at 2500 mg/L and a 2 L volume batch-activated sludge reactor was used. Air was supplied to the reactor to provide sufficient oxygen and 0.2 M HCl and NaOH was used to adjust the pH. Samples were collected at various time points, and the resulting supernatant was stored at 4°C following centrifugation.

2.2.Adsorption Studies

To determine the amount of biodegradation of paracetamol by the activated sludge process, the adsorption of paracetamol with activated sludge in the abiotic environment was examined. 200 mL of activated sludge was placed in Erlenmeyer flasks at three different biomass concentrations (2500, 3500 and 4500 mg/L), and 0.1% sodium azide was added to each bottle to kill the activated sludge bacteria and an orbital shaker was used at a mixing speed of 125 rpm. After the transformation of activated sludge into the abiotic environment, it was treated with

wastewater containing paracetamol at a fixed concentration of 5 mg/L. After centrifugation, the supernatant was filtered with Whatman GFC (1.2 µm) and adjusted to pH 2.0. Before HPLC analysis, samples were purified using an Oasis HLB cartridge to remove other compounds and ions that may obstruct the column. The methanol/pure water ratio used to condition the cartridges was 5/95 in a mixed solution of methanol and pure water with a pH of 2. After this stage, the cartridges were dried under vacuum. Then, 10 mL of sample was passed through the cartridge and conditioned. Conditioned 10 mL volume samples were washed with methanol. It was then transferred to vials to be analyzed by HPLC.

3. BULGULAR VE TARTIŞMA

3.1. Paracetamol adsorption and biodegradation kinetic models

In this study, where the effectiveness of the active ingredient paracetamol added to synthetic wastewater at a concentration of 5 mg/L was investigated, it was observed that 95-96% of paracetamol was removed in approximately 24 hours (Figure 2).

Figure 2 Change of paracetamol removal over time

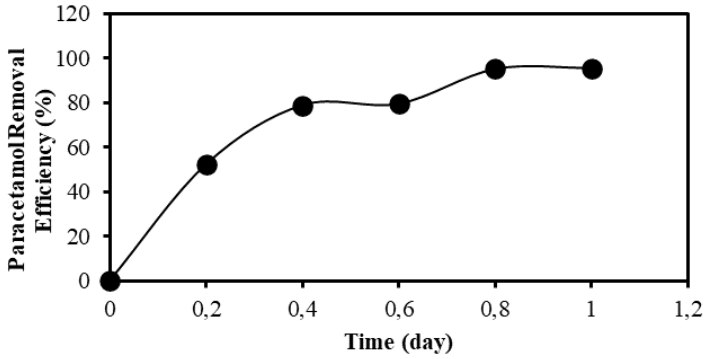

As seen in the experiments performed at a fixed biomass concentration of 2500 mg/L, the paracetamol removal efficiency is 80% in 14.4 hours (0.6 days), while it reaches up to 95% in 14-24 hours (0.6-1 day). In this case, the microorganisms in the wastewater tolerated the 5 mg/L paracetamol concentration even after being acclimated with 0.5 mg/L paracetamol for 12 days. It is important to evaluate kinetic data to better understand the removal mechanism. The results of the experiments with the batch-activated sludge process were applied to some well-known kinetic model equations (Table 1). The results are shown in Figure 3.

Table 1. Applied kinetic model equations

Kinetic Models	**Equation**	**Plot**		**Parameters**
Zero order	$C_t=C_e-k_0t$		C_t vs t	C_e= KN k_0= -E
Fist order	$C_t=C_e \exp(k_1t)$		Ln C_t vs t	C_e= KN k_1= -E
Second order	$\frac{C_t}{} = \frac{C_e}{(1+C_e\,k_2t}$		$1/C_t$ vs t	C_e= KN^{-1} k_2= -E
		Tip (I)	t/C_t vs t	C_e= E^1 k_2= E^2/KN
Pseudo Second order	$\frac{C_t}{} = \frac{k_{2p}C_e^2t}{(1+C_ek_{2p}t)}$	Tip (II)	$1/C_t$ vs 1/t	C_e= KN^{-1} k_{2p}= KN^2/E
		Tip (III)	C_t vs C_t/t	C_e= KN^{-1} k_{2p}= 1/E*KN
		Tip (IV)	Ct/t Vs C_t	C_e= -KN/E k_2= -E^2/KN

Figure 3 (a) Zero Order, (b) First Order, (c) Second Order, (d) Pseudo Second Order Type I, (e) Pseudo Second Order Type II, (f) Pseudo Second Order Type III, (g) Pseudo Second Order Type IV

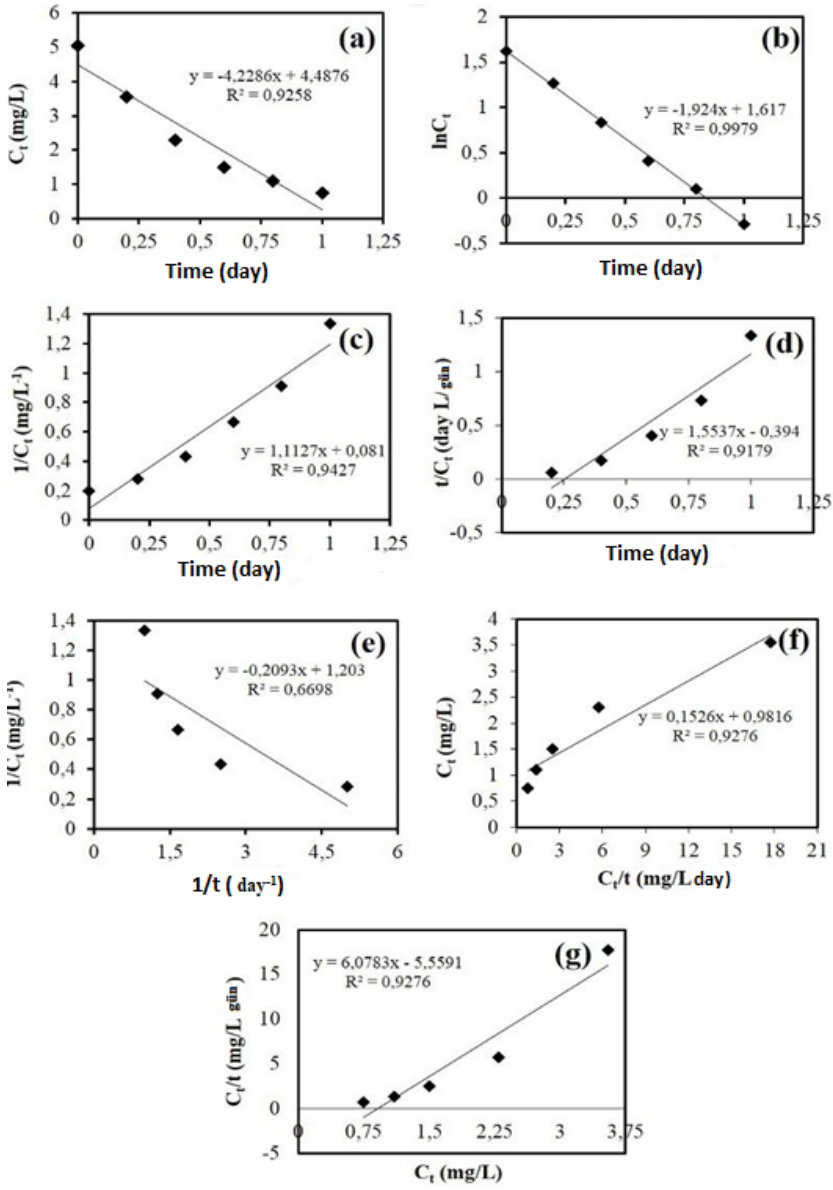

As shown in Figure 3, the biodegradation mechanism of paracetamol best fits the first-order kinetic model with a regression coefficient of 0.9979. In many studies in the literature, it has been reported that organic matter removal with activated sludge processes mostly meets first-order kinetics (Quintelas et al., 2020). Garcia-Rodrigues et al. (2015) stated that the excellent fit to the pseudo-first-order model was due to the impact of biodegradation processes, commonly described as first-order reactions.

3.2. Calculation of the biodegradation constant (k_{biol}) value

The pseudo-first-order kinetic model given below can be used to model the concentration of a pharmaceutical compound in wastewater (Dawas-Massalha et al. 2014).

$$\frac{C_i}{C_o} = e^{-k_{biyol}*SS*HRT} = e^{-k_{biol}*SP*SRT} \quad (1)$$

C_i: Input paracetamol concentration (µg/L)

C_o: Output paracetamol concentration (µg/L)

SP: Specific sludge production per unit volume of treated wastewater (gSS/m^3)

SS: Suspended solids concentration

k_{biol}: Pseudo-first-order biodegradation constant

If equation (1) is converted to its linear form, equation 2 is obtained:

$$ln\frac{C_i}{C_o} = -k_{biyol} * SS * HRT \quad (2)$$

The slope of the line acquired by plotting the $\ln(C_i/C_o)$ value against time will give the $-k_{biol} * SS.\ln(C_i/C_o)$ value. Studies have been conducted to establish a relationship between the biological kinetic degradation coefficient and removal capacity of

pharmaceutical compounds in aerobic batch experiments and the following results were obtained (Gome and Upadhyay, 2012).

• If k_{biol} <0.1 [L/gSS.day]: Less than 20% removal

• If 0.1 <k_{biol} <10: Partial removal ranging from 20-90%.

•k_{biol} >10: Biodegradation was responsible for over 95% of the removal, and the reactor configuration played a significant role in this process.

The biodegradation change of paracetamol obtained depending on time in batch experimental studies is shown in Figure 4.

Figure 4 Variation of biodegradation of paracetamol over time in batch experimental studies

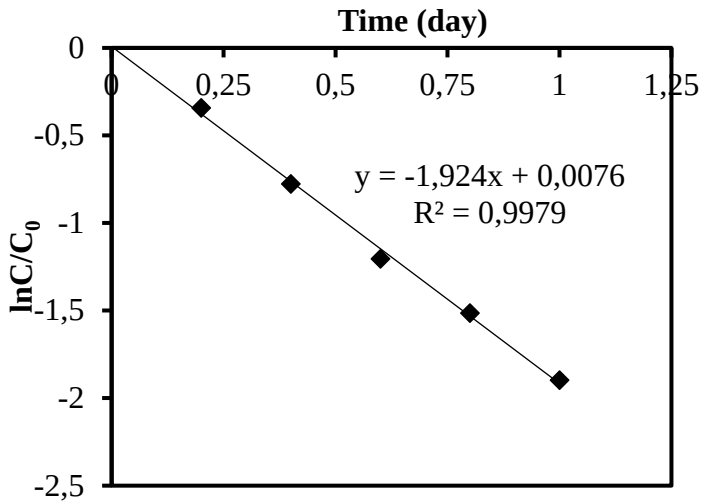

In this study, the k_{biol} value obtained for paracetamol was 18.47 L/gSS.day. The biological degradation mechanism is important in the removal of paracetamol, depending on the kbiol value. In other words, it can be said that over 95% of paracetamol removal is achieved through biodegradation. Jones et al. (2002) similar results were reported. Joss et al. (2006) also found the k_{biol}

value for paracetamol to be 10 L/gSS.day in their study. According to their findings, they reported that paracetamol is a chemical that is easily biodegradable. Paracetamol has a high biokinetic partition coefficient compared to other pharmaceutical compounds. It was observed that the removal rates increased as the SRT increased. Compounds such as ibuprofen and paracetamol with high kbiol values can be removed via biodegradation, regardless of SRT and HRT (Wang, 2009).

3.3.Adsorption Tests

In this study, adsorption tests were performed with activated sludge at concentrations of 2500, 3500, and 4500 mg/L, and adsorption contact times for paracetamol with initial concentrations of 5 mg/L were determined by activated sludge. The time to reach equilibrium for paracetamol was determined as 24 hours. Adsorption equilibrium graphs of paracetamol are given in Figure 5.

Figure 5 Paracetamol adsorption equilibrium graph

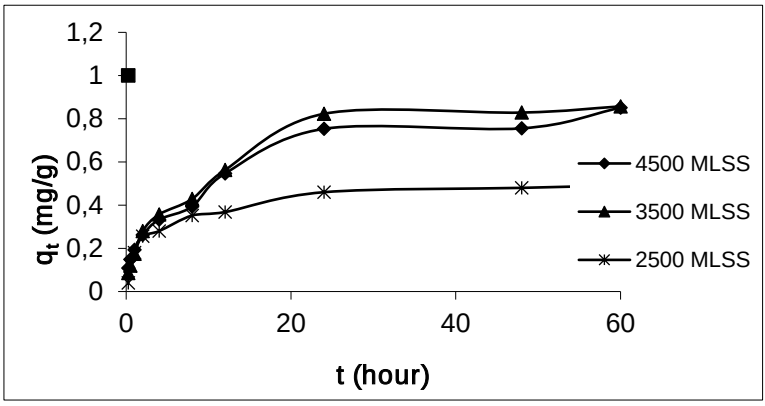

As expected, the adsorption capacity increases with the increase in biomass concentration. Padmesh et al. (2006) explained the reason for this behavior as surface saturation depends on the initial concentration of the pharmaceutical. For the same amount of usable space on biomass, the number of moles

of paracetamol increased depending on concentration (Quintelas et al., 2013). Increasing the amount of biomass leads to an increase in enzyme concentration, which in turn affects the reaction rate. When the amount of enzyme increases at a fixed substrate value, the substrate/enzyme ratio also decreases (Balcı et al. 2012). This study observed that activated sludge biomass successfully removed paracetamol in a batch system and the removal rate was over 90% at an applied concentration of 5 mg/L paracetamol. It was observed that the reaction orders of the removal kinetics at four different biomass concentrations and 5 mg//L paracetamol concentration followed the first order. According to the regression coefficient (R^2) values, values of 0.92 for the zeroth degree, 0.99 for the first degree and 0.94 for the second degree were obtained. Paracetamol removal percentage varies between 93 and 99. It was observed that the removal kinetics best fit the first-order reaction kinetics with a regression coefficient of 0.99.

4. CONCLUSION

Paracetamol removal method using activated sludge biomass was investigated in order to examine the effect of basic operating conditions on the fate of pharmaceutical compounds in activated sludge processes. Maximum removal efficiencies and biodegradation reaction kinetics were investigated for paracetamol in terms of chemical oxygen demand (COD) removal values. It was declared that the removal efficiency increased as biomass increased. Paracetamol removal ranged from 95% to 96%. It was observed that the reaction degrees of the removal kinetics at four different biomass concentrations and 5 mg//L paracetamol concentration matched the first order. It was seen that the removal kinetics best matched the first-order reaction kinetics (R^2= 0.99). The activated sludge system

proposed here is promising in removing pharmaceuticals from wastewater, and it has been found that activated sludge biomass is not adversely affected by high pharmaceutical concentrations.

Funding This study was supported by the Scientific Research Projects Coordination Unit, Van Yuzuncu Yil University, with the project code FYL-2019-8061.

REFERENCES

Alobaidi, R. A. K., Ulucan-Altuntas, K., Mhemid, R. K. S., Manav-Demir, N., & Cinar, O. (2021). Biodegradation of emerging pharmaceuticals from domestic wastewater by membrane bioreactor: the effect of solid retention time. *International Journal of Environmental Research and Public Health*, 18(7), 3395.

APHA (American Public Health Association) (2012). Standard methods for the examination of water and wastewater (22nd ed.) Washington D.C.

Balcı B., Keskinkan O., Erkuş A. (2012). Atıksulardan parasetamol gideriminde aktif çamur kullanılması. *Çukurova Üniversitesi Mühendislik Mimarlık Fakültesi Dergisi,* 27(2),1-12.

ISO 11733: Water quality-Determination of the elimination and biodegradability of organic compounds in an aqueous medium-Activated sludge simulation test, 2004.

Dawas-Massalha, A., Gur-Reznik, S., Lerman, S., Sabbah, I., Dosoretz, C. G. (2014). Co-metabolic oxidation of pharmaceutical compounds by a nitrifying bacterial enrichment. *Bioresource technology,* 167, 336-342.

Erkus (2012). Bazı Tıbbi Kimyasalların Aerobik Sistemlerde Farklı İşletimKoşullarında Gideriminin İncelenmesi,

(Doktora tezi). Çukurova Üniversitesi, Fen Bilimleri Enstitüsü, Adana.

Erkus, A., Basıbüyük, M., Erkus, F.S. (2015) The examination of paracetamol and diclofenac removal in activated sludge systems under different operating conditions, *International Journal of Ecosystems and Ecology Science*,5 (2015) 315–320.

Garcia-Rodriguez, A., Matamoros, V., Fontàs, C., Salvado, V. (2015). The influence of Lemna sp. and Spirogyra sp. on the removal of pharmaceuticals and endocrine disruptors in treated wastewaters. *International Journal of Environmental Science and Technology*, 12, 2327-2338.

Gome, A., Upadhyay, K. (2012). Chemical kinetics of ozonation and other processes used for the treatment of wastewater containing pharmaceuticals: a review. *International Journal of Current Research and Review*, 4(22), 157.

Jones, O. A. H., Voulvoulis, N., Lester, J. N. (2002). Aquatic environmental assessment of the top 25 English prescription pharmaceuticals. *Water Research,* 36(20), 5013-5022.

Joss, A., Zabczynski, S., Göbel, A., Hoffmann, B., Löffler, D., McArdell, C. S., Ternes, T.A., Thomsen, A., Siegrist, H. (2006). Biological degradation of pharmaceuticals in municipal wastewater treatment: proposing a classification scheme. *Water Research,* 40(8), 1686-1696.

Kasprzyk-Hordern B., Dinsdale R.M., Guwy A.J. (2009). The removal of pharmaceuticals, personal care products, endocrine disruptors and illicit drugs during wastewater treatment and its impact on the quality of receiving waters. *Water Research*, 43,363–380.

Li X., Zheng W., Kelly W.R. (2013). Occurrence and removal of pharmaceutical and hormone contaminants in rural wastewater treatment lagoons. *Science Total Environment*, 445–446:22–28.

Li, D., Yu, T., Zhang, Y., Yang, M., Li, Z., Liu, M.M. Qi, R. (2010). Antibiotic Resistance Characteristics of Environmental Bacteria from an Ox tetracycline Production Wastewater Treatment Plant and the Receiving River. *Applied and Environmental Microbiology*, 76, 3444-345.

Maculewicz, J., Kowalska, D., Świacka, K., Tański, M., Stepnowski, P., Białk-Bielińska, A., & Dołżonek, J. (2022). Transformation products of pharmaceuticals in the environment: Their fate,(eco) toxicity and bioaccumulation potential. *Science of the Total Environment*, 802, 149916.

Özgüven (2020). Veteriner İlaçlarının Çevrede Bulunuşu ve Etkileri, *Bitlis Eren Üniversitesi Fen Bilimleri Dergisi*, 9(1), 487–499.

Özgüven, A., Öztürk, D., & Bayram, T. (2021). An investigation based on removal of ibuprofen and its transformation products by a batch activated sludge process: A kinetic study. *Environmental Research and Technology*, 4(4), 329-341.

Özgüven, A., Yönten, V., & Kıvanç, M. R. (2022). The Utilization of a Statistical Program for Chemical Oxygen Demand Reduction and Diclofenac Sodium Removal from Aqueous Solutions via Agaricus campestris/Amberlite Styrene Divinylbenzene Biocomposite. *Arabian Journal for Science and Engineering*, 47(1), 441-454.

Padmesh, T.V.N., Vijayaraghavan, K., Sekaran, G., Velan, M. (2006). Biosorption of acid blue 15 using fresh water macroalga Azolla filiculoides: batch and column studies, *Dyes and Pigments*, 71, 77–82.

Quintelas, C., Costa, F., Tavares, T. (2013). Bioremoval of diethylketone by the synergistic combination of microorganisms and clays: uptake, removal and kinetic studies, *Environment Science Pollution Research*, 208, 1374–1383.

Quintelas, C., Mesquita, D. P., Torres, A. M., Costa, I., Ferreira, E. C. (2020). Degradation of widespread pharmaceuticals by activated sludge: Kinetic study, toxicity assessment, and comparison with adsorption processes. *Journal of Water Process Engineering*, 33, 101061.

Sahar E., Messalem R., Cikurel H., Aharoni A., Brenner A., Godehardt M., Jekel M., Ernst M. (2011). Fate of antibiotics in activated sludge followed by ultrafiltration (CAS-UF) and in a membrane bioreactor (MBR). *Water Research*, 45, 4827–4836.

Samal, K., Mahapatra, S., & Ali, M. H. (2022). Pharmaceutical wastewater as Emerging Contaminants (EC): Treatment technologies, impact on environment and human health. *Energy Nexus*, 6, 100076.

Schaider L.A., Rudel R.A., Ackerman J.M., Dunagan S.C., Brody J.G.(2014).Pharmaceuticals,perfluorosurfactants,andothe rorganicwastewater compounds in public drinking water wells in a shallow sand and gravel aquifer. *Science Total Environment*, 468–469,384–393.

Ternes, T., Joss, A., Kreuzinger, N., Miksch, K., Lema, J.M., Von Gunten, U., Mcardell, C. H. S., and Siegrist, H. (2005). Removal of pharmaceuticals and personal care products:

results of Poseidon project. Water Environment Federation, 227-243.

Wang, S. C. (2009). Removal of Emerging Contaminants in Biological Treatment (Doctoral dissertation, University of California, Los Angeles).

Whitacre, D. M., Monteiro, S. C., Boxall, A. B. (2010). Occurrence and fate of human pharmaceuticals in the environment. *Reviews of Environmental Contamination and Toxicology,* 202,53-154.

A COMPREHENSIVE ANALYSIS OF ASSOCIATION RULES IN ÇANKIRI KARATEKIN UNIVERSITY LIBRARY'S BOOK BORROWING RECORDS

Pelin AKIN[1]

Didem GULERYUZ[2]

1. INTRODUCTION

With computer systems in every field, access to information has increased rapidly (Akın & Koç, 2021). Using computers in libraries is also very common to obtain more accurate and quality information. With the more active use of computers and the internet in libraries, the desired information can be accessed quickly. These library systems, called library automation systems, provide documents and lend resources or information consultation services. Providing documents, cataloging, lending, supervision of periodicals, and consulting services in libraries based on information systems, using computers in library management, and benefiting from remote communication technology is possible with the library automation system. The automation system allows the most appropriate way to manage and share resources in the library. Library automation software is used in almost all libraries, especially university libraries. In this way, researchers can be

[1] Arş. Gör. Dr., Çankırı Karatekin University, Faculty of Science, Department of Statistics, pelinakin@karatekin.edu.tr, ORCID: 0000-0003-3798-4827.

[2] Assoc. Prof., Bayburt University, Faculty of Applied Sciences, Department of Management İnformation Systems, dguleryuz@bayburt.edu.tr, ORCID: 0000-0003-4198-9997.

provided with better quality and faster service. Library Automation Systems collects a large amount of data about the history of readers' visits to library resources. Much important information is hidden behind such data, and Data Mining is used to reveal this confidential information (Erdemalp, Gültekin, & Bayramoğlu, 2022). Data mining uses statistics and machine learning algorithms to transform raw data into information (Koc & Akın, 2022; Ozden & Guleryuz, 2022). Association Rules, one of the data mining techniques, is an important technology that contains the necessary information to extract the interrelationships between descriptive data items from large amounts of data (Alpaydın, 2011). The Association Rules method is used to detect frequently recurring items in a dataset and to detect connections and relationships (patterns) between items in a dataset. Association rules are a descriptive model that supports future studies by analyzing the behavior of data. Bussaban and Kularbphettong (2014) created a model for analyzing student behavior using library resources based on association rules in the data mining technique. They found the rules with the apriori algorithm. Ping (2015) used association rules analysis for library loans to analyze different types of reader library collections and automatically provide readers with other books related to that book. Sihachack and Yu (2016) described the analysis of user behavior regarding borrowed book registration at the National Central Library University of Laos using the association rule technique based on data mining technologies. Finally, they showed that eight user behavior rules could be used to manage the library resource. Muhajir, Kesumawati, and Mulyadi (2018) determined the most preferred library in public libraries in the United States with the association rules analysis. Yi, Chen, and Cong (2018) used the Artificial bee colony algorithm from the association rule to find the loan rules based on the loan records of the readers and suggest other book lists to them in a personalized way.

Irfiani (2020) determined the pattern of book loan evaluation by using the Apriori algorithm in the public library. Devega (2020) used the Eclat algorithm from the association rules for determining books that are often borrowed together. Shen, Wang, Yang, and Lv (2021) analyzed the library loan records using a hybrid-based Apriori Genetic algorithm. Wang, Xu, Feng, Peng, and Ma (2022) proposed a Markov logic network method to restructure association rule mining tasks and apply it to library personalized services. The Markov logic network approach outperforms traditional association rule algorithms in model performance measures. Ningsih, Sihombing, and Sitorus (2022) created a model by applying an Apriori algorithm from association rules to determine which books are frequently borrowed so that library officials know the information about frequently borrowed books. Özlük and Kayaalp (2022) applied Association Rules algorithms to the Düzce University Library Records dataset and revealed rules regarding co-borrowing patterns at the level of book categories. In addition, he compared the performance of the Rules of Association algorithms on Python, R, and SPMF platforms based on their running time and the amount of memory occupied during the experiments.

In this study, we applied the Association Rules algorithms from the Data Mining methods to the book borrowing data set obtained from the Çankırı Karatekin University Library. Association rules algorithms Apriori, Eclat, and LCM were examined using different support and confidence values. The association rules between different borrowed book categories are introduced. The remainder of the study is organized as follows. Section 2 introduces Apriori, Eclat, and LCM algorithms from association rules analysis. Section 3 explains the application of the association rules analysis with library borrowing data. Finally, a brief discussion is given in Section 4.

2. MATERIALS AND METHODS

Association rules analysis is unsupervised data mining that tries to find relationships between records in a data set. Association rule analysis can be viewed as a two-step process.

i. All standard item sets are found, and a predetermined minimum support value defines the frequency of these identified item sets.

ii. It creates strong association rules from common item sets. These rules are defined as rules that provide the minimum value of support and confidence (Han, Pei, & Kamber, 2011).

Another value calculation used in association rules analysis is the "lift" value. The lift value is calculated as follows:

$$\text{Lift}(X \Rightarrow Y) = \frac{\text{confidence}(X \Rightarrow Y)}{\text{support}(Y)} \quad (1)$$

If the leverage value exceeds one, it indicates a significant rule among the rules. If it is less than 1, it indicates a meaningless rule among the rules. In order to determine association rules, frequently repeated items must be found, and these found items must be repeated as much as the predetermined minimum support number. Strong association rules are then created from these repeated items. There are many algorithms in association rules analysis. We used Apriori, Eclat, and LCM algorithms in this study.

2.1. Apriori Algorithm

The Apriori algorithm is the most preferred in association rules. In the stages of the algorithm, firstly, threshold values are determined to compare the support values, and the results are expected to be equal to or greater than these threshold values. By scanning the database, the number of repetitions for each product

to be included in the analysis, the support is calculated with the following formula (Mittal, Pareek, & Agarwal, 2015):

$$\text{Support}(X \Rightarrow Y) = P(X \cup Y) \quad (2)$$

The formula shows the probability of the simultaneous existence of X and Y in the transaction. These support values are compared to the threshold support values. Rows with values less than the threshold support number are excluded from the analysis, and relevant observations are considered. The relationship between items is expressed in confidence and defined by the formula.

$$\text{Confidence}(X \Rightarrow Y) = (P(X \cup Y))/(P(X)\ ) \quad (3)$$

This situation is double, triple, quadruple, etc. groupings are repeated. After groups are determined, the association rules are derived by looking at the rule support criteria and calculating the trust criteria for each rule (Özkan, 2020).

2.2. Eclat Algorithm

Eclat is an algorithm for discovering frequently occurring sets of items in a transactional database proposed by Zaki (2000). The Eclat algorithm has a structure that operates on a vertical data format. Eclat uses a depth-first search to find frequently used items instead of a breadth-first search and sets intersections to extract relationship rules. The Eclat algorithm is a more efficient and scalable version of the Apriori algorithm.

2.3. Linear-Time Closed Itemset Mine (LCM) Algorithm

The linear-time Closed itemset Mine (LCM) algorithm is supposed to be one of the fastest closed item set mining algorithms. LCM is an abbreviation of linear time closed item set mine (Uno, Asai, Uchida, & Arimura, 2003). Enumerates (output or count) all frequent item sets, all maximum frequent item sets, or all frequently closed item sets in a given transaction database

for a given support (Naresh & Suguna, 2019). LCM has a very stable performance for both computation time and memory usage. The basic idea of this algorithm is depth priority search. In its first step, the LCM calculates the frequency of each item set consisting of one item. An item is added if that item set is frequent, resulting in numbered frequent item sets. In this way, iteratively, LCM enumerates all frequent item sets (Nigam, Nigam, & Dalal, 2017).

3. APPLICATION

This study used the data of the book records borrowed from the Çankırı Karatekin University library between 2017 and 2023 (January). Total book enrollment is 26263 taken from the library by the student, master student, Ph.D. student, academic staff, administrative staff, and permanent worker at Çankırı Karatekin University. Twenty-nine book categories were obtained in the whole data set. The most preferred book category is Turkish Language and Literature, with 18.2%. The least preferred book category is Agriculture, with 0.2%. In addition, 12.1% of men borrow books in the Turkish Language and Literature category, while 23% of women borrow books in the Turkish Language and Literature category. The whole item frequency plot of preference for 29 book categories is given in Figure 1.

Figure 1. The Absolute Item Frequency Plot for 29 Book Categories

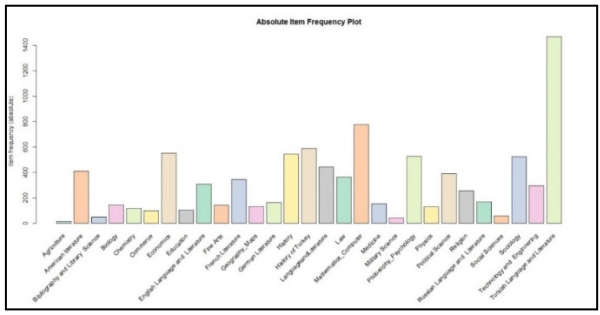

In order to determine the book categories that are preferred to be loaned together during the preparation of the data, single-book borrowing records were not taken into account. However, 6131 records were considered in which two or more books were borrowed together. After the data preprocessing and transformation processes, analyses were made using R software version 4.2.2 and SPMF version 2.57. Figure 2 gives runtime graphs of Apriori, Eclat, and LCM algorithms for different support values.

Figure 2. Comparison of Apriori, LCM, and Eclat Algorithm

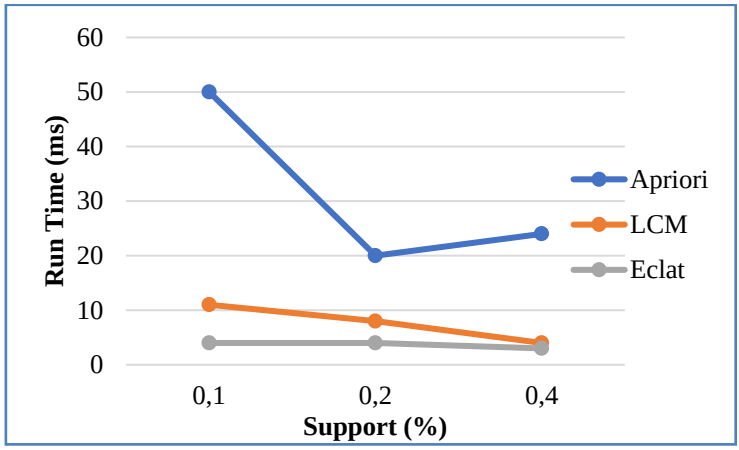

Figure 2 shows the average running times (ms) of Apriori, Eclat, and LCM algorithms for 0.1%, 0.2%, and 0.4% support values. The Eclat algorithm is the fastest in terms of run times for all support values. The first step to creating a set of Eclat algorithms is determining the optimal thresholds for support and confidence. Figure 3 shows the different support and confidence values and how many rules were generated for each combination.

Figure 3. Comparison of the Eclat Algorithm for Different Support and Confidence Values

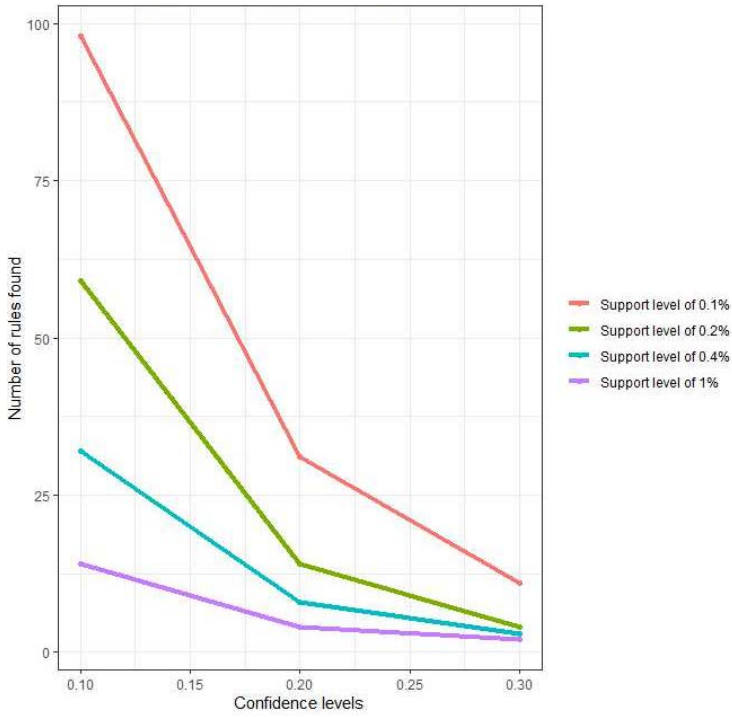

When the support level was 0.1%, too many rules were found, which caused extreme learning. Only a few rules were set with deficient confidence when the support level was 1%. This situation means that there were relatively frequent associations in our dataset. Since the resulting rules were not representative and few, this rule was not chosen either. While the support level is 0.4%, the minimum confidence level should be 0.2; otherwise, the rule level will not be sufficient. However, when it is 0.2%, this situation disappears.

To summarize, it was selected as a support level of 0.2% and a confidence level of 0.2. A total of 14 rules were created when the Eclat algorithm was applied to the data by taking the min support value of 0.2% and the min confidence value of 0.2.

The ten rules with the highest confidence level are in Table 1 below.

Table 1. Association Rule for Eclat Algorithm with The Min Support Value Of 0.2% and Confidence Value of 0.2.

No	Association Rule	Support	Confidence	Lift	Count
1	{History, Political Science}c=>{History of Turkey}	0.0035	0.4230	4.4113	22
2	{Commerce}=>{Economics}	0.0061	0.3800	4.2282	38
3	{LanguageandLiterature}=> Turkish Language and Litarature}	0.0262	0.3634	1.5199	161
4	{French Literature}=>{Turkish Language and Litarature}	0.0169	0.3005	1.2570	104
5	{Physics}=>{Mathematics_Computer}	0.0063	0.2977	2.3521	39
6	{History of Turkey, Political Science}=>{history}	0.0035	0.2972	3.3322	22
7	{German Literature}=>{Turkish Language and Litarature}	0.0073	0.2743	1.1475	45
8	{Social Sciences}=>{Economics}	0.0026	0.2711	3.0175	16
9	{English Language and Literature=>{Turkish Language and Litarature}	0.0133	0.2662	1.1134	82
10	{Russian Language and Literature}=>{Turkish Language and Litarature}	0.0066	0.2411	1.0086	41

Table 1 shows the ten rules with the highest confidence value created with the Eclat algorithm. According to the association analysis rule results, in the first rule, 42% of the library users who took history and political science books also took a history of Turkey book. The total number of book categories taken together is twenty-two. In the second rule, library users who borrowed commerce books also borrowed the economic book 38%. The total number of book categories taken together is thirty-eight. In the third rule, 30% of library users who borrowed language and literature books also borrowed Turkish language and literature books. The total number of book categories taken together is one hundred and sixty-one. In the fourth rule, users of the library who borrowed French literature books also borrowed Turkish language and literature books 30% of the time. The total number of book categories taken together is one hundred and forty-four. In the fifth rule, 30% of the users of the library who took on loan Physics books also took on loan Mathematics-Computer books. The total number of book categories taken together is thirty-nine. In the sixth rule, 30% of the library users who borrowed the history of Turkey and political science books also took history books. The total number of book categories taken together is twenty-two. In the seventh rule, 27% of library users who borrowed German literature books also

borrowed Turkish language and literature books. The total number of book categories taken together is forty-five. In the eighth rule, library users who borrowed Social Sciences books also borrowed the economic book 27%. The total number of book categories taken together is sixteen. In the ninth rule, 26% of those who borrowed the English Language and Literature book also borrowed the Turkish language and literature book. Finally, it was seen that 24% of those who borrowed the Russian Language and Literature book borrowed the Turkish language and literature book.

4. CONCLUSIONS

Today, library automation software is used in all libraries. Library automation systems allow the management and optimum sharing of resources in the library. The slowness and errors caused by the human factor in the transactions made on the broadcasts (borrowing/taking, an extension of time, etc.) are eliminated with the system. In this study, we applied the association rules Apriori, Eclat, and LCM algorithms to the book borrowing data set obtained from the Çankırı Karatekin University Library. When these algorithms are compared according to different support values with running time. The Eclat algorithm is faster than other algorithms. This result is compatible with the literature (Nigam et al., 2017). Finding the optimal support and confidence values in the Eclat algorithm is significant. In this study, four different support and five different confidence values were used, and a comparison was made according to the number of rules that emerged. Appropriate rules for the values have been obtained with a support level of 0.2% and a confidence level of 0.2. In total, 14 rules were obtained. When we examine the ten rules with the ten highest levels of confidence, it was seen that those who took a book in the

Language and Literature, French Literature, German Literature, English Language and Literature, Russian Language and Literature category also borrowed the Turkish Language and Literature book. It was observed that those who borrowed history and Political Science books borrowed the History of Turkey book. It was found that library users who took Economics books also borrowed Commerce and Social Sciences categories in the book areas. Finally, users who borrowed Physics books were also interested in Mathematics-Computer books. These results can be considered a suggestion for arranging the books in the library.

Acknowledgment

The authors gratefully acknowledge Çankırı Karatekin University Library for data set support.

REFERENCES

Akın, P., & Koç, T. (2021). Ağaç tabanlı regresyon modelleri kullanılarak sağlık göstergeleri ile insani gelişme endeksinin tahmini.

Alpaydın, E. (2011). *Yapay öğrenme*: Boğaziçi Üniversitesi Yayınevi.

Bussaban, K., & Kularbphettong, K. (2014). Analysis of users' behavior on book loan log based on association rule mining. *International Journal of Industrial and Manufacturing Engineering, 8*(1), 18-20.

Devega, M. (2020). *Implementation of ECLAT Algorithm Technology: Determining Books Borrowing Pattern in University library.* Paper presented at the IOP Conference Series: Earth and Environmental Science.

Erdemalp, Ö., Gültekin, Ö. F., & Bayramoğlu, T. (2022). Paneel veri ve makine öğrenmesi yöntemiyle gelir dağılımı ve insani gelişmişlik arasındaki ilişki üzerine bir analiz.

Gaziantep University Journal of Social Sciences, 21(2), 564-582.

Han, J., Pei, J., & Kamber, M. (2011). *Data mining: concepts and techniques*: Elsevier.

Irfiani, E. (2020). Determination of Book Loan Association Pattern Using Apriori Algorithm in Public Libraries. *Techno Nusa Mandiri, 17*(2), 137-142.

Koc, T., & Akın, P. (2022). Estimation of High School Entrance Examination Success Rates Using Machine Learning and Beta Regression Models. *Journal of Intelligent Systems: Theory and Applications, 5*(1), 9-15.

Mittal, M., Pareek, S., & Agarwal, R. (2015). Efficient ordering policy for imperfect quality items using association rule mining. In *Encyclopedia of Information Science and Technology, Third Edition* (pp. 773-786): IGI Global.

Muhajir, M., Kesumawati, A., & Mulyadi, S. (2018). *Apriori Algorithm for Frequent Pattern Mining for Public Librariesin United States.* Paper presented at the Proceedings of the International Conference on Mathematics and Islam.

Naresh, P., & Suguna, R. (2019). *Association rule mining algorithms on large and small datasets: A comparative study.* Paper presented at the 2019 International Conference on Intelligent Computing and Control Systems (ICCS).

Nigam, B., Nigam, A., & Dalal, P. (2017). Comparative study of top 10 algorithms for association rule mining. *International Journal of Computer Sciences and Engineering, 5*(8).

Ningsih, A. Y., Sihombing, V., & Sitorus, S. P. (2022). Implementation of a priori algorithm for book lending at state high school library I Silima Pungaga-Punga Parongil. *Sinkron: jurnal dan penelitian teknik informatika, 7*(1), 196-203.

Ozden, E., & Guleryuz, D. (2022). Optimized machine learning algorithms for investigating the relationship between economic development and human capital. *Computational Economics, 60*(1), 347-373.

Özkan, Y. (2020). *Veri madenciliği yöntemleri*: Papatya Yayıncılık Eğitim.

Özlük, S., & Kayaalp, F. (2022). Birliktelik Kurallariyla Kütüphane Ödünç Alma Kayitlarinin Analizi: Düzce Üniversitesi Örnek Uygulamasi.

Ping, H. (2015). The research on personalized recommendation algorithm of library based on big data and association rules. *The Open Cybernetics & Systemics Journal, 9*(1).

Shen, Y., Wang, J., Yang, X., & Lv, Y. (2021). *Analysis of Library loan records based on hybrid Apriori-Genetic algorithm.* Paper presented at the 2021 2nd International Conference on Artificial Intelligence and Computer Engineering (ICAICE).

Sihachack, T., & Yu, L. (2016). Analysis of User's Behavior on Borrowed Book Record in National Central Library University of Laos. *Transactions on Machine Learning and Artificial Intelligence*, 28-35.

Uno, T., Asai, T., Uchida, Y., & Arimura, H. (2003). *LCM: An Efficient Algorithm for Enumerating Frequent Closed Item Sets.* Paper presented at the Fimi.

Wang, S., Xu, J., Feng, Y., Peng, M., & Ma, K. (2022). A Markov logic network method for reconstructing association rule-mining tasks in library book recommendation. *Information Discovery and Delivery, 50*(1), 34-44.

Yi, K., Chen, T., & Cong, G. (2018). Library personalized recommendation service method based on improved association rules. *Library Hi Tech, 36*(3), 443-457.

Zaki, M. J. (2000). Scalable algorithms for association mining. *IEEE transactions on knowledge and data engineering, 12*(3), 372-390.

Developments in the Field of Engineering

YAZ Yayınları
M.İhtisas OSB Mah. 4A Cad. No:3/3
İscehisar / AFYONKARAHİSAR
Tel : (0 531) 880 92 99
yazyayinlari@gmail.com • www.yazyayinlari.com

ISBN: 978-625-6524-95-8